NASA Technical Memorandum 1999–206892, Volume 7

SeaWiFS Postlaunch Technical Report Series

Stanford B. Hooker, Editor
NASA Goddard Space Flight Center
Greenbelt, Maryland

Elaine R. Firestone, Senior Technical Editor
SAIC General Sciences Corporation
Beltsville, Maryland

Volume 7, The Fifth SeaWiFS Intercalibration Round-Robin Experiment (SIRREX-5), July 1996

B. Carol Johnson, Howard W. Yoon, Sally S. Bruce, Ping-Shine Shaw, and Ambler Thompson
National Institute of Standards and Technology
Gaithersburg, Maryland

Stanford B. Hooker
NASA Goddard Space Flight Center
Greenbelt, Maryland

Robert A. Barnes and Robert E. Eplee, Jr.
SAIC General Sciences Corporation
Beltsville, Maryland

Stephane Maritorena
Universities Space Research Association
Greenbelt, Maryland

James L. Mueller
CHORS/San Diego State University
San Diego, California

Abstract

This report documents the fifth Sea-viewing Wide Field-of-view Sensor (SeaWiFS) Intercalibration Round-Robin Experiment (SIRREX-5), which was held at the National Institute of Standards and Technology (NIST) on 23–30 July 1996. The agenda for SIRREX-5 was established based on recommendations made during SIRREX-4. For the first time in a SIRREX activity, instrument intercomparisons were performed at field sites, which were near NIST. The goals of SIRREX-5 were to continue the emphasis on training and the implementation of standard measurement practices, investigate the calibration methods and measurement chains in use by the oceanographic community, provide opportunities for discussion, and intercompare selected instruments. As at SIRREX-4, the day was divided between morning lectures and afternoon laboratory exercises. A set of core laboratory sessions were performed: 1) in-water radiant flux measurements; 2) in-air radiant flux measurements; 3) spectral radiance responsivity measurements using the plaque method; 4) device calibration or stability monitoring with portable field sources; and 5) various ancillary exercises designed to illustrate radiometric concepts. Before, during, and after SIRREX-5, NIST calibrated the SIRREX-5 participating radiometers for radiance and irradiance responsivity. The Facility for Automated Spectroradiometric Calibrations (FASCAL) was scheduled for spectral irradiance calibrations for standard lamps during SIRREX-5. Three lamps from the SeaWiFS community were submitted and two were calibrated.

1. INTRODUCTION

Experience with the proof-of-concept Coastal Zone Color Scanner (CZCS) underscored the importance of sustained and coordinated programs to verify the optical sensor calibration and the accuracy of the derived products. Compared to CZCS, more rigorous specifications on measurement uncertainties are required to address new or updated geophysical and biological problems identified by the science community. As a second-generation ocean color radiometer, the Sea-viewing Wide Field-of-view Sensor (SeaWiFS) instrument offers a variety of design improvements over the CZCS (Hooker et al. 1993). Since flight operations began on 18 September 1997, SeaWiFS has provided global estimates of oceanic chlorophyll and other bio-optical quantities (McClain et al. 1998).

Two important goals of the SeaWiFS Project are to determine, from the SeaWiFS radiance measurements, 1) normalized water-leaving radiance with an uncertainty of 5%, and 2) chlorophyll *a* concentration with an uncertainty of 35%. (All uncertainties are expressed as relative standard uncertainties unless otherwise noted.†) These goals are ambitious. They can only be achieved by augmenting the SeaWiFS measurements with a program of ongoing validation measurements to verify the radiometric uncertainty and long-term stability of the SeaWiFS instrument's radiance responsivities, and to validate the atmospheric correction models and algorithms used to convert SeaWiFS radiances to normalized water-leaving radiances. One of the principal approaches to this critical aspect of validation is frequent direct comparison between SeaWiFS estimates and *in situ* measurements of water-leaving radiance. Because the primary goal is to demonstrate that normalized water-leaving radiances derived from SeaWiFS data have uncertainties of less than 5%, the comparative *in situ* radiometric measurements must be calibrated to an uncertainty of less than 5%.

The only economically feasible approach to acquiring a large and globally distributed database of *in situ* radiometric measurements for SeaWiFS validation, is to solicit contributions of data from the oceanographic community at large. In addition, the aggregate data set must be assured to have uniform quality and an uncertainty of less than 5%. The SeaWiFS Project at the National Aeronautics and Space Administration (NASA) Goddard Space Flight Center (GSFC) is responsible for the calibration and validation of the data (McClain et al. 1992, and Hooker and McClain 1999). The program includes measurement and instrument protocols (Mueller and Austin 1992 and 1995), data archives (Hooker et al. 1994a and 1994b), and ongoing measurement intercomparisons. The fifth one in the series of these SeaWiFS Intercalibration Round-Robin Experiments (SIRREX-5) is described in this document. Finally, in an effort to coordinate and critically assess data from multiple global ocean color missions, the Sensor Intercomparison and Merger for Biological and Interdisciplinary Oceanic Studies (SIMBIOS) program was developed.

1.1 SIRREX-1 to SIRREX-4

The SeaWiFS instrument was characterized and calibrated by its manufacturer, Raytheon Santa Barbara Research Center (SBRC).† Prior to launch, SeaWiFS was re-

† The guidelines for evaluating and expressing the uncertainty of measurement results, as followed in this document, are given in Taylor and Kuyatt (1994).

† Formerly, Hughes Santa Barbara Remote Sensing (SBRS).

calibrated at the spacecraft integrator, Orbital Sciences Corporation (OSC), with the support of the National Institute of Standards and Technology (NIST) and GSFC (Johnson et al. 1999). Since flight operations began, the radiometric calibration of SeaWiFS was assessed using the sun and the moon, as well as comparisons to *in situ* data (McClain et al. 1998).

The SIRREX activities, which began in 1992, arose from the recognition of the need to maintain internal consistency between calibrations of *in situ* instruments and of the SeaWiFS instrument. The SIRREX Program includes domestic laboratories, manufacturers of instruments, and international collaborators. The domestic laboratories include:

1) GSFC;
2) Center for Hydro-Optics and Remote Sensing (CHORS) at San Diego State University (SDSU);
3) University of Miami (UM);
4) University of California at Santa Barbara (UCSB);
5) University of Arizona (UA); and
6) Moss Landing Marine Laboratory (MLML), in collaboration with Dennis Clark of the National Oceanic and Atmospheric Administration (NOAA).

The manufacturers include†:

a) Biospherical Instruments, Inc. (BSI) in San Diego, California;
b) Satlantic, Inc., in Halifax, Nova Scotia; and
c) Analytical Spectral Devices (ASD) in Boulder, Colorado.

The international partners with the SeaWiFS Project are the Plymouth Marine Laboratory (PML) in Plymouth, United Kingdom, and the Joint Research Centre (JRC) in Ispra, Italy.

The strategy adopted for SeaWiFS validation is to calibrate all involved instruments within a network consisting of these, and possibly a few additional, laboratories. The general purposes of the SIRREX activities are to transfer NIST spectral irradiance measurements through GSFC to all participating laboratories in the SeaWiFS ocean community, and to the calibration standards used to calibrate the SeaWiFS instrument for radiance responsivity.

The core objectives of SIRREX include the following:

1. Intercalibrate FEL-type lamp working standards of spectral irradiance used at the participating laboratories, and to reference each lamp to NIST by way of secondary standards;
2. Intercalibrate integrating sphere sources of spectral radiance used at the various laboratories;
3. Intercompare plaques used as standards of spectral radiance when illuminated by an FEL lamp;
4. Intercompare transfer radiometers and other support electronics, most critically, shunt resistors and voltmeters, used to support radiometric calibrations at each laboratory.
5. Emphasize training and work to foster and encourage the uniform use of accepted protocols for laboratory calibration of radiometric instruments.

The first SIRREX (SIRREX-1) was held at CHORS on 27–31 July 1992 (Mueller 1993). SIRREX-1 demonstrated that the NIST spectral irradiance scale was not transferred from the GSFC secondary standard (FEL lamp F269) to the 17 other lamps with an expected uncertainty of approximately 1%.

The second SIRREX (SIRREX-2) was held at CHORS on 14–25 June 1993 (Mueller et al. 1994). SIRREX-2 showed that spectral irradiance lamps measured using the GSFC standard irradiance lamp (F269) were consistent with the program goals, because the uncertainty of these measurements was assessed to be about 1%. This was not true, however, for the spectral radiance measurements.

The third SIRREX (SIRREX-3) was held at CHORS on 19–30 September 1994 (Mueller et al. 1996). The spectral irradiance of the FEL lamps were intercompared, which showed a Type A uncertainty† of approximately 1%; this was the same as obtained during SIRREX-2. The data for FEL lamps common to both SIRREX-2 and -3, however, differed on the average by 1.5%. The 1.1–1.5% uncertainties associated with sphere radiance in SIRREX-3 were a significant improvement over the 5–7% results obtained during both SIRREX-1 and SIRREX-2.

The fourth SIRREX (SIRREX-4) was held at NIST during 3–10 May 1995 (Johnson et al. 1996). The agenda for SIRREX-4 was established by a consensus reached at the conclusion of SIRREX-3: there should be an emphasis on training to foster and encourage the uniform use of accepted protocols for calibrating radiometric instruments in the laboratory. To address this goal, there were five laboratory sessions, covering topics such as characterizing radiometers and establishing a scale of spectral radiance using a standard irradiance lamp and a diffusely reflecting plaque.

In the progress from the first to the fourth SIRREX, uncertainties in the intercomparisons between the spectral irradiance lamps improved from 8% to 1%. Intercomparisons of sphere radiance showed little improvement between SIRREX-1 and -2, with uncertainties as large as 7% in both experiments. In SIRREX-3, however, more rigorous characterization of both spheres and transfer radiometers reduced the uncertainties to approximately 1.5% in absolute spectral radiance and 0.3% in radiance stability for most spheres. Inadequate lamp current regulation

† Identification of commercial equipment to adequately specify the experimental problem does not imply recommendation or endorsement by the National Institute of Standards and Technology, nor does it imply that the equipment identified is necessarily the best available for the purpose.

† Type A uncertainties are those that are determined using statistical methods.

was clearly identified as the source of the larger (2%) uncertainty in the stability of the radiance of the CHORS sphere.

Plaque reflectance measurements in SIRREX-3 represent a qualitative improvement over results obtained during the earlier SIRREXs, primarily because of the improved performance of the SeaWiFS Transfer Radiometer (SXR) (Johnson et al. 1998a). Areas of improvement were identified, including the development of proper methods for stray light baffling, goniometric corrections for FEL lamp off-axis irradiances, and quantitative characterization of the bidirectional reflectance distribution function (BRDF) of diffuse Spectralon† plaques.

Intercomparisons between shunt resistors and voltmeters were done at the first three SIRREXs and, in general, the equipment used by all participants met the specified levels of uncertainty for radiometric calibration measurements. In the first and second SIRREXs, minor problems were identified with particular voltmeters which were either corrected or the instruments were taken out of service for this particular application.

In addition to the concerns about plaques, SIRREX-3 clearly demonstrated the need for rigorous laboratory practices. The shift in the spectral irradiance of GSFC lamp F269 emphasized the need to closely adhere to several extremely important protocols for usage and record keeping associated with FEL lamps in general, and with NIST secondary standards in particular (Mueller et al. 1996). Lamp operating hours should always be recorded. The voltage across the lamp terminals, as well as the lamp operating current, should be measured and recorded during each use of a lamp. As a matter of routine practice, the irradiance of a NIST secondary standard of spectral irradiance should be transferred locally to several additional working standard FEL lamps, and the transfer periodically verified for each of the local working standards at intervals of 20–30 h of lamp operation.

The local working standards should be used as the reference in most laboratory experiments, including lamp transfer intercomparisons. The NIST secondary standard usage is limited to occasional verification of the working standard reference lamp. This procedure will minimize the operating time accumulated on the NIST secondary standard, which should be returned to NIST for recalibration at intervals of 20–30 h of lamp operation. Lamp hours were not regularly logged for lamp F269, and lamp operating voltages were not recorded. Had the lamp's voltage history been maintained, the time at which the values changed during SIRREX-3 would have been more easily detected.

SIRREX-4 addressed the repeated failures in laboratory techniques during the first three SIRREXs by the emphasis on training, discussion, and demonstration of the accepted protocols for laboratory calibrations of radiometric instruments. The five laboratory sessions, which were led by NIST metrologists, offered a range of opportunities for interaction. The participants were divided into five groups of between 4–6 people and the groups participated in all five laboratory sessions during the five afternoons scheduled for SIRREX-4. Data from these and other SIRREX studies contributed to a summary of instrument performance.

1.2 SIRREX-5

SIRREX-4 provided the opportunity to use actual oceanographic radiometers in a laboratory calibration setting with the objective of demonstrating proper measurement practice and protocol implementation. It was concluded that future SIRREXs should expand this objective and perform intercomparisons of radiometers in field measurements designed to simulate the ocean environment. The participation by NIST personnel was viewed as essential, thus restricting the site to a location convenient to NIST. The in-water site selected was Little Seneca Lake near Germantown, Maryland, and the in-air site selected was adjacent to a pond on the NIST campus. Although these sites were not ideal in terms of the optical quality of the water, they were viewed as adequate for the first SIRREX *in situ* instrument intercomparison.

The essential questions addressed at SIRREX-5 were:

1. Do simultaneous *in situ* measurements with radiometers in the same class give the same answers?
2. Is the radiometric calibration correct?
3. Is the instrument stable from the calibration laboratory to the field site?
4. What measurement issues are being overlooked?

The SIRREX-5 format was based on that of the successful SIRREX-4, with morning lectures and discussions, midday and early afternoon measurement sessions, and a late afternoon daily presentation of results. Each day began at the conference hotel with the lectures, and then the participants went to various locations for the measurement sessions. In mid-afternoon, the workshop reconvened in the Facility for Advanced Radiometric Calibrations (FARCAL), located in Building 245 on the NIST campus.

The ambitious objectives of SIRREX-5 required additional planning and logistical support when compared to SIRREX-4. The instruments identified as suitable for the demonstrations and intercomparisons arrived at NIST before the workshop began and were calibrated by NIST personnel using standard lamps or the plaque method. The requirement to provide the community with assurance on their standards of spectral irradiance was accomplished by scheduling the Facility for Automated Spectroradiometric Calibrations (FASCAL) for irradiance calibrations during SIRREX-5. This special scheduling of a routine NIST calibration service allowed for timely measurements of these community standards with little or no effect on the individual field programs. A few special measurement sessions

† Spectralon is a registered trademark of Labsphere, Inc., North Sutton, New Hampshire.

and discussions, designed to demonstrate calibration methods or serve as a mini-workshop on some area of the SeaWiFS Ocean Optics Protocols (SOOP, Mueller and Austin 1995), were also implemented during SIRREX-5.

1.2.1 SIRREX-5 Agenda

Tuesday 23 July

0800	*Registration*	
0900	Introduction	S. Hooker
0910	Welcome to NIST	R. Hebner
0930	SIRREX-5 Overview	C. Johnson
0945	In-Water Activity Overview	J. Mueller
1000	In-Air Activity Overview	A. Thompson
1015	Plaque Laboratory Overview	S. Bruce
1030	*Break*	
1100	Laboratory Exercises	
1230	Box Lunches Delivered	
1530	*Break*	
1600	Data Analysis	
1730	Rapid Results Meeting	C. Johnson
1830	*Adjourn*	

Wednesday 24 July

0800	*Registration*	
0900	Introduction	J. Mueller
0910	Reflectance: Three Methods of Derivation	J. Mueller
0940	Portable Field Sources	P-S. Shaw
1010	BRDF and Care of Diffusers	Y. Barnes
1030	*Break*	
1100	Laboratory Exercises	
1230	*Box Lunches Delivered* 1530 *Break*	
1600	Data Analysis	
1730	Rapid Results Meeting	C. Johnson
1830	*Adjourn*	

Thursday 25 July

0800	*Registration*	
0900	Introduction	C. McClain
0910	JRC Calibration and Validation Activities: N. Atlantic	G. Zibordi
0930	Global Ocean System Eco-Dynamics (GLOBEC) Buoy Developments	J. Irish
0950	Above-Water Reflectance: Hyperspectral Imaging	C. Davis
1010	SeaWiFS Ocean Optics Protocols	C. McClain
1030	*Break*	
1100	Laboratory Exercises	
1230	*Box Lunches Delivered*	
1530	*Break*	
1600	Data Analysis	
1730	Rapid Results Meeting	C. Johnson
1830	*Adjourn*	

Friday 26 July

0800	*Registration*	
0900	Introduction	C. Johnson
0910	Preliminary Results: Modular Optoelectronic Scanner (MOS)	K-H. Suemnich
0930	NOAA/CSC Bio-Optics Field Programs	A. Subramaniam
0950	Calibration of Data Loggers for SIRREX-5	T. Larason
1010	Calibrations at BSI	J. Morrow
1040	UCSB	D. Menzies
1100	Laboratory Exercises	
1230	*Box Lunches Delivered*	
1530	*Break*	
1600	Data Analysis	
1730	Rapid Results Meeting	C. Johnson
1830	*Adjourn*	

Saturday 27 July

0900	Selected Laboratory Exercises	S. Hooker
1630	*Adjourn*	

Monday 29 July

0900	Introduction	J. Butler
0910	Ocean Optics with OCR-200s	S. McLean
0930	Atlantic Meridional Transect	G. Moore
0950	FEL Lamp Calibrations for SIRREX-5	C. Gibson
1010	Optical Measurements with ASD Instruments	B. Curtiss
1030	*Break*	
1100	Field Site Restoration	
1230	*Box Lunches Delivered*	
1930	*Banquet Dinner*	
2130	*Adjourn*	

Tuesday 30 July

0900	Introduction	S. Hooker
0910	In-Water Results	J. Mueller
0940	In-Air Results	A. Thompson
1010	Plaque Laboratory Results	C. Johnson
1030	*Break*	
1100	Revisions to the Protocols	C. McClain
1130	SIRREX-6	S. Hooker
1300	*Adjourn*	

Unlike SIRREX-4, where the laboratory space was not sufficient to allow everyone to participate in the laboratory exercises, the number of groups and activities were increased at SIRREX-5 so everyone would have a chance to participate. The individuals involved with SIRREX-5, and their levels of participation, are listed in Appendix A. The group designations and the laboratory exercises involved in SIRREX-5 are shown in Table 1. The laboratories corresponded to:

Table 1. Laboratory schedule for participant groups A–H during SIRREX-5. See Appendix A for the group compositions.

Lab	Tuesday July 23	Wednesday July 24	Thursday July 25	Friday July 26	Saturday July 27
I	A	D	E	C	B
II	D	F	G	E	H
III	B	H	C	A	
IV	E	G	D	H	
V	G	C	F	B	A
VI	H	B	A	F	
VII	F	E	H	G	D
VIII	C	A	B	D	

1) Lab I, In-Water Data Collection;
2) Lab II, In-Water Data Processing;
3) Lab III, In-Air Data Collection;
4) Lab IV, In-Air Data Processing;
5) Lab V, Irradiance Field Source;
6) Lab VI, Plaque Laboratory;
7) Lab VII, SeaWiFS Quality Monitor (SQM); and
8) Lab VIII, Selected Topics.

Labs I, II, V, and VII were at Little Seneca Lake. Labs II, IV, and one of the sessions in Lab VIII were at the NIST pond. The remaining exercises were in Building 221 or 245 on the NIST campus.

The questions identified in Sect. 1.2 were addressed to varying degrees in each laboratory exercise. The issue of simultaneous *in situ* measurements was addressed in the in-water activities. Assessing the accuracy of the radiometric calibration of the instruments consisted of NIST personnel performing calibrations at NIST before, after, and during SIRREX-5. The question of instrument stability between the laboratory and the field was the prime objective of Lab V. The remaining laboratories were designed to identify overlooked measurement issues, provide training, investigate the calibration methods and protocols used by the oceanographic community, and provide opportunities for discussion. The results and lessons learned from each activity are discussed in the relevant sections and summarized in Sect. 8.

1.2.2 SIRREX-5 Instruments

For the in-water measurements, the basic radiometric quantities measured are the downwelling, in-air, spectral irradiance at the surface of the water, $E_s(0^+, \lambda)$; the downwelling, in-water, spectral irradiance as a function of depth, $E_d(z, \lambda)$; and the upwelling, in-water, spectral radiance as a function of depth, $L_u(z, \lambda)$. The depth variable is z, with 0^+ and 0^- denoting just above and just below the surface. For the in-air techniques, the basic radiometric quantities measured are the radiance of the surface of the water $L_{\mathrm{sfc}}(\lambda)$, of a reference plaque (diffuse) reflector $L_{\mathrm{p}}(\lambda)$, and of the sky $L_{\mathrm{sky}}(\lambda)$, along with the downwelling irradiance at the surface. All of the radiometers used in SIRREX-5 are listed in Table 2.

The field radiometers are classified by the aforementioned basic capabilities and given a reference code (Table 2). The three character instrument designations are derived from the laboratory that supplied the sensor (first character: see column labeled "Owner"), the measurement environment (second character: "W" for in-water, and "A" for in-air), and the quantity measured [third character: "R" for radiance, usually $L_u(z, \lambda)$; "I" for $E_d(z, \lambda)$, or $E_s(0^+, \lambda)$; and "E" as a substitute for "I" when required to differentiate units]. The model and serial numbers are also given in Table 2.

Two general optical designs were represented, depending on the method to select the measurement wavelength: interference filters or gratings. For the in-water experiments, a configuration of instruments with interference filters (from either BSI or Satlantic) were grouped as a set for simultaneous measurements of $E_s(0^+, \lambda)$, $E_d(z, \lambda)$, and $L_u(z, \lambda)$. The grating instruments, from ASD, used fiber optics in the optical train and this allowed the spectrograph and electronics to be located about 1 m from the measurement point. The particular ASD devices at SIRREX-5 were for in-air use only; each unit was a dual spectrograph, so that simultaneous radiance and irradiance measurements could be made. A pair of in-air filter radiometers from Satlantic, the Satlantic Airborne Sensor (SAS-II) system, is denoted GAE and GAR in Table 2. One of the two ASD units was used in the in-air experiments (SAI and SAR in Table 2). The first optic for all instruments that measured irradiance was a specially shaped transmittance diffuser which provided adequate cosine response. For the instruments at SIRREX-5 that measured radiance, a pair of co-aligned apertures limited the field of view.

All of the Satlantic sensors were 8.9 cm in diameter and had seven detector assemblies, or channels, with the measurement wavelength defined by the properties of the interference filter. One channel was centered on the mechanical axis of the sensor, and the other six were arranged symmetrically on a circle of 27.94 mm in diameter. The

Table 2. Radiometric instruments used at SIRREX-5. The SAS-II unit is composed of GAE and GAR.

SIRREX-5 Label	*Owner*	*Manufacturer*	*Model and S/N*	*Wavelength Selection*	*A/D Unit (integral)*	*Quantity Measured*
GAI	GSFC	Satlantic	OCI-200/30	Filter		$E_s(0^+, \lambda)$
GWI	GSFC	Satlantic	OCI-200/29	Filter		$E_d(z, \lambda)$
GWE	GSFC	Satlantic	OCI-200/40	Filter		$E_d(z, \lambda)$
GWR	GSFC	Satlantic	OCR-200/21	Filter		$L_u(z, \lambda)$
SWQ	GSFC	Satlantic	OCR-200/35	Filter		$L_u(z, \lambda)$
GAE	GSFC	Satlantic	OCI-200/35	Filter	MVDS-013	$E_s(0^+, \lambda)$
GAR	GSFC	Satlantic	OCR-200/28	Filter	MVDS-012	$L_{\rm sky}(\lambda)$, $L_{\rm p}(\lambda)$, $L_{\rm sfc}(\lambda)$
PWI	PML	Satlantic	OCI-200/01	Filter		$E_d(z, \lambda)$
PWR	PML	Satlantic	OCR-200/01	Filter		$L_u(z, \lambda)$
UAI	USN	Satlantic	OCI-200/42	Filter	MVDS-016	$E_s(0^+, \lambda)$
UWI	USN	Satlantic	OCI-200/37	Filter		$E_d(z, \lambda)$
UWE	USN	Satlantic	OCI-200/36	Filter		$E_d(z, \lambda)$
UWR	USN	Satlantic	OCR-200/29	Filter		$L_u(z, \lambda)$
JWI	JRC	Satlantic	OCI-200/14	Filter		$E_d(z, \lambda)$
JWR	JRC	Satlantic	OCR-200/10	Filter		$L_u(z, \lambda)$
SAE	S/CSC	Satlantic	OCI-200/045	Filter	MVDS-017	$E_s(0^+, \lambda)$
CAI	C/CSC	BSI	PRV610 9644	Filter		$E_s(0^+, \lambda)$
CWI	C/CSC	BSI	PRV600-S9643/0	Filter		$E_d(z, \lambda)$
CWR	C/CSC	BSI	PRV600-S9643/1	Filter		$L_u(z, \lambda)$
NAI	NRL	ASD	PS2-901A	Grating		$E_s(0^+, \lambda)$
NAR	NRL	ASD	PS2-901	Grating		$L_{\rm sky}(\lambda)$, $L_{\rm p}(\lambda)$, $L_{\rm sfc}(\lambda)$
SAI	S/NRL	ASD	PS2-903 9S-03239	Grating		$E_s(0^+, \lambda)$
SAR	S/NRL	ASD	PS2-903 9S-03239	Grating		$L_{\rm sky}(\lambda)$, $L_{\rm p}(\lambda)$, $L_{\rm sfc}(\lambda)$

1. GSFC is Goddard Space Flight Center, SeaWiFS Project Office, Greenbelt, Maryland;
2. USN is Naval Research Laboratory, Code 7240, Stennis Space Center, Mississippi;
3. S/CSC is National Data Buoy Center, Stennis Space Center, Mississippi;
4. C/CSC is NOAA Coastal Services Center, Charleston, South Carolina;
5. NRL is Naval Research Laboratory, Code 7212, Washington, DC; and
6. S/NRL is Naval Research Laboratory, Code 7243, Stennis Space Center, Mississippi.
7. OCI is the Ocean Color Irradiance radiometer.
8. OCR is the Ocean Color Radiance radiometer.

half-angle field of view at the 50% response point was 14° when measured in air; in water, this value decreased to 10°. Channel 7, with the longest wavelength, was in the center, and channel 1, with the shortest wavelength, could be identified by the location of the Satlantic instrument label. The label was attached to the outside of the cylindrical housing and aligned with channel 1 when viewed along the optical axis. Each channel in the irradiance sensor had its own specially shaped transmittance diffuser, to correct for spectral effects in the cosine response.

The fiber optic (in the ASD units) was coupled to the entrance slit of the monochromator at one end, and to a mount on the other end. For the irradiance system, a diffuser was attached to the irradiance mount so the fiber was flush with the inside surface of the diffuser. The irradiance mount contained a threaded hole and a spirit level as mounting aids. For the radiance channels, a cylindrical tube 1.9 cm in diameter attached to the radiance mount via a thread connection. The radiance mount had a plastic hand grip and the cylindrical tube contained a small lens and a pair of apertures for defining the field of view. The specified instrumental bandwidth was between 4–5 nm and the specified wavelength interval was 1.3 nm. The system designated "NAI" and "NAR" in Table 2 was not used during SIRREX-5, because the fiber optic, which was recently replaced, did not fit the cylindrical tube.

The analog signals from the silicon photodiodes or linear diode arrays in the instruments were converted to digital counts using analog-to-digital (A/D) converters supplied by the manufacturer as part of the overall system. The A/D converter for the in-water instruments was located near the optical sensor, enabling data transmission to the control computer over long distances using the RS-232 or RS-422 serial interface. The A/D converter for the in-air filter radiometers was integrated with the sensor or connected to it using a short cable. For the ASD instruments, the A/D converter was incorporated into the data acquisition system supplied by the manufacturer. In Table 2, the A/D unit is indicated only if it is integral to the radiometer. Other A/D units, which can be used with

Table 3. Individual A/D units used at SIRREX-5.

SIRREX-5 Identification	*Owner*	*Manufacturer*	*Model and S/N*	*Input Voltage*
L1	GSFC	Satlantic	OCP-100/004	
L2	Satlantic	Satlantic	OCP-100/003	
L3	PML	Satlantic	TBS-001	12 V dc
L4	USN	Satlantic	OCP-100/5	
L5	GSFC	Satlantic	MVDS-009	
L6	PML	PML		12 V dc

other sensors in the same class, are given in Table 3.

To simplify the in-water laboratory, Lab I, most of the measurements were made using equipment from one manufacturer—Satlantic. This relaxed the constraints on the mounting apparatus for Little Seneca Lake because all instruments were the same size and mass; a common data acquisition system could be used also. The ASD units were used for the in-air measurements (Lab III) and the BSI instruments were used with the SQM (Lab VII), and once for the in-water measurements.

Table 4. Additional optical equipment used at SIRREX-5.

Owner	*Description*
NRL	25.4 cm square 10% reflecting Spectralon plaque
GSFC	SXR
GSFC	SQM
NIST	Field Irradiance Calibrator
NIST	60.96 cm, square; and 25.4 cm, square, 99% reflecting Spectralon plaques
NIST	10.2 cm, square, orange tile
NIST	Illuminance meter
NIST	FEL lamps (E007 and F332)
NOAA	Single channel irradiance radiometer
Satlantic	PC in crate (for SAS-II)

Additional equipment used at SIRREX-5 is identified in Table 4. The NRL group contributed a 25.4 cm, square, gray, diffuse plaque made from Spectralon. This plaque was used in the in-air experiments at the NIST pond (Lab III). The SeaWiFS Project Office contributed the SXR for use in the plaque laboratory (Lab VI) and the SQM was used at Little Seneca Lake in Lab VII. A field irradiance calibrator, designed by NIST for use in the North American interagency intercomparison of ultraviolet (UV) monitoring spectroradiometers (Early et al. 1998a), was used in Lab V at Little Seneca Lake. NIST also contributed the same 25.4 cm square, 99% reflecting Spectralon plaque which was used in SIRREX-4 [model number SRT-99-100, serial number (S/N) 12127] as well as a new 60.96 cm square, 99% reflecting Spectralon plaque (model number SRT-99-240, S/N 15107). A NIST 10 cm, square, orange tile was used during Lab III to provide a colored sample with a known spectral reflectance factor. In one of the sessions for Lab VIII, a single channel dual sensor (irradiance and radiance) was used to map the irradiance distribution of a standard irradiance lamp. This sensor, developed by NIST for NOAA's Marine Optical Buoy (MOBY) program, measures irradiance or radiance, depending on the configuration of the fore optics. NIST used a commercial irradiance meter in another of the Lab VIII experiments as a verification of $E_s(0^+, \lambda)$. Satlantic, Inc., lent a personal computer (PC) that was used for the laboratory calibration of the GAR and GAE units (the SAS-II system) and Lab III.

1.3 Document Organization

The remainder of this document is organized in the following manner. Section 2 describes the measurements at Little Seneca Lake, where simultaneous results from selected radiometers were intercompared (Labs I and II). Section 3 describes the measurements at a pond on the NIST campus, where two methods of deriving the remote sensing reflectance of the pond were implemented (Labs III and IV). For Labs I–IV, the calibration coefficients supplied by the instrument's owner were used to reduce the data. As a separate effort, NIST personnel calibrated all of the participating sensors and measured the reflectance factor of the NRL gray plaque. The NIST data for the gray plaque was used for the Lab III analysis.

Section 4 describes the use of a portable, absolute, calibration source for spectral irradiance responsivity (Lab V). The calibration coefficients derived in the field are compared to those derived in the NIST laboratory (Sect. 7). The method of generating a known source of spectral radiance using a source of known irradiance and a diffusely reflecting sample of known reflectance factor, or *the plaque method* for brevity, was the subject of Lab VI (Sect. 5). The NIST calibration procedure for spectral radiance responsivity also used the plaque method, but the data acquired prior to SIRREX-5 were not useful because of a problem with the data acquisition software. For the Satlantic radiance sensors, therefore, the comparison of the owner, and NIST, calibration coefficients is based on data

acquired by the participants during SIRREX-5 in Lab VI (Sects. 5 and 7).

Lab VII was a simple study of the stability of a new portable field source (the SQM) using the BSI sensors. The results, described in Sect. 6, were analyzed using the owner-supplied calibration coefficients, but the observed stability and repeatability is independent of these values. Section 6 also includes a summary of selected topics (Lab VIII). As mentioned above, Sect. 7 describes the NIST calibrations and presents the results. Section 8 discusses all of the SIRREX-5 results, and Sect. 9 summarizes the conclusions.

2. IN-WATER STUDIES

The major objective of the field campaign at Little Seneca Lake was to determine the level of agreement between different sensors designed to measure the same physical quantity, e.g., $L_u(z,\lambda)$, $E_d(z,\lambda)$, or $E_s(0^+,\lambda)$; to ensure comparability, the data were collected simultaneously. A secondary and implicity addressed issue was the stability of the sensors over the time period of the field measurements.

Measurements of $L_u(z,\lambda)$ and $E_d(z,\lambda)$ give information on the vertical profiles of the light field, which is related to chlorophyll *a* and other optically active components in the water. Measurements of $E_s(0^+,\lambda)$ are generally used to normalize the in-water data, e.g., to determine the remote sensing reflectance (Lab III, Sect. 3). For more information on in-water optical measurements and why they are made, see Mueller and Austin (1995) and the references therein. Analysis of the data from Little Seneca Lake was expected to be difficult because of the water properties associated with summertime conditions (i.e., algal blooms) and the limited depth of the lake, but these experimental conditions were not expected to adversely affect the primary objective: an intercomparison of simultaneous measurements and stability. For SIRREX-5, no attempt was made to determine the apparent optical properties (AOPs) of the water from the vertical profiles or to correct for possible instrument self-shading.

To simplify the experimental design, the different sensors were actually from the same manufacturer, but with separate calibration and deployment histories; almost all of the radiometers had very similar center wavelengths and bandwidths. For the results presented here, all of the instruments were Satlantic 200 series ocean color radiance (OCR-200) or irradiance (OCI-200) sensors; the former category measures $L_u(z,\lambda)$, while the latter measures either $E_d(z,\lambda)$ or $E_s(0^+,\lambda)$. Using the calibration coefficients supplied by the instrument owner, the radiance or irradiance data were intercompared as a function of time and depth. By comparison, among the calibration activities in Labs V–VII, as well as to the NIST calibration activities (Sect. 7), the stability of the radiometers can be assessed.

2.1 Site Preparation

A moored haul-down system was designed and constructed (Fig. 1). The haul-down system was designed to minimize platform shadowing and hold four in-water sensors plus two Satlantic ocean color profilers (OCP-004 and OCP-005). The OCP units contained the A/D units, pressure sensors, pitch and roll sensors, power supplies, and interface electronics. The entire apparatus consisted of two anchors, a float, the instrument frame, an anchor windlass, electrical cables, support cables, and a haul-down tether. The haul-down block assembly anchor had a stainless steel dinghy block attached to it for the haul-down tether. A separate anchor was attached to the haul-down anchor using a horizontal cable along the lake bottom (i.e., a Danforth anchor) to prevent motion of the haul-down anchor. The float was in line with the haul-down tether between the dinghy block and the instrument frame, i.e., the float was under water at all times. The electrical cables ran from the tower of the pumping station to the float; separate cables, using underwater connections, went from the float to the instrument frame. At night, the sensors were removed from the frame and the frame was stowed under water.

The system was assembled beginning 17 July and the anchors were deployed on 20 July using a rubber boat deployed from the shore near the west side of the dam at Little Seneca Lake. A wooden A–frame was built to allow the anchors to be deployed over the stern of the rubber boat. The Danforth anchor was placed approximately 45 m northwest of the pumping station tower, and the haul-down anchor was placed approximately 22 m northwest of the tower. The A–frame and its attached anchor windlass were removed from the boat and deployed on the deck of the pumping station tower to be used in hauling in, and controlling the release of, the haul-down tether. On 21 July, electrical umbilical cables were run from the pumping station building and coiled in a figure-eight pattern on the tower deck. On 22 July in the morning, the electrical cables, which were terminated with dummy connectors, were run from the tower to the float. The cables were buoyed into two catenaries to relieve the weight on the float. Four OCI-200 sensors with flotation were assembled onto the frame. On 23 July, the first day of SIRREX-5, the frame was towed to the haul-down site using the boat and the necessary connections were made. Figure 2 is a composite photograph of Little Seneca Lake and the deployment team on the rubber boat. The view is from the dam looking northwest, and the pumping station tower, haul-down line, and the frame buoy are visible.

2.2 Daily Activities

The daily activities were as follows:

- 23 July—four downwelling irradiance sensors were mounted in the instrument frame: GWI, UWI, PWI, and JWI (Table 5).

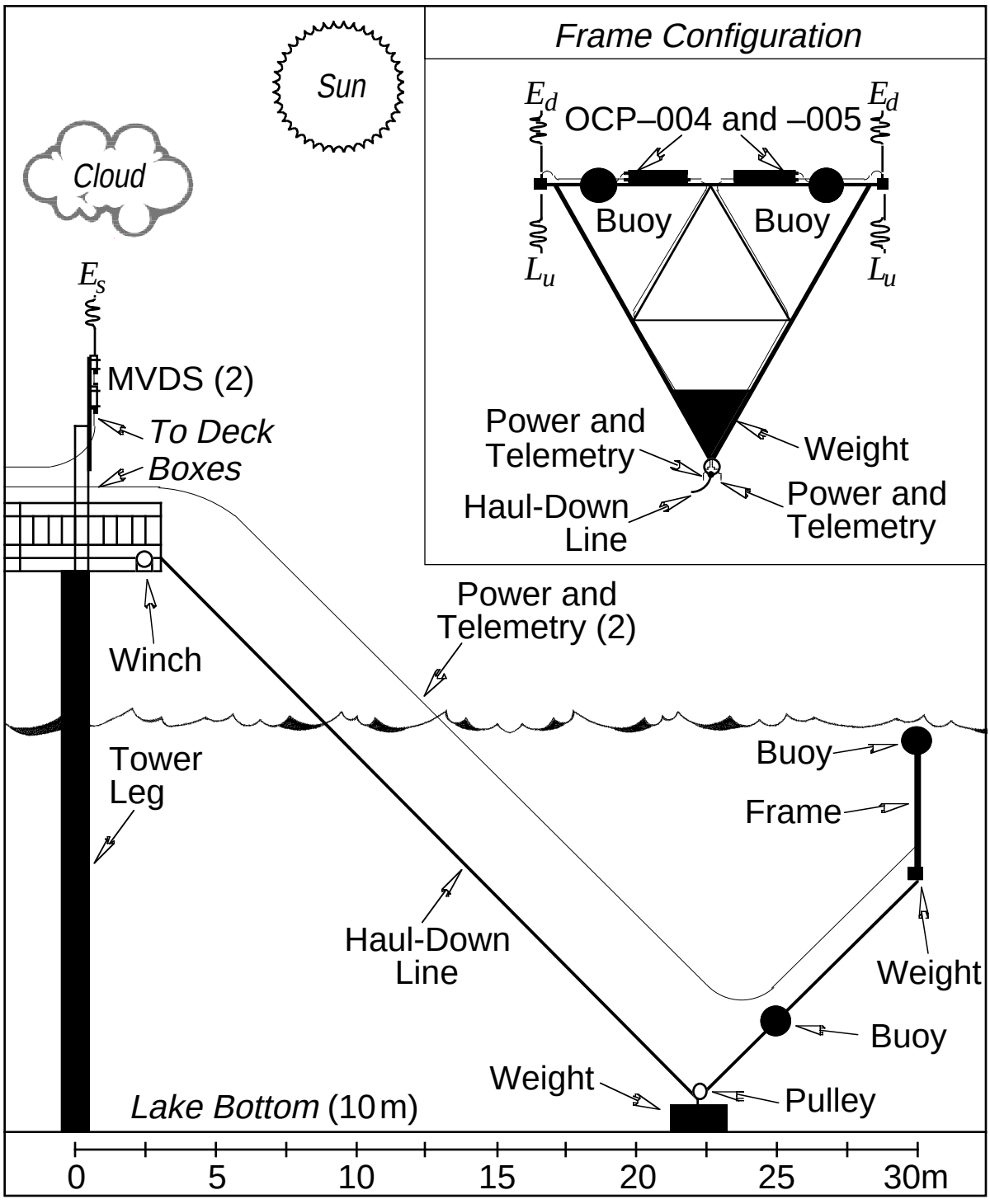

Fig. 1. A schematic of the Little Seneca Lake field site showing the relationship of the in-water equipment with respect to the pump tower. Details of the frame used to carry the light sensors are shown in the inset panel. In the insert, the view of the frame is perpendicular to the view in the overall schematic.

Table 5. A summary of the sensors and their configurations during the measurement campaign at Little Seneca Lake. The sequential day of the year (SDY) is given in the second column.

					OCP-004 Surface			*OCP-005 Surface*		
Date	*SDY*	*Time*	*Cast*	*Event*	*Port 1*	*Port 2*	*Irradiance*	*Port 1*	*Port 2*	*Irradiance*
23 July	205	1510	1	Down	PWI	UWI	GAI	GWI	JWI	SAE
23 July	205	1512	1	Up	PWI	UWI	GAI	GWI	JWI	SAE
23 July	205	1533	2	Down	PWI	UWI	GAI	GWI	JWI	SAE
23 July	205	1535	2	Up	PWI	UWI	GAI	GWI	JWI	SAE
23 July	205	1613	2	Dark	PWI	UWI		GWI	JWI	
24 July	206	1158	3	Dark				GWI	JWI	
24 July	206	1204	3	Dark	PWI	UWI				
24 July	206	1229	3	Down	PWI	UWI	GAI	GWI	JWI	
24 July	206	1234	3	Up	PWI	UWI	GAI	GWI	JWI	SAE
24 July	206	1355	4	Down	PWI	UWI	GAI	GWI	JWI	SAE
24 July	206	1357	4	Up	PWI	UWI	GAI	GWI	JWI	SAE
25 July	207	0929	5	Dark	UWR	GWR		PWR	JWR	
25 July	207	1005	5	Down	UWR	GWR	GAI	PWR	JWR	SAE
25 July	207	1007	5	Up	UWR	GWR	GAI	PWR	JWR	SAE
25 July	207	1014	6	Down	UWR	GWR	GAI	PWR	JWR	SAE
25 July	207	1024	6	Up	UWR	GWR	GAI	PWR	JWR	SAE
25 July	207	1101	7	Down	UWR	GWR	GAI	PWR	JWR	SAE
25 July	207	1103	7	Up	UWR	GWR	GAI	PWR	JWR	SAE
25 July	207	1108	8	Down	UWR	GWR	GAI	PWR	JWR	SAE
25 July	207	1110	8	Up	UWR	GWR	GAI	PWR	JWR	SAE
25 July	207	1140	9	Dark	GWI	GWR		JWI	JWR	
25 July	207	1223	9	Down	GWI	GWR	GAI	JWI	JWR	SAE
25 July	207	1225	9	Up	GWI	GWR	GAI	JWI	JWR	SAE
25 July	207	1319	10	Down	GWI	GWR	GAI	JWI	JWR	SAE
25 July	207	1321	10	Up	GWI	GWR	GAI	JWI	JWR	SAE
25 July	207	1333	11	Down	GWI	GWR	GAI	JWI	JWR	SAE
25 July	207	1335	11	Up	GWI	GWR	GAI	JWI	JWR	SAE
25 July	207	1517	12	Dark	GWI	GWR		UWE	UWR	
25 July	207	1521	12	Down	GWI	GWR	GAI	UWE	UWR	SAE
25 July	207	1523	12	Up	GWI	GWR	GAI	UWE	UWR	SAE
25 July	207	1530	13	Down	GWI	GWR	GAI	UWE	UWR	SAE
25 July	207	1533	13	Up	GWI	GWR	GAI	UWE	UWR	SAE
25 July	207	1542	13	Dark	GWI	GWR		UWE	UWR	
26 July	208	0941	14	Dark	GWI	GWR		PWI	PWR	
26 July	208	1012	14	Down	GWI	GWR	GAI	PWI	PWR	SAE
26 July	208	1014	14	Up	GWI	GWR	GAI	PWI	PWR	SAE
26 July	208	1021	15	Down	GWI	GWR	GAI	PWI	PWR	SAE
26 July	208	1023	15	Up	GWI	GWR	GAI	PWI	PWR	SAE
26 July	208	1029	16	Down	GWI	GWR	GAI	PWI	PWR	SAE
26 July	208	1031	16	Up	GWI	GWR	GAI	PWI	PWR	SAE
27 July	209	1024	17	Down	GWI	GWR	GAI	CWI	CWR	CAI
27 July	209	1026	17	Up	GWI	GWR	GAI	CWI	CWR	CAI
27 July	209	1034	18	Down	GWI	GWR	GAI	CWI	CWR	CAI
27 July	209	1036	18	Up	GWI	GWR	GAI	CWI	CWR	CAI
27 July	209	1117	19	Down	GWI	GWR	GAI	CWI	CWR	CAI
27 July	209	1120	19	Up	GWI	GWR	GAI	CWI	CWR	CAI

Fig. 2. Composite photograph of the site at Little Seneca Lake corresponding to the in-water activities. The pumping station tower, haul-down line, and frame buoy are visible. The insert is a photograph of the rubber boat used to deploy the equipment.

- 24 July—the sequence with the same four irradiance sensors was repeated.
- 23 and 24 July—no data on the roll of the instrument frame were recorded, although tilt data were.
- 25 July—four upwelling radiance sensors—GWR, UWR, PWR, and JWR, were mounted in the normal configuration (sensors facing down). The orientation of OCP-004 was adjusted, so the roll sensor would deliver more useful information. The four sensors were then inverted to measure downwelling radiance (these data should not be influenced by self-shading). Finally, the UWR and PWR sensors were replaced with GWI and JWI. The JWI and JWR sensors were in turn replaced with the UWE and UWR instruments.
- 26 July—two sets of systems were used: GWR and GWI, plus PWR and PWI.
- 27 July—the BSI sensors from C/CSC, CWR and CWI, were used with the GSFC system, GWR and GWI.
- 23–26 July—for all measurements, the surface downwelling radiometer was GAI for OCP-004, and SAE for OCP-005.
- 27 July—sensor GAI was used with the GSFC system and CAI was used with the C/CSC system.

The data acquisition consisted of a continuous down profile, recorded from the surface to a depth of approximately 8.7 m. The instrument frame was held at that depth while a fixed-depth intercomparison data set was acquired. The instrument frame was then brought to the surface, with a pause for fixed-depth intercomparison measurements at approximately 7.4 m, 3.8 m, 1.85 m, and then the surface. This set of measurements, round trip from the surface, is one cast. At each depth, data were collected at 6 Hz for between 10–15 s. The SIRREX-5 participants in the relevant group were responsible for operating the haul-down apparatus. Communication to the data acquisition activities inside (Lab II) was over marine radio.

On 29 July, the haul-down system and support equipment was removed and the site was returned to its normal state, except that both anchors were left in Little Seneca Lake. A messenger line was fed through the haul-down block and both ends were buoyed at the surface.

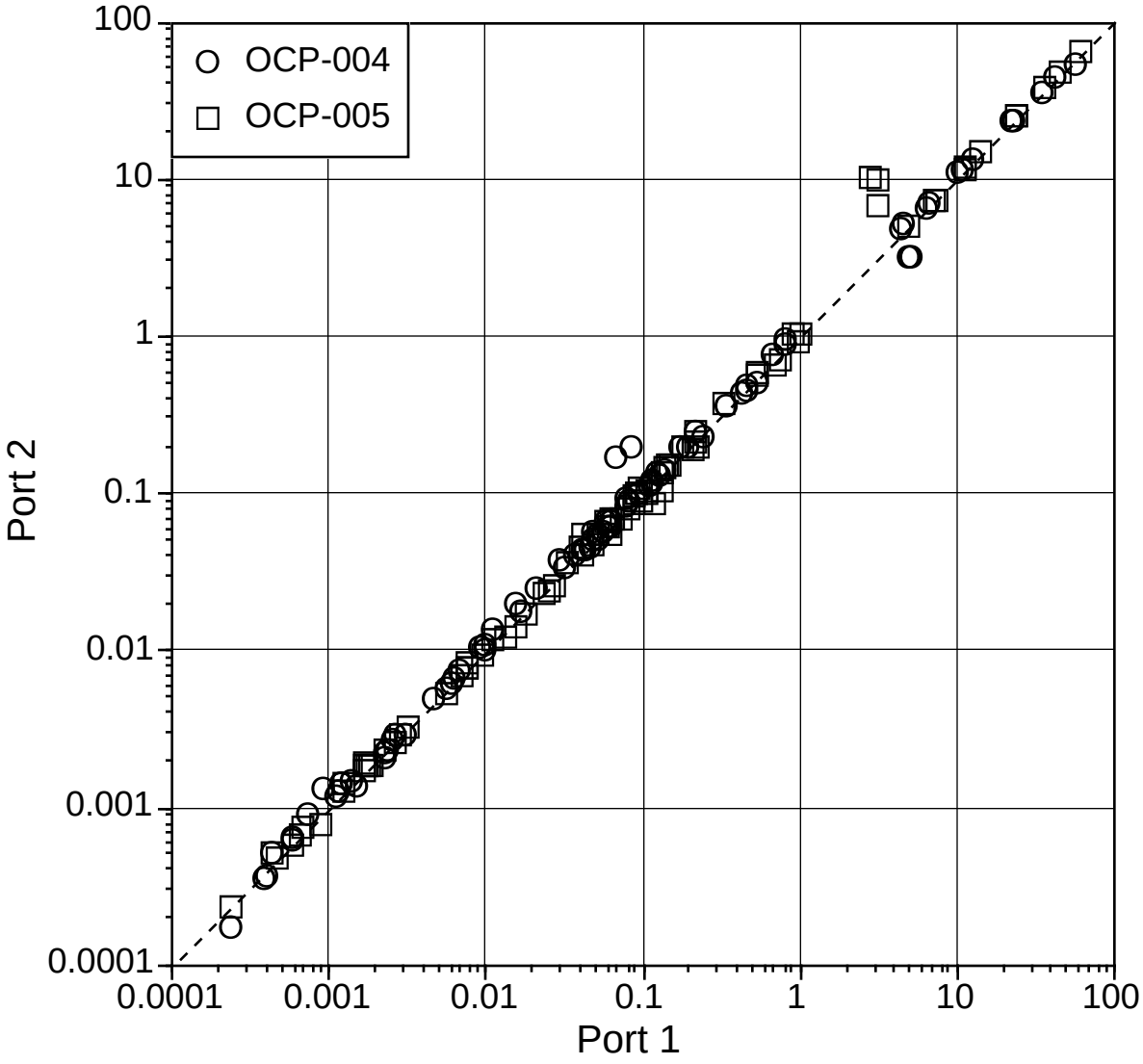

Fig. 3. A comparison of the calibrated in-water radiance and irradiance data from casts 1–8 (23–25 July 1996) during which all of the radiometers on the frame were of the same type, i.e., all radiance or all irradiance. The comparisons are between the two instruments connected to the same OCP unit and, thus, the same side of the deployment frame.

2.3 Results

Limited pitch offsets appeared to occur in some of the early data files, and significant pitch angles occurred after cast 13. This may have been related to the electrical cables. It is suspected that during the installation of a new set of sensors, the frame was twisted so that the catenary of the lead from the float to the frame could interfere with the lead from the float to the tower. Despite these difficulties, a large data set of simultaneous measurements under a variety of sky conditions was collected.

For the purposes of intercomparing the in-water measurements, the cast data can be separated into two groups: casts 1–8 and casts 9–16. The former represent those measurements when all of the sensors on the frame were of the same type (all radiance or all irradiance), whereas the latter are of mixed type (radiance and irradiance). The difference between the two sets is that for casts 1–8, all of the sensors can be intercompared (which maximizes the total number of permutations), whereas for casts 9–16 only the like sensors can be intercompared.

Figure 3 is an intercomparison of all the sensors on a particular OCP unit (OCP-004 or OCP-005) across the first five SeaWiFS wavelengths for casts 1–8, i.e., ports 1 and 2 on OCP-004, and ports 1 and 2 on OCP-005. In the common configuration for the OCP units, port 1 is the electrical input for the irradiance (OCI sensors) and port 2 is the electrical input for the radiance (OCR sensors), but the units can be operated in other configurations. The data were filtered to include only those time periods for

which light conditions were stable and the maximum pitch on the deployment frame was less than 5°. After extraction from the common depth periods during the up casts, the calibrated responses of the instruments for either $L_u(z,\lambda)$ or $E_d(z,\lambda)$ at these particular depths were averaged. If a linear regression (Type II) is applied to the Fig. 3 data, the slope of the regression line is 0.986 and $R^2 = 0.988$ (1.006 and 0.996, respectively, on log transformed data). The minor degradation in the R^2 value is due to a small number of points.

The Fig. 3 data are from radiance or irradiance sensors on the same OCP unit. It is also possible to consider sensors on different OCP units and, thus, different sides of the deployment frame. These cross relationships are formed by considering data from each port at one end of the frame versus the data from both ports at the opposite end of the frame (i.e., port 1 on OCP-004, versus ports 1 and 2 on OCP-005 plus port 2 on OCP-004, versus ports 1 and 2 on OCP-005). When all cross comparisons are pooled together, a type II regression results in a slope of 1.007 and a R^2 of 0.999 (0.989 and 0.993, respectively, for log transformed data). These lower agreements among radiometers are partly explained by slight differences in calibrations (around 2% as shown above), but most of the degradation observed for the cross comparisons actually result from the fact that the two ends of the deployment frame were at different depths because of pitch (a pitch angle of 2° induced more than 10 cm depth difference between the two ends of the frame, which is significant in turbid waters).

The other data collected at the Little Seneca Lake site was $E_s(0^+,\lambda)$ data. These data were collected with the same two sensors—GAI and SAE—which had very similar center wavelengths except for channel 7. A comparison of these two sensors, formed by calculating the ratio of the calibrated response of the SAE sensor divided by the GAI sensor for simultaneous measurements, is shown in Fig. 4. The mean ratios for channels 1–6 (i.e., the first six SeaWiFS wavelengths) are shown in Table 6 along with the standard deviation of each mean. The average ratio of all six channels is 0.995 with an average standard deviation of 0.0117. This means that the individual channels intercompare at approximately the 0.5% level, which is clearly seen in Fig. 4.

Table 6. A summary of the mean ratios and standard deviations of the SAE to GAI calibrated irradiance for channels 1–6 during casts 2, and 4–11 at Little Seneca Lake.

λ [nm]	*Mean*	σ
412	0.997	0.009
443	0.986	0.010
490	0.981	0.011
510	1.016	0.012
555	0.995	0.013
670	0.999	0.015

2.4 Discussion and Recommendations

The *in situ* intercomparisons indicate that the uncertainty in the different in-water and in-air sensors deployed at Little Seneca Lake was approximately 1–2% under the optimal light and platform (pitch) conditions. If the data set is broadened to include cross comparisons with instruments from different sides of the deployment frame, i.e., the instruments are at different depths, the uncertainty increases mostly because of the depth difference between the ends of the deployment frame. Although not all of the data was presented, the data set includes trim conditions with large tilts, which can result in intercomparison discrepancies as high as 200%. In any event, the results clearly show intercomparisons at a level in keeping with the calibration requirements as long as the effects of platform motion are negligible.

The most important lesson in this activity is the importance of platform stability, particularly in the highly attenuating environment of the lake. Pitch and roll offsets can be alleviated by using more care in rigging the electrical cables to prevent horizontal motion at the base of the instrument frame, or perhaps the installation of an electromechanical ballast for automatic trimming of the instrument frame. An accurate intercalibration of the pressure sensors would also have contributed to better control of the frame behavior, and, to a certain extent, depth measurement accuracy is relevant to radiometric data processing.

3. IN-AIR STUDIES

The ocean color protocols outline several methods that are used to determine remote sensing reflectance, $R_{\rm RS}(\lambda)$. The purpose of Lab III was to demonstrate methods for finding $R_{\rm RS}(\lambda)$ that do not require in-water radiant flux measurements. During the planning for SIRREX-5, it was clear that the site at Little Seneca Lake would not be suitable for the in-air studies; the shoreline was steep and the site was being used by Labs I, II, V, and VII, so deploying the instruments would have been difficult. Instead, the southern-most pond on the NIST campus was used.

A photograph of Lab III during SIRREX-5 is shown in Fig. 5. The pond was easy to access from the plaque laboratory, so that the irradiance and radiance calibrations of the in-air instruments could be repeated during SIRREX-5. Although the water quality of the pond was not typical of that encountered at sea, it was deemed suitable for the purpose of illustrating the concepts and investigating the stability of the radiometers. The planning prior to SIRREX-5 included discussion of moving the in-air experiment to Little Seneca Lake on the last day for a direct comparison of $R_{\rm RS}(\lambda)$, but this was not done because of the logistical issues and the fact that such a comparison was not a prime objective of SIRREX-5.

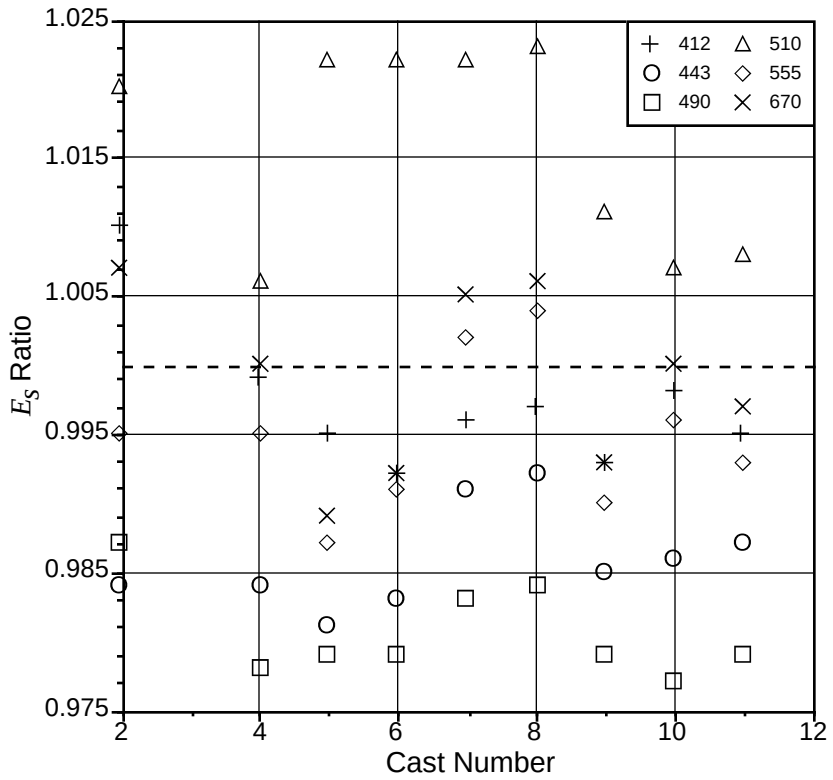

Fig. 4. A comparison of the calibrated solar irradiance $[E_s(\lambda)]$ data collected during the Little Seneca Lake in-water deployments. The data have been filtered to exclude those casts with unstable (i.e., cloudy) light fields, and only channels 1–6 of the two instruments (GAI and SAE) are shown, because the channel 7 center wavelengths were substantially different.

Fig. 5. Photograph of Lab III, illustrating the construction of the experimental platform (black plywood) over the overflow drain, the gray plaque, the SAR and SAI sensors, the GAR sensor, the data acquisition equipment, and some of the participants.

3.1 Measurement Principles

The significance of the remote sensing reflectance, $R_{\rm RS}(\lambda)$, is that it is proportional to the irradiance reflectance factor (Carder and Steward 1985). This reflecbreak tance factor can be predicted based on models and measurements of the backscattering and absorption coefficients for seawater, Gelbstoff, phytoplankton, and detritus (Carder and Steward 1985), and then related to $R_{\rm RS}(\lambda)$ if a model for the angular distribution of the upwelling light field is chosen. The remote sensing reflectance is defined as

$$R_{\rm RS}(\lambda) \;=\; \frac{\pi L_W(\lambda)}{E_s(0^+,\lambda)}, \qquad (1)$$

where $L_W(\lambda)$ is the water-leaving radiance at a particular angle of viewing and $E_s(0^+,\lambda)$ is the total downwelling irradiance. The water-leaving radiance is the radiance backscattered by the water; it does not include any incident flux reflected, either diffusely or specularly, by the surface of the water from the sky. The total downwelling irradiance is the sum, at the surface of the water, of the direct solar irradiance and any flux from the hemisphere (diffuse solar flux, flux scattered by clouds, etc.). Note that (1), from Carder and Steward (1985), differs by the factor π from the definition in the SOOP [Mueller and Austin 1995, (66)], which is incorrect.

For laboratory measurements, the quantity $R_{\rm RS}(\lambda)$ is similar to the hemispherical directional reflectance factor, which corresponds to uniform illumination (over the hemisphere) of the target with the reflected radiance measured for one direction. According to the Helmholtz reciprocity, for isotropic samples, the inverse illumination geometry is equivalent, and generally it is the directional hemispherical reflectance factor, $R(\theta/{\rm h},\lambda)$, that is measured. Here, θ is the polar angle for the incident beam and "h" stands for the hemispherical collection geometry. At NIST, $\theta = 6°$, while at Labsphere, $\theta = 8°$.

There are important differences between $R_{\rm RS}(\lambda)$ and $R(\theta/{\rm h},\lambda)$, which are worth noting. First, for $R_{\rm RS}(\lambda)$, $L_W(\lambda)$ represents the subsurface scattered radiance, as in a volume scatterer. The diffusely and specularly reflected sky components are not included. For $R(\theta/{\rm h},\lambda)$, the total flux scattered into the hemisphere is measured, independent of the scattering source (surface or volume) or directional parameters (diffuse or specular). Equating $R(\theta/{\rm h},\lambda)$ with the hemispherical directional reflectance factor $R({\rm h}/\theta',\lambda)$ means that the exitent radiance for the laboratory data includes specular reflection. Second, for $R_{\rm RS}(\lambda)$, $E_s(0^+,\lambda)$ includes both components of illumination: the direct (solar) and diffuse (sky). For $R(\theta/{\rm h},\lambda)$, the illumination is direct beam only.

The first, or *direct,* method to determine $R_{\rm RS}(\lambda)$, uses simultaneous measurements of $L_{\rm sfc}(\lambda)$ and $E_s(0^+,\lambda)$, followed by simultaneous measurements of $L_{\rm sky}(\lambda)$ and $E_s(0^+,\lambda)$. $L_{\rm sfc}(\lambda)$ is the sum of the backscattered and reflected radiance from the surface. Ideally, all three quantities should be measured at the same time, but because there is usually only a single radiance and irradiance sensor, the experiment is done in two steps. If these sensors are properly characterized and calibrated, then

$$R_{\rm RS}(\lambda) \;=\; \frac{\pi\big(L_{\rm sfc}(\lambda) \;-\; \rho_W(\lambda)L_{\rm sky}(\lambda)\big)}{E_s(0^+,\lambda)}, \qquad (2)$$

where $\rho_W(\lambda)$ is the Fresnel reflectance of the water. The value for $\rho_W(\lambda)$ is estimated to be 0.028 for low wind speeds and a viewing angle, θ', of 40° (Hooker et al. 1999). With respect to a point on the surface of the water, $L_{\rm sfc}(\lambda)$ is along an outgoing ray in direction θ',φ' and $L_{\rm sky}(\lambda)$ is along an incoming ray in direction θ,φ. Here, φ is the azimuthal angle; (2) is only valid in the case where the reflectance of the water is completely specular, so $\theta' = \theta$ and $\varphi' = \varphi + \pi$. The assumption is often made that the incident angle θ is small, and may be approximated as zero (normal incidence). In this case, the specular reflectance is the same for both states of linear polarization, which are referenced to the plane of incidence. Assuming normal incidence and a specular surface,

$$\rho_W(\lambda) \;=\; \frac{\big(n(\lambda) \;-\; 1\big)^2 + k(\lambda)^2}{\big(n(\lambda) \;+\; 1\big)^2 + k(\lambda)^2}, \qquad (3)$$

where $n(\lambda)$ and $k(\lambda)$ are the index of refraction and extinction coefficient of seawater, respectively. For the case of $\theta \neq 0$, there are two forms of (2), one for each state of polarization (DeWitt and Richmond 1988).

The second method, referred to as the *plaque method,* to determine $R_{\rm RS}(\lambda)$ uses a calibrated reflectance target and uncalibrated radiometers to measure relative radiance and irradiance. For this method to produce accurate results, the radiometers must be stable, insensitive to the polarization state of the incident flux, and linear with incident flux. The reflectance target must be spatially uniform, $R(\theta/{\rm h},\lambda)$ must be known, and these parameters must be stable. For accurate transfer from the laboratory values for $R(\theta/{\rm h},\lambda)$ to $R_{\rm RS}(\lambda)$, the reflectance target must be a perfect diffuser (e.g., lambertian), because the illumination conditions are so different. Otherwise, the radiance distribution of the sky, as well as the complete BRDF of the target, must be known. There is substantial evidence from Spectralon BRDF data that illustrates the lambertian condition is not valid (Early et al. 1999, or Fig. B2 in Johnson et al. 1996).

Typically, the target is a gray form of Spectralon with the absorptance chosen so that the reflectance is close to that of water. The analysis proceeds by assuming the target is uniform and lambertian, with reflectance $\rho_{\rm p}(\lambda)$ [equals $R(6/{\rm h},\lambda)$ using the NIST data], where the subscript "p" refers to the plaque target. Then the differences between the methods used to define or measure $R_{\rm RS}(\lambda)$ and

$R(\theta/\mathrm{h}, \lambda)$ are overlooked and the downwelling irradiance is written in terms of the radiance of the plaque as measured in the field, $L_\mathrm{p}(\lambda)$, and the reflectance determined in the laboratory:

$$E_s(0^+, \lambda) \;=\; \frac{\pi L_\mathrm{p}(\lambda)}{\rho_\mathrm{p}(\lambda)}. \qquad (4)$$

Note the similarity between (4) and (1).

The method consists of sequential radiance-mode measurements of the plaque, resulting in the signal $S_\mathrm{p}(\lambda)$; the total radiance of the water, resulting in the signal $S_\mathrm{sfc}(\lambda)$; and the radiance of the sky, resulting in signal $S_\mathrm{sky}(\lambda)$. As with the first method, the sky radiance is measured in the direction corresponding to specular reflection of the water, and the plaque and total water radiance are measured in the same direction. From (4), it is possible to write the downwelling irradiance in terms of the signal from the plaque radiance measurements, $E_s(0^+, \lambda) \propto S_\mathrm{p}(\lambda)\,\pi\rho_\mathrm{p}(\lambda)$. Then the remote sensing reflectance is

$$R_\mathrm{RS}(\lambda) \;=\; \frac{\rho_\mathrm{p}(\lambda)\big(S_\mathrm{sfc}(\lambda) \;-\; \rho_W(\lambda)\,S_\mathrm{sky}(\lambda)\big)}{S_\mathrm{p}(\lambda)}. \qquad (5)$$

The above, (5), and the comparable equation given in the SOOP [Mueller and Austin 1995, (67)] are not consistent and disagree by the factor $\rho_\mathrm{p}(\lambda)^2$ after accounting for the factor of π in the definition of $R_\mathrm{RS}(\lambda)$. However, (5) is consistent with the derivation of Carder and Steward (1985), see (10) in that paper. The error is in the Mueller and Austin document.

Variations of these two in-air methods exist. For example, the determination of the downwelling irradiance can be made using a sensor calibrated for spectral radiance and a plaque with a known reflectance factor as a substitute for the direct measurement of $E_s(0^+, \lambda)$ using the calibrated irradiance sensor. The technique in the second method for determining a signal that is proportional to the downwelling irradiance using the radiance from a diffuse reflectance target, is combined with the absolute radiance measurements in the first method; then

$$R_\mathrm{RS}(\lambda) \;=\; \frac{\rho_\mathrm{p}(\lambda)\big(L_\mathrm{sfc}(\lambda) \;-\; \rho_W(\lambda)\,L_\mathrm{sky}(\lambda)\big)}{L_\mathrm{p}(\lambda)}. \qquad (6)$$

Another variation possible in either method is to use a mirror of known reflectivity orientated in the horizontal plane to measure $L_\mathrm{sky}(\lambda)$.

The third method for determining $R_\mathrm{RS}(\lambda)$, not implemented in Lab III, relies on in-water radiant flux measurements. The upwelling radiance as a function of depth and the downwelling irradiance at the surface of the water are measured using calibrated sensors. Then, after corrections for self-shading, wave focusing, and other sources of bias, the $L_u(z, \lambda)$ data are used to estimate $L_u(0^-, \lambda)$ and this value is propagated through the surface using Fresnel's laws; then, from (1), $R_\mathrm{RS}(\lambda)$ can be determined.

In summary, there are a number of important assumptions and critical measurement parameters that must hold for an accurate determination of $R_\mathrm{RS}(\lambda)$. Because the measurements are not completely simultaneous, the illumination conditions and the radiometers must be stable. The incident and viewing angles, θ and θ', must be small, ideally at normal incidence, or else the two states of polarization must be considered separately. The reflectance target is assumed to be isotropic and lambertian, or the full BRDF must be measured for in- and out-of-plane geometries. The spectral reflectance of the water must be specular, with a negligible diffuse component. Wind-driven waves affect the reflectance, and this bias depends on the angle θ. Finally, the variation in $R(\theta/\mathrm{h}, \lambda)$ with θ should be negligible.

Lab III was structured to address some of these fundamental issues and assumptions. $R_\mathrm{RS}(\lambda)$ was derived using (2) and (6), and these independent determinations are compared. An orange tile with a known reflectance factor was measured outdoors as a special test. Performance of the measurements outdoors in conditions somewhat analogous to those on a ship was expected to result in a reasonable estimate of the variance caused by clouds, increased temperatures, and so forth. The participants in Lab III were actively involved in performing the actual measurements, including mounting and aligning the radiometers and the reflectance targets.

3.2 Daily Activities

The two instruments used for measuring the remote sensing reflectance were the SAS-II, consisting of two filter radiometers, each with seven channels; and a dual-grating spectrograph manufactured by ASD with fiber-optic input (SAI and SAR). Both instruments could measure radiance and irradiance simultaneously. The instruments were calibrated for irradiance and radiance responsivity at NIST during SIRREX-5, and the NIST calibration factors are used in the analysis presented here. For brevity, the SAI and SAR system will be described using the model number PS2-903.

The daily procedure was to measure the remote sensing reflectance at the pond site first with the PS2-903, then with the SAS-II, and then again with the PS2-903. Simultaneous measurements with the two instruments were not performed. The fiber-optic input of the PS2-903 dual spectrograph was respectively fitted with a cosine collector for irradiance and an 18° field-of-view aperture pair for radiance. The experimental procedure for the PS2-903 was to first measure the gray plaque radiance, then the water radiance followed by the sky radiance. Figure 6 is a photograph taken during the alignment of the SAR sensor. The sky irradiance measurements were done simultaneously with all of the corresponding radiance measurements. The entire cycle of plaque-water-sky took little over a minute and the cycle was repeated five times for a single set. The experimental procedure for the SAS-II instrument was to first

Fig. 6. Photograph during Lab III, illustrating the method used to align the radiance sensors (SAR in this case) to the diffuse plaque. For measurements of $L_{\rm sfc}$, the tripod with the sensor was moved to the edge of the experimental platform.

measure the plaque radiance and then the water radiance, but was occasionally followed by sky radiance measurements. A single cycle with the SAS-II took about two minutes, and each cycle was saved in separate files. The sky irradiance was also measured simultaneously with the radiance measurements. On some occasions, the SAS-II channels were saturated by the sky radiance. The PS2-903 did not saturate under any conditions.

The experimental procedure was changed on the second and third days of the experiment to include a glossy, colored tile of a known reflectance factor. The radiance from the tile was measured in place of $L_{\rm sfc}(\lambda)$.

The measurement geometry was similar for the plaque, water, and tile data sets. The plaque or tile was horizontal, and the direction of direct solar illumination was always orthogonal to the plane of measurement for $L_{\rm sfc}(\lambda)$, $L_{\rm p}(\lambda)$, and $L_{\rm sky}(\lambda)$. Referenced to a point on the target, the polar and azimuthal angles for the incident direct solar beam varied with the time of day. The polar angle, θ, for the $L_{\rm sfc}(\lambda)$, $L_{\rm p}(\lambda)$, and $L_{\rm sky}(\lambda)$ measurements was either 20°, 30°, or 45°. The radiance sensor for the SAS-II or the PS2-903 was mounted on a tripod, located on a small dock at the edge of the pond. The tripod was moved to the edge of the dock for the $L_{\rm sfc}(\lambda)$ measurements. The plaque or tile sat on a small table which was moved in front of the tripod for the reflected radiance measurements. The irradiance sensors for the SAS-II or the PS2-903 were mounted on a second tripod, about 1.8 m above the dock.

3.3 Analysis

In the direct method, the remote sensing reflectance for both the PS2-903 and the SAS-II, $R_{\rm RS,c}$ was determined using (2), so

$$R_{\rm RS,c} \;=\; \frac{\pi}{n}\sum_{j=1}^{n}\left(\frac{L_{\rm sfc}(t)}{E_s(t)} \;-\; \rho_W\,\frac{L_{\rm sky}(t')}{E_s(t')}\right), \qquad (7)$$

where t and t' represent the time of the measurements, n is the number of samples, "c" stands for calibrated, and the dependence with wavelength is understood. The number of samples ranged from 5 for the PS2-903 instrument to over 100 for the SAS-II instrument.

In the plaque method, the remote sensing reflectance $R_{\rm RS,p}$ is determined by,

$$R_{\rm RS,p} \;=\; \frac{1}{n}\sum_{j=1}^{n}\rho_{\rm p}\left(\frac{L_{\rm sfc}(t)}{L_{\rm p}(t')} \;-\; \rho_W\,\frac{L_{\rm sky}(t'')}{L_{\rm p}(t')}\right), \qquad (8)$$

where $\rho_{\rm p}$ is the gray plaque reflectance factor measured in the laboratory; t, t', and t'' are measurement times; and $L_{\rm p}(t')$ is the radiance from the plaque measured in the

field. The number of samples, n, also ranged from 5 for the measurements using the PS2-903 instrument, to over 100 for the SAS-II instrument.

3.4 Results

3.4.1 24 July 1996

The sky was scattered with clouds. During the morning, a green scum was on the surface of the pond, but this dissipated by midday. The details of the measurements are given in Table 7, where the files for the SAS-II instrument are denoted as a group and labeled by the time at which the measurements were taken. For all of the SAS-II measurements, $\theta = 30°$; for the PS2-903 measurements, the value was not recorded, although it was not varied. Every measurement of $L_{\rm sky}(\lambda)$ was saturated for the SAS-II instrument, so no results are presented for 24 July.

Table 7. The filenames and the times for the remote sensing reflectances were measured using the PS2-903 and the SAS-II instruments at the NIST pond on 24 July 1996.

Filename	*Time*	*Instrument*
960724a	10:52–10:58	PS2-903
960724b	11:03–11:09	PS2-903
960724c	11:14–11:19	PS2-903
—	13:02–13:17	SAS-II†
960724d	13:31–13:37	PS2-903

† 10 measurements.

The remote sensing reflectance with the PS2-903 instrument is shown in Figs. 7 and 8 using the direct method and the plaque method, respectively. The reflectance is a strong function of wavelength with a maximum value of about 550 nm. The ratio $R_{\rm RS,c}$:$R_{\rm RS,p}$ is shown in Fig. 9. The values for $R_{\rm RS,c}$ and $R_{\rm RS,p}$ are in good agreement for the first three PS2-903 files: 960724a, 960724b, and 960724c. The value for $R_{\rm RS,c}$ is several percent greater than $R_{\rm RS,p}$ in the range from about 420–680 nm. For file 960724d, the discrepancy is much larger, from 20–30% and in the same direction, $R_{\rm RS,c} > R_{\rm RS,p}$. The average and standard deviations of these ratios for the PS2-903 are given in Table 8.

Table 8. Comparison of $R_{\rm RS,c}$ and $R_{\rm RS,p}$ for the PS2-903 measurements on 24 July 1996. The values correspond to the quantity $(R_{\rm RS,c} - R_{\rm RS,p})/\,R_{\rm RS,p}$ ($\overline{\Delta}'$) in percent, for the wavelength range from 420–680 nm. The relative standard deviation (σ') of this ratio is also given.

Filename	$\overline{\Delta}'$ [%]	σ' [%]
960724a	2.4	1.7
960724b	3.8	1.8
960724c	2.4	2.0
960724d	22.3	3.1

3.4.2 25 July 1996

The field measurements were performed in a similar way as on 24 July 1996. The times and filenames are reported in Table 9. For the SAS-II and the PS2-903 measurements, $\theta = 45°$. Figures 10 and 11 show the remote sensing reflectance measured using the PS2-903: $R_{\rm RS,c}$ and $R_{\rm RS,p}$, respectively. Figure 12 illustrates the ratio $R_{\rm RS,c}$:$R_{\rm RS,p}$. From Fig. 12, the $R_{\rm RS}$ values for the two methods from files 960725b and 960725d are in good agreement with each other; the average difference, for the wavelength range from 420–680 nm is less than 4%. The data set 960725a gives a larger discrepancy (Fig. 12 and Table 10); as with the 24 July PS2-903 data, $R_{\rm RS,c} > R_{\rm RS,p}$ for all three data sets.

Table 9. The filenames and the times for the remote sensing reflectances measured using the PS2-903 and the SAS-II instruments at the NIST pond on 25 July 1996.

Filename	*Time*	*Instrument*
960725a	12:06–12:10	PS2-903
960725b	13:19–13:26	PS2-903
960725c	13:37–13:42	PS2-903†
—	14:01–14:21	SAS-II‡
960725d	14:44–14:48	PS2-903

† Orange tile. ‡ 7 measurements.

Table 10. Comparison of $R_{\rm RS,c}$ and $R_{\rm RS,p}$ for the PS2-903 measurements on 25 July 1996. The values correspond to the quantity $(R_{\rm RS,c} - R_{\rm RS,p})/\,R_{\rm RS,p}$ in percent, for the wavelength range of 420–680 nm. The relative standard deviation of this ratio is also given.

Filename	$\overline{\Delta}'$ [%]	σ' [%]
960725a	8.4	1.5
960725b	3.9	1.8
960725d	1.9	1.6

The average and the standard deviation of the remote sensing reflectances for the seven measurements with the SAS-II instrument are also shown in Figs. 10 and 11. In these figures, the average values are denoted by open circles and the corresponding standard deviations are denoted as vertical lines. The values for $R_{\rm RS,c}$ are consistently greater than $R_{\rm RS,p}$ (Fig. 12 and Table 11). In addition, the values of $R_{\rm RS,c}$ have less scatter and thus, smaller standard deviations.

For each of the seven separate measurements with the SAS-II instrument, the values of the average, over wavelength, percent difference between $R_{\rm RS,c}$ and $R_{\rm RS,p}$ are given in Table 12. The standard deviations, as seen in the third column in Table 12, remain constant in time, even though the average relative difference changes by over a factor of 20.

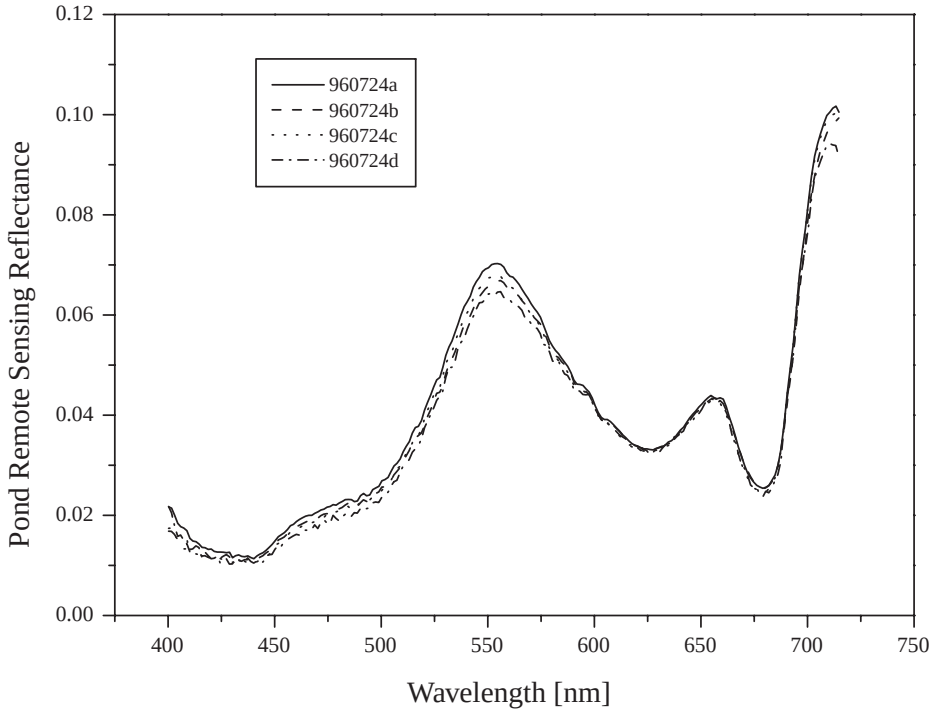

Fig. 7. The results for $R_{\mathrm{RS,c}}$ for the 24 July 1996 measurements. Four PS2-903 data sets were acquired (Table 7) and the filenames are indicated in the legend.

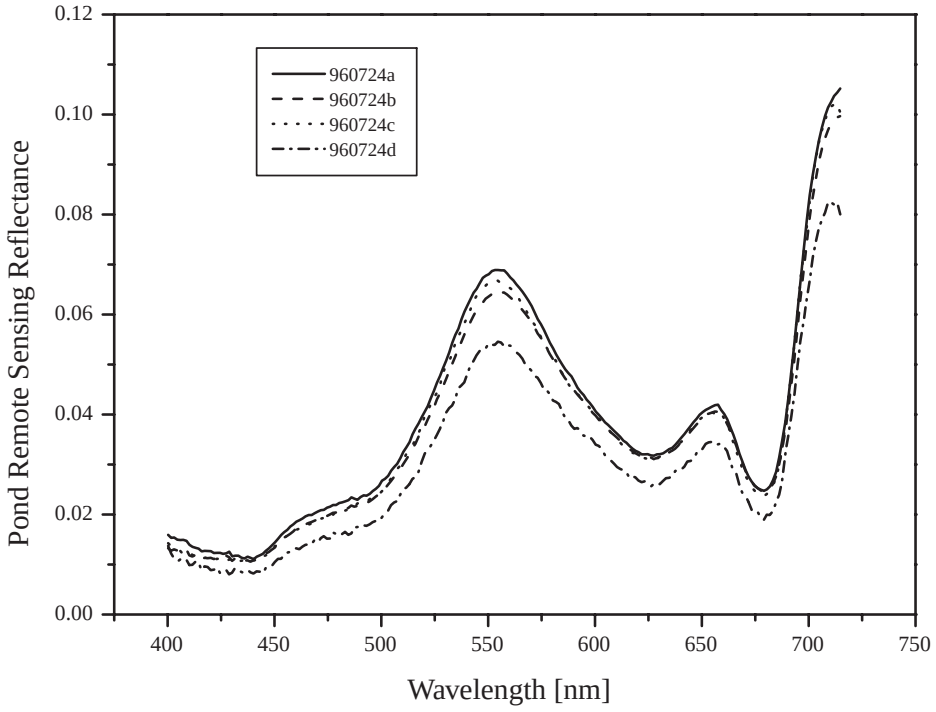

Fig. 8. The results for $R_{\mathrm{RS,p}}$ for the 24 July 1996 measurements. Four PS2-903 data sets were acquired (Table 7) and the filenames are indicated in the legend.

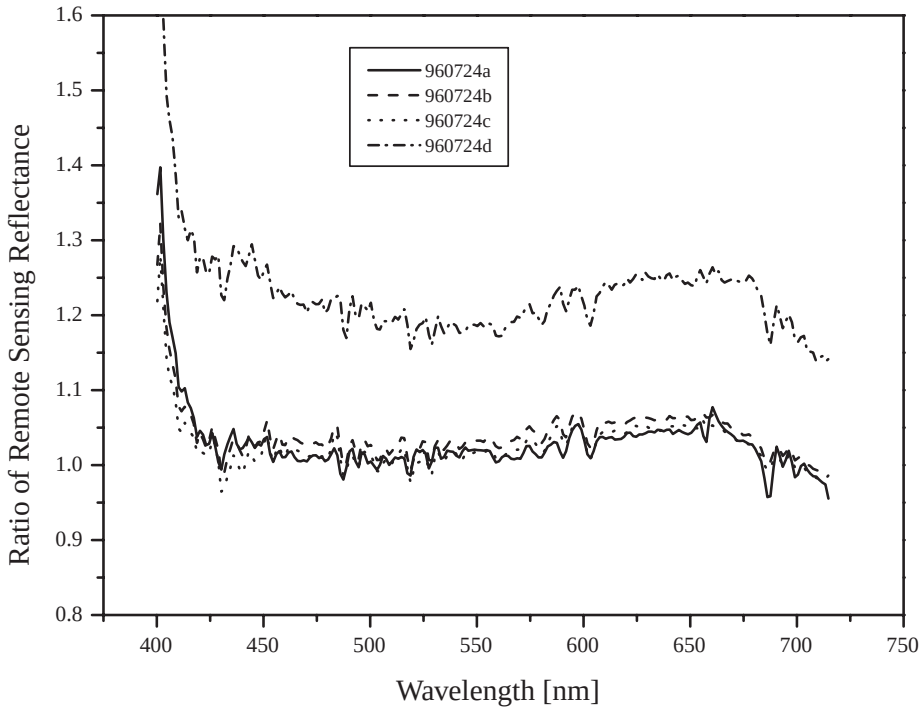

Fig. 9. The ratio $R_{\mathrm{RS,c}}$:$R_{\mathrm{RS,p}}$ as determined from measurements on 24 July 1996 at the pond site using the PS2-903. The filenames for the PS2-903 data sets are indicated in the legend.

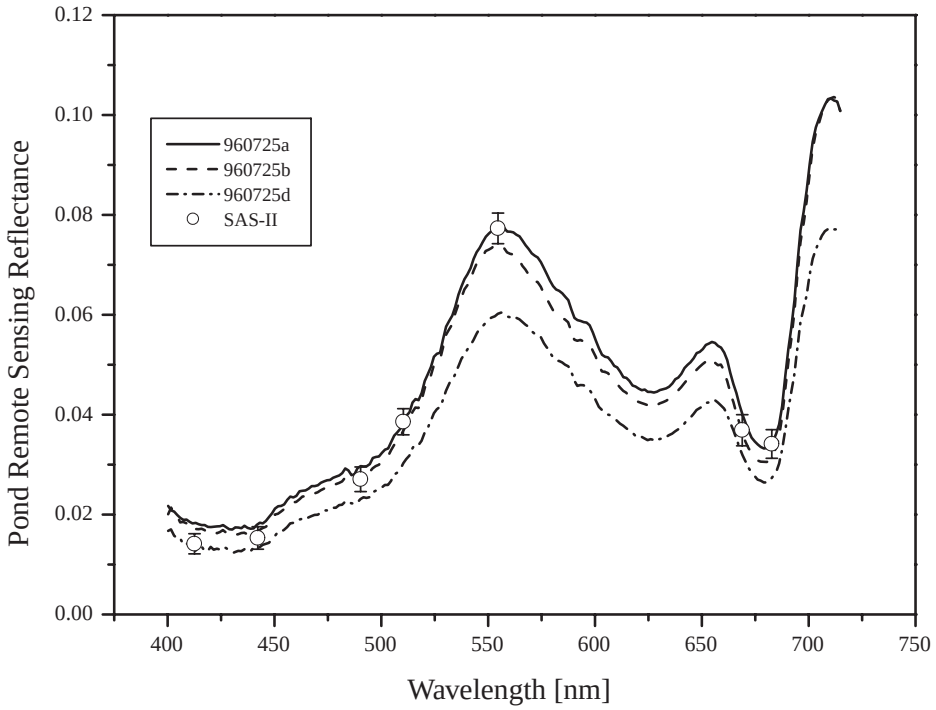

Fig. 10. The results for $R_{\mathrm{RS,c}}$ for the 25 July 1996 measurements. Three PS2-903 data sets were acquired (Table 9) and the filenames are indicated in the legend. The average values obtained from the seven SAS-II measurements are shown as open circles with the standard deviations shown as vertical lines.

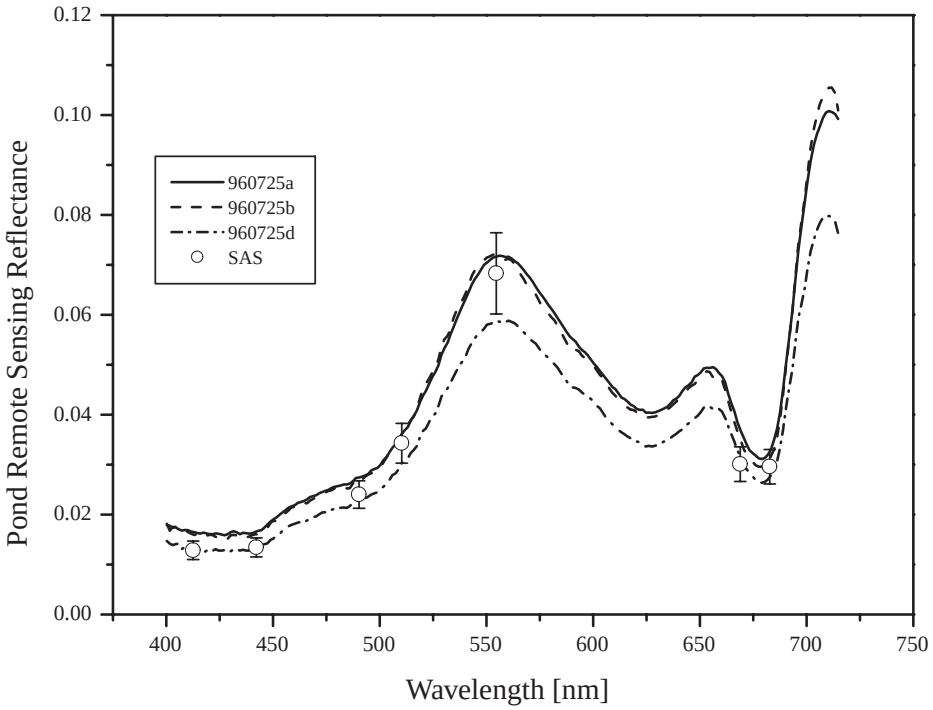

Fig. 11. The results for $R_{\mathrm{RS,p}}$ for the 25 July 1996 measurements. Three PS2-903 data sets were acquired (Table 9) and the filenames are indicated in the legend. The average values obtained from the seven SAS-II measurements are shown as open circles with the standard deviations shown as vertical lines.

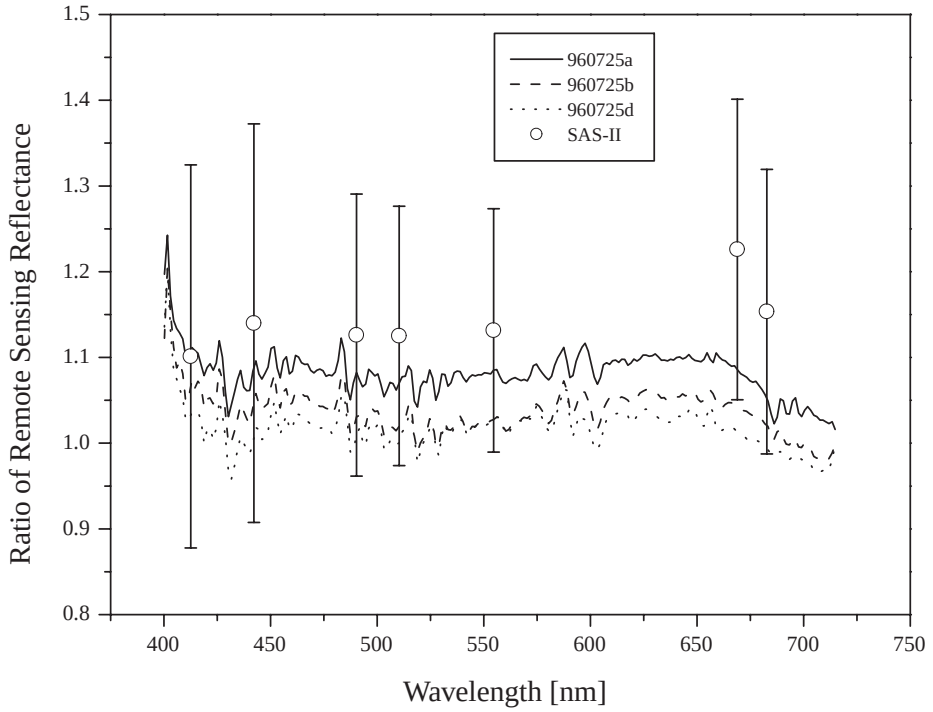

Fig. 12. The ratio $R_{\mathrm{RS,c}}$:$R_{\mathrm{RS,p}}$ as determined from measurements on 25 July 1996 at the pond site using the PS2-903 and the SAS-II instrument (open circles). The filenames for the PS2-903 data sets are indicated in the legend. The vertical lines represent the uncertainty in the ratio of the reflectances for the SAS-II data obtained from the standard deviations.

Table 11. The SAS-II results on 25 July for R_{RS} using the calibrated method and the plaque method with the corresponding standard deviations.

λ [nm]	$R_{\mathrm{RS,c}}$	σ' $R_{\mathrm{RS,c}}$ [%]	$R_{\mathrm{RS,p}}$	σ' $R_{\mathrm{RS,p}}$ [%]
412.6	0.0141	14.3	0.0128	14.4
442.2	0.0153	14.7	0.0134	14.1
490.3	0.0271	9.1	0.0240	11.4
510.3	0.0386	6.8	0.0343	11.6
554.6	0.0773	4.0	0.0683	11.9
668.9	0.0369	8.5	0.0301	11.5
682.7	0.0341	8.4	0.0296	11.7

Table 12. Comparison of $R_{\mathrm{RS,c}}$ and $R_{\mathrm{RS,p}}$ for the seven individual SAS-II measurements on 25 July 1996. The values correspond to the average, over the SAS-II wavelengths, of the quantity $(R_{\mathrm{RS,c}} - R_{\mathrm{RS,p}})/\,R_{\mathrm{RS,p}}$ in percent. The relative standard deviation of this ratio is also given.

Filename	$\overline{\Delta}'$ [%]	σ' [%]
B0135	15.9	5.0
B1031	4.2	4.3
B1220	3.3	3.0
B1304	1.8	2.8
B1355	5.6	2.9
B1933	41.2	7.6
B2121	37.3	5.3

3.4.3 26 July 1996

The sky was scattered with clouds, but care was taken to do the measurements only in direct sunlight. Table 13 lists the filenames and measurement times; as on 25 July, for the SAS-II measurements, $\theta = 45°$. This angle was varied for the PS2-903 measurements and is listed in Table 13. The values for $R_{\mathrm{RS,c}}$ and $R_{\mathrm{RS,p}}$ using the PS2-903 are shown in Figs. 13 and 14, respectively. Table 14 lists the ratios $R_{\mathrm{RS,c}}$:$R_{\mathrm{RS,p}}$. With the exception of file 960726a, the $R_{\mathrm{RS,p}}$ values are greater than the $R_{\mathrm{RS,c}}$ values (Fig. 15). This tendency is the reverse of the previous days for the PS2-903, where $R_{\mathrm{RS,c}} > R_{\mathrm{RS,p}}$. The standard deviation of the reflectance ratios are nearly equal for each measurement set, indicating a systematic change in one or both of the R_{RS} values.

The reflectances measured with the SAS instrument are also plotted in Figs. 13 and 14. For the SAS-II, $R_{\mathrm{RS,c}}$ is greater than $R_{\mathrm{RS,p}}$; however, the direct method produced somewhat lower standard deviations, as seen in Table 15. Although the SAS-II instrument was used in between the PS2-903 measurements (Table 13), the PS2-903 reflectance ratios do not bracket the SAS-II ones. For the SAS-II results, the average, over wavelength, of the quantity $(R_{\mathrm{RS,c}} - R_{\mathrm{RS,p}})/\,R_{\mathrm{RS,p}}$ is given in Table 16 for each of the nine separate measurements.

Table 13. The filenames and the times for the remote sensing reflectances measured using the PS2-903 and the SAS-II instruments at the NIST pond on 26 July 1996.

Filename	Time	Instrument	θ [°]
960726a	11:20–11:23	PS2-903	45
960726b	11:28–11:31	PS2-903	30
960726c	11:34–11:37	PS2-903	20
960726d	11:42–11:44	PS2-903†	20
—	12:02–12:25	SAS-II‡	45
960726e	13:39–13:41	PS2-903	45
960726f	13:49–13:53	PS2-903	45
960726g	14:01–14:04	PS2-903†	45

† Orange tile. ‡ 9 measurements.

Table 14. Comparison of $R_{\mathrm{RS,c}}$ and $R_{\mathrm{RS,p}}$ for the PS2-903 measurements on 26 July 1996. The values correspond to the quantity $(R_{\mathrm{RS,c}} - R_{\mathrm{RS,p}})/\,R_{\mathrm{RS,p}}$ in percent, for the wavelength range of 420–680 nm. The relative standard deviation of this ratio is also given.

Filename	$\overline{\Delta}'$ [%]	σ' [%]
960726a	1.7	1.8
960726b	−2.6	1.8
960726c	−10.3	1.5
960726e	−13.3	1.5
960726f	−11.4	1.2

Table 15. The SAS-II results on 26 July for R_{RS} using the calibrated method and the plaque method with the corresponding standard deviations.

λ [nm]	$R_{\mathrm{RS,c}}$	σ' $R_{\mathrm{RS,c}}$ [%]	$R_{\mathrm{RS,p}}$	σ' $R_{\mathrm{RS,p}}$ [%]
412.6	0.0141	5.5	0.0132	5.6
442.2	0.0159	5.2	0.0147	5.5
490.3	0.0258	3.4	0.0248	4.5
510.3	0.0357	2.6	0.0348	6.4
554.6	0.0691	1.3	0.0670	3.0
668.9	0.0377	3.0	0.0340	3.3
682.7	0.0346	3.4	0.0329	4.3

3.5 Discussion and Recommendations

The only difference between the direct method and the plaque method is the method of determining the sky irradiance; the direct method measures this quantity directly, (6), while the plaque method determines it from the plaque radiance and known values for the plaque reflectance, (7). Any difference between the remote sensing reflectances found using the two methods, therefore, could be due to the environmental conditions, the illumination geometry, systematic effects associated with the derivation of the downwelling irradiance from the reflected plaque radiance, or problems with the $E_s(\lambda, t)$ radiometers (such

Table 16. Comparison of $R_{\mathrm{RS,c}}$ and $R_{\mathrm{RS,p}}$ for the nine individual SAS-II measurements on 24 July 1996. The values correspond to the average, over the SAS-II wavelengths, of the quantity $(R_{\mathrm{RS,c}} - R_{\mathrm{RS,p}})/\,R_{\mathrm{RS,p}}$ in percent. The relative standard deviation of this ratio is also given.

Filename	$\overline{\Delta}'$ [%]	σ' [%]
B1154	1.4	5.1
B1250	9.0	2.4
B1444	4.9	3.6
B1815	7.6	2.4
B1550	8.8	2.6
B2017	7.0	2.1
B2227	6.7	2.3
B2418	2.8	4.4
B1346	3.7	2.4

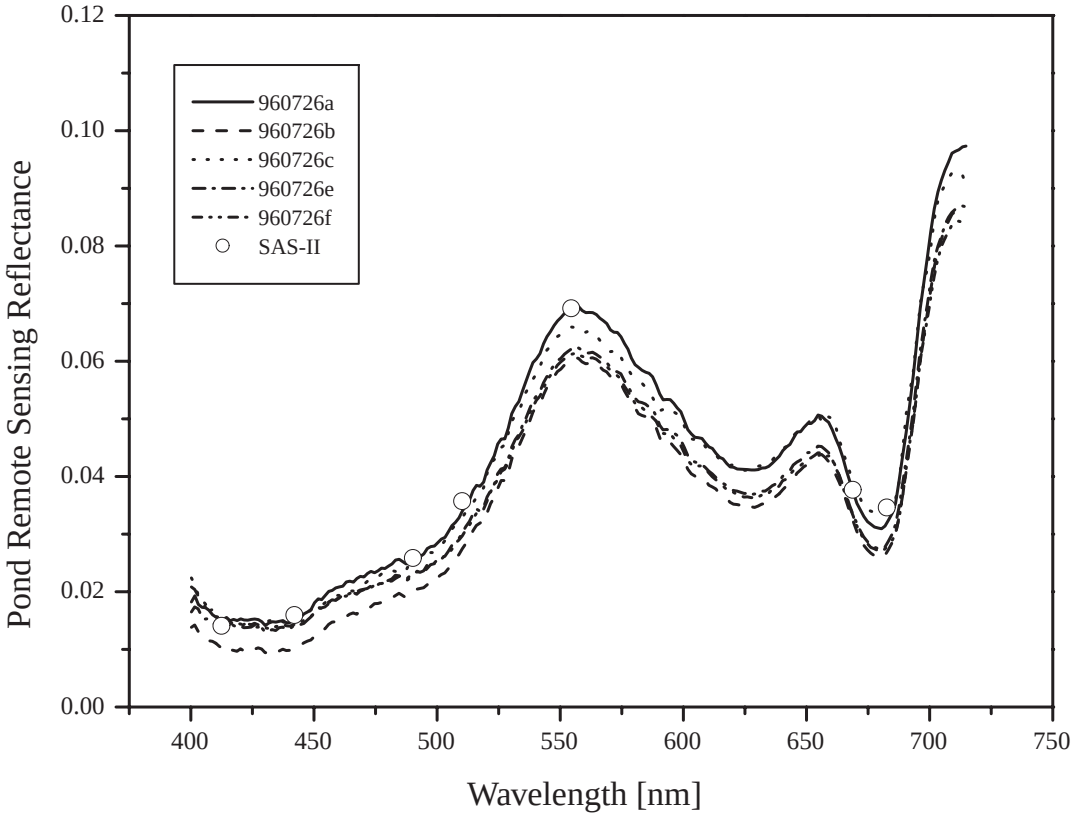

Fig. 13. The results for $R_{\mathrm{RS,c}}$ for the 26 July 1996 measurements. Five PS2-903 data sets were acquired (Table 13) and the filenames are indicated in the legend. The average values obtained from the nine SAS-II measurements are shown as open circles; for clarity, the standard deviations are not shown because they correspond to the size of the plotted symbol.

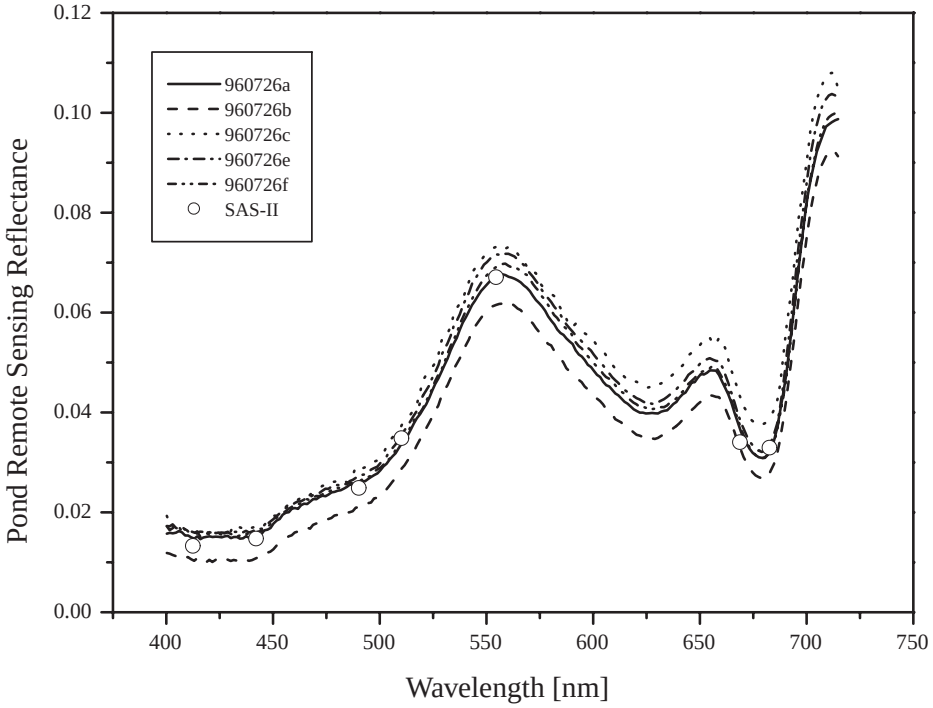

Fig. 14. The results for $R_{\mathrm{RS,p}}$ for the 26 July 1996 measurements. Five PS2-903 data sets were acquired (Table 13) and the filenames are indicated in the legend. The average values obtained from the nine SAS-II measurements are shown as open circles; for clarity, the standard deviations are not shown because they correspond to the approximate size of the plotted symbol.

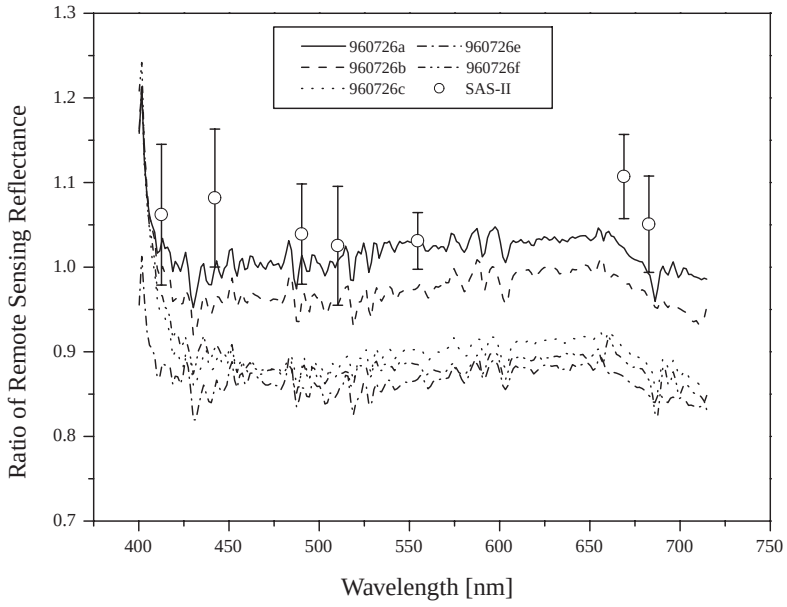

Fig. 15. The ratio $R_{\mathrm{RS,c}}$:$R_{\mathrm{RS,p}}$ as determined from measurements on 26 July 1996 at the pond site using the PS2-903 and the SAS-II instrument (open circles). The filenames for the PS2-903 data sets are indicated in the legend. The vertical lines represent the uncertainty in the ratio of the reflectances for the SAS-II data obtained from the standard deviations.

as the cosine response of the individual channels). For the SAS-II results on a given day, the standard deviations were somewhat less for $R_{\mathrm{RS,c}}$ compared to $R_{\mathrm{RS,p}}$ (Tables 11 and 15).

For each of the three days, the sky conditions were clear to partly cloudy. On 26 July, all measurements were made when clouds were not blocking the sun, but this may not have been true for the 24 and 25 July data. Increased awareness by the participants to the significance of the variable sky conditions during SIRREX-5 may explain the improvement in the standard deviations for the SAS-II results over time (Tables 11 and 15). The presence of wind-driven waves on the pond surface, which would have varied with time, could explain some of the variability in the results. For example, with a uniform sky and a viewing angle of 30°, wind-driven surface waves increase the reflectance of the surface for the reflected sky component relative to the Fresnel value, (3). Atmospheric conditions, such as water vapor and aerosols, affect the diffuse sky component, but these were not quantified as part of SIRREX-5.

The PS2-903 measurements occur over a greater time interval than the SAS-II ones, with a corresponding increase in the range of solar illumination angles. The temporal variation of the PS2-903 R_{RS} results is seen in Figs. 9, 12, and 15. On 24 July, the first three PS2-903 measurements took place during a 27 min interval; the fourth measurement was 2.3 h later. On 25 July, 1.2 h and 1.4 h separated the three PS2-903 data sets, respectively. On 26 July, the first three PS2-903 data sets (960726a, 960726b, and 960726c) took 24 min to obtain, and occurred at about the same time of day as the three consecutive data sets on 24 July. Unlike the 24 July results, which were in agreement, the ratio $R_{\mathrm{RS,c}}$:$R_{\mathrm{RS,p}}$ changed by up to 15%; however, θ was different for each of the first three 26 July data sets: 45°, 30°, and 20°, respectively. The last two 26 July data sets took place about 2 h later than set 960726c (Table 13). Inspection of the ratios $R_{\mathrm{RS,c}}$:$R_{\mathrm{RS,p}}$ for the PS2-903 at $\theta = 45°$ for the three days does not reveal a strong correlation with time of day; with the exception of data sets 960724d, 960726e, and 960726f, the ratios are all between 1.0 and 1.1.

Issues relating to the use of the reflected radiance from a diffusely reflecting standard to determine the total downwelling irradiance were discussed in the introduction to this section. Because such reflecting standards are not lambertian (Early et al. 1999), the plaque method should not be used unless the measurement equation is expanded to include the distribution of sky radiance and full BRDF plaque data.

4. IRRADIANCE FIELD SOURCE

The motivation for Lab V was the lack of traceability between laboratory calibrations and field measurements. The calibration coefficients for downwelling irradiance sensors were determined in the field using an absolute standard of spectral irradiance. The objectives of Lab V were to determine the stability of the radiometers during SIRREX-5 and to compare the laboratory and field calibration. The measurements at SIRREX-5 are useful for sensor evaluation, although they are not practical for *in situ* ocean color measurements because of the typical position of the downwelling irradiance sensor on a tall mast and the motion of the ship.

4.1 Field Calibrator

The field irradiance calibrator was made for the North American interagency intercomparison of UV monitoring spectroradiometers—the UV intercomparisons (Early et al. 1998a and 1998b). The field calibrator is an absolute source for spectral irradiance. The principle of operation is the kinematic location of an FEL lamp in the horizontal position 50 cm from the input aperture of the irradiance collector on a field spectroradiometer. Operation in full sunlight is possible because the field calibrator is enclosed in a light-tight shroud. The stray radiation from the 1,000 W FEL lamp is trapped within the unit, and a fan maintains the temperature at about 150°C for the plate closest to the lamp. The FEL lamp used in Lab V, E007, was calibrated for operation in the horizontal position prior to SIRREX-5. A photograph of the equipment used in Lab V is shown in Fig. 16.

The field irradiance calibrator, when it is configured for the UV intercomparisons, uses the field instruments for the mechanical support. These instruments are self-supporting, and they are tethered to concrete pads during the intercomparison. A custom base plate and the mechanical standoffs kinematically mate the UV spectroradiometer to the field calibrator. Because the field radiometers in the ocean color community are smaller and not self-supporting, a set of support legs was designed for the field calibrator, and a special base plate was made; the radiometers were supported from the base plate. The design was made kinematic by attaching a D-shaped mounting collar 3.81 cm from the front of the radiometer. The flat section of the collar was aligned with the bluest channel in the set of channels for each radiometer, which was usually the one at 411 nm. The receiving aperture in the field calibrator base plate contained a step in the diameter and a set of locking cams on the bottom of the base plate. Custom spacers were used to fix the distance between the field radiometers and lamp E007 at 50 cm. This general design was used in the SQM (Sect. 6, and Johnson et al. 1998b). The D-shaped collars were also used as a mechanical reference in the in-water and laboratory calibration activities.

The UV intercomparison control equipment for the field calibrator did not require modification for SIRREX-5. The lamp current was held constant using a calibrated shunt resistor in series with the lamp. A Visual Basic computer program (Microsoft Corp.) operating on a Toshiba laptop PC in the Windows environment, monitored the lamp current as measured with the shunt resistor using the General Purpose Interface Bus (GPIB) and a Hewlett Packard

Fig. 16. Photograph taken during SIRREX-5 of the absolute irradiance field source (Lab V). The experiment was located at Little Seneca Lake, on the southwest side of the parking lot at the WSSC pumping station building.

(HP) digital multimeter (DMM) model HP 3457. The computer program recorded the lamp current and voltage at regular intervals. The general procedure is described fully in Walker and Thompson (1994).

The field irradiance calibrator contains a mechanical arm located midway between the lamp mount and the base plate. Circular discs are attached to the end of the arm to block the direct irradiation from the lamp onto the irradiance collector. The motor-controlled arm has two positions, stowed and centered; these are selected with a switch. In the centered position, the diffuse, or ambient, signal was measured; and in the stowed position the response to the standard lamp was measured. The size of the disc was determined during the initial alignment procedures on 23 July by visual inspection of the shadow cast on the radiometers. The goal was to shadow all of the diffusers (there is one for each channel) without eliminating all sources of scattered radiation. Possible sources of scattered light include the edges of the apertures in the field calibrator located between the lamp and the base plate, and the mechanical lip at the outer edge of the radiometers. The edge of the black disc, however, may also be a source of scattered radiation, which makes this a difficult measurement. The use of this type of on-axis baffle to record background is recommended because this corresponds to the method used for the calibration of the FEL lamp at NIST.

4.2 Daily Procedures

The unit designated UAI in Table 2 was used for most of the measurements in Lab V. This downwelling, in-air, irradiance sensor contained an integrated A/D unit, as do the majority of the Satlantic $E_s(0^+, \lambda)$ sensors. The power supply and data logger, along with the data acquisition computer, were located in the Washington Suburban Sanitary Commission (WSSC) building on the Little Seneca Lake Dam. Custom data acquisition software, developed in LabVIEW (National Instruments) by the SeaWiFS Project, was used with a Macintosh PowerBook portable computer. The field calibrator was located between the parking lot and the spillway on the southwest side of the site. The daily temperature was probably about 30°C, but no records were kept in Lab V. The SIRREX-5 participants in Lab V assisted in the operation of the UV

irradiance field source, operated the OCI-200 data acquisition program, and were instructed in laboratory practices of field irradiance calibrations.

Before the first measurement was made, the lamp base was aligned in the field calibrator using a lamp alignment jig (mounted in the lamp holder) and a radiometer alignment fixture. This fixture consisted of an aluminum rod with a threaded hole in one end and scribe lines on the other end. An aluminum cup-shaped fixture, designed to fit over the Satlantic radiometers, was attached to the end of the rod. The dimensions of the cup were such that when the scribe lines were flush and aligned to the cross hairs on the lamp alignment jig, the radiometer would be the correct distance and orientation with respect to the lamp. The alignment procedure was verified using a wooden rod that was 50 cm in length. The fixtures designed for the Satlantic radiometers could have been produced for units from the other manufacturers, but because the scope of the measurements at SIRREX-5 was limited, this was not done.

Table 17. Irradiance $[E(\lambda)]$ values at 50 cm from the calibration of lamp E007, including the combined relative standard uncertainties.

λ [nm]	$E(\lambda)$ [μW cm^{-2} nm^{-1}]	σ' [%]
250	0.0193	1.1
260	0.0333	1.4
270	0.0547	1.1
280	0.0866	0.8
290	0.1303	0.81
300	0.1892	0.93
310	0.2685	0.76
320	0.3692	0.72
330	0.4898	0.72
340	0.6421	0.69
350	0.8254	0.64
360	1.039	0.66
370	1.290	0.70
380	1.573	0.67
390	1.882	0.69
400	2.243	0.77
450	4.491	0.67
500	7.441	0.65
555	11.44	0.67
600	13.95	0.73
654.6	17.09	0.72
700	19.29	0.70
800	22.40	0.58
900	23.41	0.66

Each day began with initializing the control systems for the field calibrator and the irradiance sensors. The location of the D-shaped collar was checked, and the radiometer was mounted in the field calibrator with the bluest channel directly under the base of the lamp. As the lamp was warming up, the mechanical shutter was put in the centered position. In some cases, the lens cap was left on initially (or repositioned at the end of the measurement sequence) and the background was recorded, generally for 2 min. Then the lens cap was removed, and as the lamp was continuing to warm up, the ambient signal was recorded, also for 2 min, and the shutter was moved to the stowed position. Then, after about 15 min had elapsed, the signal was recorded. In some cases, these data were stored in the same data file, and in other cases, different files were used.

On 23–26 July, sensor UAI was measured with the field calibrator. During the session on 26 July, UAI was rotated in 120° increments to study the alignment sensitivity. Sensor SAE was measured on 25 July, and GAI and PWI were measured on 26 July. On 27 July, four sensors were measured: JWI, UWE, UWI, and GWE. Each of these eight sensors had seven measurement channels, with common wavelengths at 412, 443, 490, 509, and 555 nm. The other two measurement channels were between 590–779 nm. For all of the measurements with the field calibrator, the current and voltage of E007 were stable, and were equal to the values during the NIST calibration: 8.2 A and 109.3 V. The lamp calibration data and relative standard uncertainties are given in Table 17 as a function of wavelength. FEL lamp E007, was measured for irradiance in a horizontal position at 8.2 A and 109.3 V direct current (dc) using a special setup which transferred the calibrated irradiance from FASCAL (Early et al. 1998a).

4.3 Results

4.3.1 Analysis

The raw data from the Satlantic sensors were reduced by using a custom written FORTRAN program, which used the International Mathematical and Statistical Libraries (IMSL)† routine, `UVSTA`, for obtaining the means and the standard deviations. A graphical routine was also incorporated into the FORTRAN program for viewing the raw data as a function of time, and the program could be run in batch mode for rapid processing of all the data files. In reducing the data, no effort was made at spike removal because the contribution to the total uncertainty by the random noise was deemed to be much smaller than the uncertainty due to other factors.

The voltages on the silicon photodiode detectors on the Satlantic irradiance sensors were digitized to counts by either an external or a built-in A/D converter at a sampling rate of 6 Hz. The mean counts, $\overline{X}(\lambda)$, were found by averaging over time:

$$\overline{X}(\lambda) = \frac{1}{n}\sum_{j=1}^{n} X_j(\lambda, t), \quad (9)$$

† IMSL is a registered trademark of Visual Numerics, Inc.

where $X_j(\lambda, t)$ is the sensor output, λ is the detection wavelength of the sensor channel, n is the total number of individual samples, and t is the time at the particular data sampling. The standard deviation for the data set and the uncertainty in the mean were determined from the Taylor and Kuyatt (1994) procedures. The total signal, $\overline{S}_{\rm T}$, is the time-averaged signal found using (9), and the net signal, $\overline{S}_{\rm N}$, is given by

$$\overline{S}_{\rm N} \;=\; \overline{S}_{\rm T} \;-\; \overline{B}, \tag{10}$$

where $\overline{B}$ is the average background signal. The background or the offset signal can be found by either covering the irradiance sensor with a lens cap and thus, blocking all sources of light, or by shuttering the direct line-of-sight from the source to try to account for scattered light. The extra light is due to the scattered radiation, as discussed in the beginning of this section. The average capped background signal is denote by $\overline{B}_{\rm C}$, and the average shuttered background is denoted by $\overline{B}_{\rm S}$. Finally, the average calibration coefficient, D, is obtained from the net signal, $\overline{S}_{\rm N}$, and the known irradiance, $E(\lambda)$, at a particular wavelength, λ, using

$$\begin{aligned} D \;&=\; \frac{\overline{S}_{\rm N}}{E(\lambda)} \\ &=\; \frac{1}{F} \end{aligned}. \tag{11}$$

In the calibration data supplied with the radiometers, the inverse of the calibration coefficient or the calibration factor, F, is given.

To determine the calibration coefficients for the irradiance sensors, the irradiance values for E007, were fit using a fifth order polynomial multiplied by a modified planckian function:

$$\begin{aligned} E(\lambda) \;=\; &(a_0 \;+\; a_1\lambda \;+\; a_2\lambda^2 \;+\; a_3\lambda^3 \\ &+\; a_4\lambda^4 \;+\; a_5\lambda^5)\exp(a_6/\lambda)/\lambda^5 \end{aligned} \tag{12}$$

(Saunders and Shumaker 1977). The fit was performed using a nonlinear, least-squares fit routine in a commercial graphics package (Microcal Origin). The fitting parameters and the standard uncertainties in the best fit parameters are shown in Table 18. Although the uncertainties in the fitting parameters are sometimes larger than the parameters themselves, the fitting routine converged to the same values for multiple fitting sessions for the same data. The large uncertainties are probably due to having more parameters than is needed for an optimal fit. The differences between the irradiances derived from the functional fit and the calibrated irradiance values differed by less than ±0.3% in the wavelength range from 400–900 nm. The interpolation was done at the sensor wavelengths obtained from the owners of the radiometers, and the wavelength values were usually the same as the values supplied by the manufacturer at the time of purchase or recalibration.

Table 18. The fitting parameters used in performing the nonlinear least-squares fit of (12). With the wavelength in nanometers, the irradiance calculated from (12) is in units of μW cm^{-2} nm^{-1}.

Parameter	*Value*	σ
a_0	-8.507×10^{17}	2.588×10^{19}
a_1	2.273×10^{16}	5.967×10^{16}
a_2	-6.700×10^{13}	4.920×10^{13}
a_3	9.977×10^{10}	4.455×10^{10}
a_4	-7.446×10^{7}	7.166×10^{7}
a_5	2.209×10^{4}	2.941×10^{4}
a_6	-4595	1726

On 25 July, two methods for subtracting the background were examined. Figure 17 plots the ratios of the net shuttered signal divided by the net capped signal, or $\overline{S}^S_N$:$\overline{S}^C_N$, where $\overline{S}^S_N = \overline{S}_T - \overline{B}_S$ and $\overline{S}^C_N = \overline{S}_T - \overline{B}_C$, for two different sensors: UAI and SAE.

For the UAI instrument, the different methods for background subtraction were examined over three consecutive days 24–26 July, and on 25 July also under different rotational mounting conditions (Fig. 17). Excluding the outlier at 770 nm for sensor SAE, $\overline{S}^S_N$ is about 1.2% smaller than $\overline{S}^C_N$. The percentage standard deviations of the net capped signal of 24 July for the UAI instrument are given in Table 19. The decrease in the standard deviation with increasing wavelength is due to the increased irradiance of the lamp at longer wavelengths, which leads to larger net signals. The values in Table 19 are also representative of the percentage standard deviations for the measurements done at later times and also for the SAE instrument.

Table 19. The relative standard deviation, σ' for $\overline{S}^C_N$, as measured by the UAI sensor on 24 July.

λ [nm]	σ' [%]
411.2	0.37
442.8	0.26
489.6	0.16
509.5	0.13
555.3	0.09
589.0	0.08
665.5	0.06

On 24–26 July, the UAI instrument was mounted with the shortest wavelength sensor oriented with the base of the lamp, and the SAE instrument was mounted in the same way. The wavelength value on the legend denotes that the channel corresponding to that wavelength of detection was mounted directly underneath the base of the FEL lamp. Figure 17 shows that with the exception of a single outlier at the 775 nm channel for the SAE sensor, the net signal found by subtracting the shuttered background is, on average, 1.2% smaller than the net signal

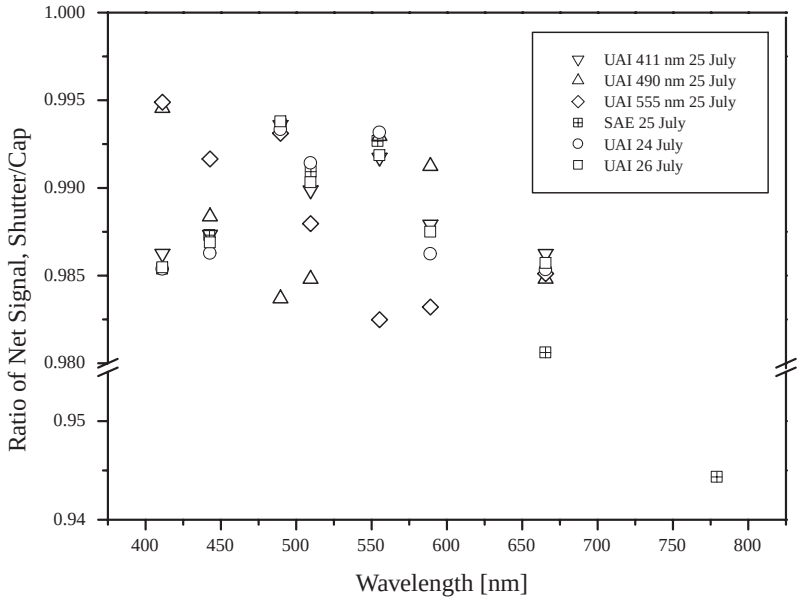

Fig. 17. The ratio $\overline{S}_N^S$:$\overline{S}_N^C$ for sensors UAI and SAE. For sensor UAI, the ratios from 24–26 July are shown, along with the ratios measured on 25 July as a function of rotation. A single ratio from 25 July is shown for sensor SAE.

found by subtracting the capped background. There is, in addition, a dependence of the amount of scattered light on the angular orientation. If the channel is directly beneath the base of the lamp, a drop of nearly 1% occurs in the net counts due to the additional scattered light. The experiment points out that the

1) Amount of scattered light is dependent on the rotational orientation of the irradiance sensor; and
2) Unless the capped background signals and the shuttered background signals are equal, the net signal found by subtracting the capped signal overestimates the true signal.

To determine the calibration coefficients in SIRREX-5, the shuttered signals were used for background subtraction.

4.3.2 Repeatability

For monitoring the repeatability of a channel centered at wavelength λ, whether temporal or positional, the percent deviation from the mean,

$$\breve{X}_k(\lambda) \;=\; 100\left[\frac{\overline{X}_k(\lambda)}{\hat{X}(\lambda)} \;-\; 1\right], \tag{13}$$

is used with

$$\hat{X}(\lambda) \;=\; \frac{1}{m}\sum_{k=1}^{m}\overline{X}_k(\lambda), \tag{14}$$

where m is the number of measurement sessions, and $\hat{X}(\lambda)$ is the mean of the results for each measurement session.

A single irradiance sensor, UAI, was measured for four consecutive days to determine the temporal stability of the sensor and the reproducibility of the overall technique. The sensor was taken off the mount after the measurement and remounted each day. A plot of the variability of the net capped signal, $\hat{S}_N^C$, referenced to the mean, over four days is shown in Fig. 18. In placing the sensor on the field calibrator, care was taken on each day to reproduce the same orientation of the channels to the lamp. Figure 18 shows that the sensor was stable with an uncertainty less than ±0.5% over the four days. The percentage standard deviation of each of the channel counts over the four days is shown in Table 20.

Table 20. Values for σ' for the UAI sensor of the percentage difference from the mean for $\overline{S}_N^C$ over four consecutive days.

λ [nm]	σ' [%]
411.2	0.13
442.8	0.15
489.6	0.27
509.5	0.50
555.3	0.24
589.0	0.15
665.5	0.11

4.3.3 Alignment Sensitivity

The sensitivity to angular alignment was tested in the field calibrator by orienting a particular channel of the irradiance sensor to directly view the base of the FEL lamp.

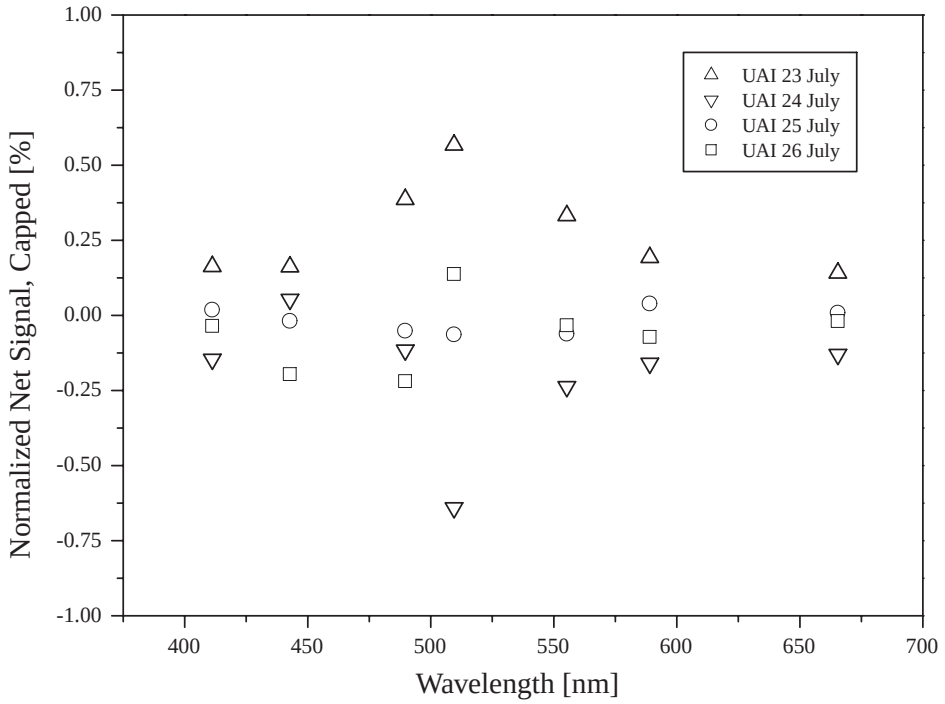

Fig. 18. The percent difference of the individual net capped signal, from the average over four consecutive days. The measurements were made with sensor UAI.

Using (14), the percentage difference of the net shuttered signal measured at three different orientations of the sensor from the mean of the three measurements, $\hat{S}_N^S$, is plotted in Fig. 19. The legend "411 nm" corresponds to the orientation in which the sensor with a filter centered at 411 nm is aligned with the base of the lamp. The irradiance unit was rotated such that in turn, the 411 nm channel, the 490 nm channel, and then the 555 nm channel was facing the base of the FEL lamp. In all three configurations, the longest wavelength (665.5 nm) channel remained at the center of rotation. When the channel at 411 nm is aligned with the base of the lamp, an approximate 1.5% decrease in the net signal is observed, and when the 490 nm channel is similarly aligned, almost a 2% decrease is observed. The minimum in the ratio moves to 555 nm when that channel is aligned with the base of the lamp.

Figure 19 shows that up to a 2% decrease in the measured irradiance occurs when a particular channel is aligned with the base of the lamp. Table 21 shows that correspondingly, the standard deviation for the measurements of the sensor in the 665.5 nm channel, which is in the central position, has the smallest percentage standard deviation of all the channels. The decrease most likely occurs because the FEL lamp is not a perfect point source of light, and the irradiance is not uniform over the entire face of the OCI sensor heads.

Table 21. The relative standard deviation of the percentage difference from the mean of the shuttered net signal for three different orientations of the sensor UAI.

λ [nm]	σ' [%]
411.2	0.68
442.8	0.43
489.6	1.02
509.5	0.69
555.3	0.94
589.0	0.55
665.5	0.30

The decrease in the net signal as a function of the angular position is probably caused by two things. First, as seen in Fig. 17 for the UAI sensor, the amount of scattered light depends on the angular position, and increases when the channel is underneath the base of the lamp. Figure 20 shows the data of 25 July from Fig. 17 plotted as percent deviation of the individual ratios from the average ratio found using (14). The plot shows the angular dependence of the scattered light. The standard deviation of the three configurations for each channel is given in Table 22, and shows that the smallest standard deviation is found for the channel in the middle of the configuration. Second, the variations in the lamp irradiance as a function of the viewing angle also leads to changes in the total signal. From Fig. 20, it is estimated that about two thirds

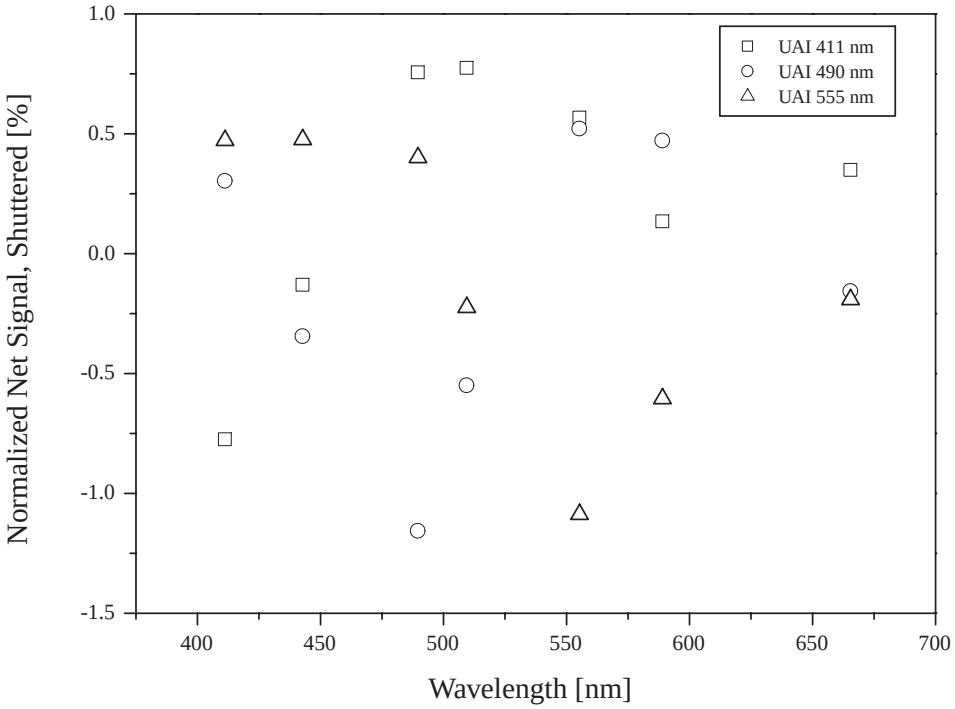

Fig. 19. The percent difference of the individual net shuttered signal from the average for three different angular positions of the sensor UAI. The wavelength value for the symbol indicates the particular sensor channel that was directly aligned with the base of the lamp; the result for this channel is consistently lower than the other channels, independent of the overall angular alignment.

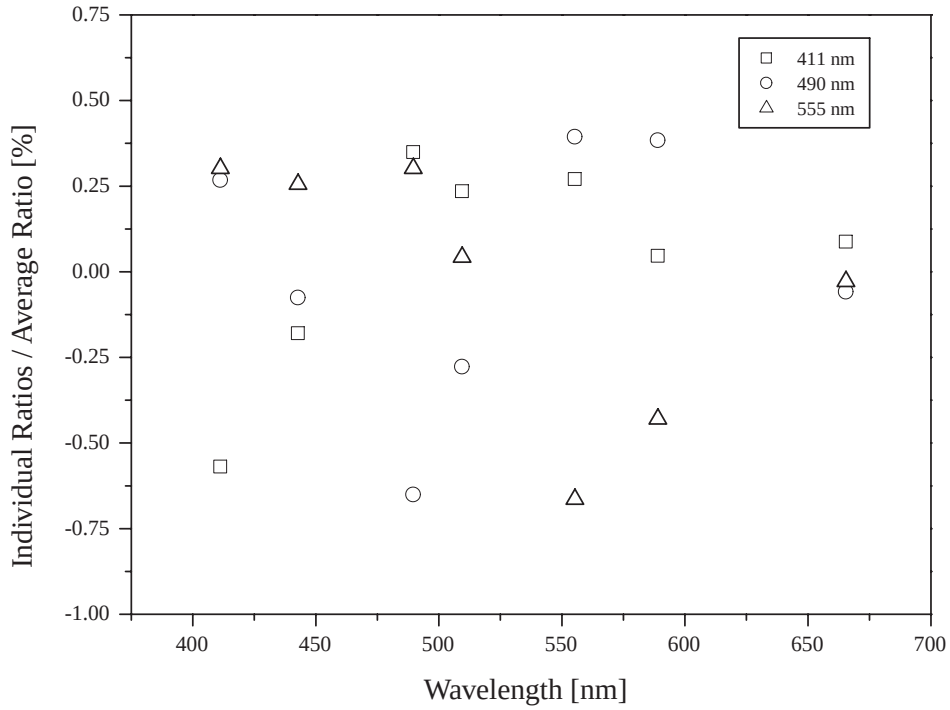

Fig. 20. The percent difference of the individual ratios from the average ratio taken from the UAI 25 July data of Fig. 17.

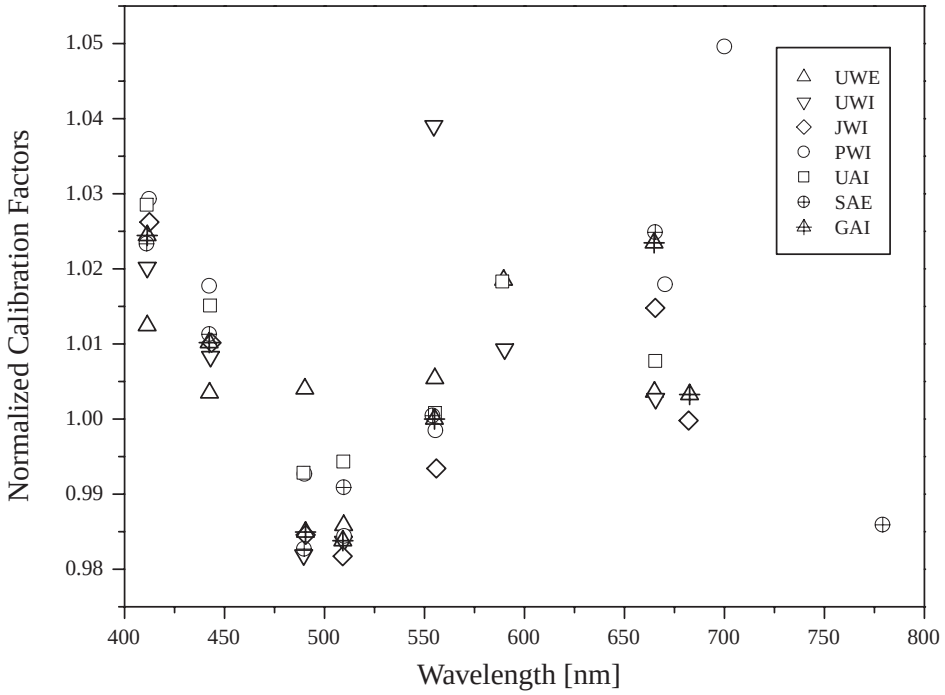

Fig. 21. The calibration factors found in using the field calibrator, F_{FS}, normalized by the calibration factors determined at NIST, F_{NL}, for six different irradiance sensors. The value for the UAI sensor is an average of three readings taken on consecutive days. The other irradiance sensors were measured only once.

of the drop in net signal in Fig. 19 is due to the increase in the background signal, with the additional one third of the drop coming from a decrease in the total signal.

Table 22. The standard deviation of the percentage difference of the individual ratios from the mean for sensor UAI.

λ [nm]	σ' [%]
411.2	0.49
442.8	0.23
489.6	0.56
509.5	0.26
555.3	0.58
589.0	0.41
665.5	0.08

4.3.4 Calibration

Figure 21 shows the ratio of the calibration factors (F) determined using the field irradiance source, F_{FS}, divided by those determined in the NIST laboratory, F_{NL}, for seven different irradiance sensors. All the field calibrations were done only once, with the exception of the UAI instrument, which was measured on three different days and the average is plotted. A systematic decrease from 400–500 nm is seen. Part of the decrease is due to the angular dependence of the net shuttered signal. The net signal when the channel is directly beneath the base of the lamp is almost 2% lower than the channels away from the base, as seen in Fig. 20. Because all the irradiance calibrations on the field calibrator were done with the shortest wavelength channel beneath the base of the lamp, the shortest wavelength channel will have a smaller net signal and, thus, a larger calibration factor than the other channels. With the exception of a few outliers, this effect is clearly seen in Fig. 21.

The effect on the calibration factor due to the angular positions of the channels can be compensated for by multiplying the ratio, F_{FS}:F_{NL}, by the ratio of the net signal taken with the 411 nm channel beneath the base of the lamp over the average signal from Fig. 20. The ratios of the calibration factors for the UAI sensor, uncorrected and corrected for the angular effect, are plotted in Fig. 22. The effect of multiplying by the ratio of the net signal over the average net signal is, in essence, that the net signal averaged over the three different angular positions is used in calculating the field calibration factor. Figure 22 shows that the peak-to-valley variation is reduced, but not eliminated, with a reduction in the percentage standard deviation over all channels from 1.3% before the multiplication of the ratio, to 0.8% percentage standard deviation with the correction applied. The remaining dip in the ratios of calibration factors could be also due to the sensitivity of

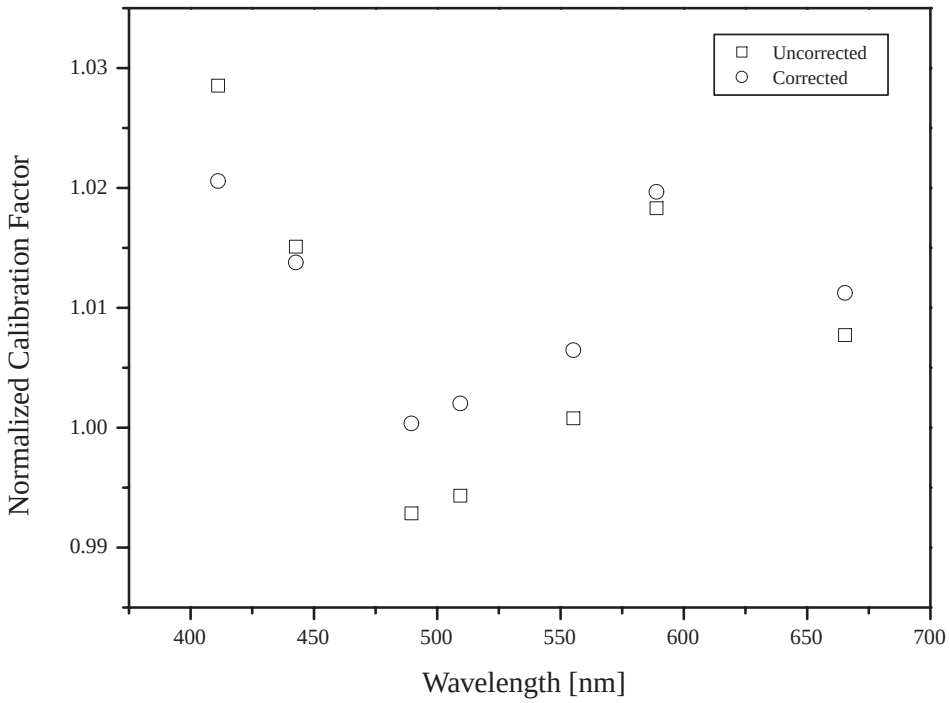

Fig. 22. The field calibration factor divided by the NIST calibration factor for the UAI sensor before (uncorrected) and after (corrected) multiplication by the ratio of the net signal at the 411 nm orientation divided by the average signal of three different orientations.

Table 23. Relative standard uncertainties, in percent, for the irradiance calibration of the UAI instrument using the UV field calibrator. These uncertainties are also applicable to the other irradiance sensors calibrated using this device.

	λ [nm]						
Component of Uncertainty	411.2	442.8	489.6	509.5	555.3	589.0	665.5
Lamp Irradiance	0.72	0.69	0.66	0.66	0.68	0.71	0.71
Interpolation	0.30	0.30	0.30	0.30	0.30	0.30	0.30
Lamp Current	0.08	0.07	0.06	0.06	0.06	0.05	0.05
Daily Reproducibility	0.13	0.15	0.27	0.50	0.24	0.15	0.11
Angular Variations	0.49	0.23	0.56	0.26	0.58	0.41	0.08
Alignment	0.42	0.42	0.42	0.42	0.42	0.42	0.42
Wavelength	1.51	1.22	0.91	0.80	0.60	0.48	0.29
Signal	0.37	0.26	0.16	0.13	0.09	0.08	0.06
RSS† Total	1.87	1.54	1.40	1.30	1.22	1.09	0.94

† Root-Sum Square

the laboratory calibration factor to angular position, but the dependence on the angle was not tested in the laboratory.

Finally, the total uncertainty of the field irradiance calibration coefficient can be estimated. As a representative sensor, the instrument UAI was tested much more extensively than the other sensors and the results from the sensor are used as generic values. Other instruments tested on the field calibrator are expected to have similar total uncertainties.

Table 23 gives each component of the total uncertainty for the UAI sensor for an absolute irradiance calibration in the field. The uncertainty in the irradiance in the FEL lamp operated in the horizontal position (Table 17) is based on the analysis in Early et al. (1998a). The estimation of the lamp irradiance at the measurement wavelengths of

the UAI sensor is termed the "interpolation component of uncertainty" in Table 23. The component of uncertainty related to the lamp current is based on a systematic uncertainty of 0.81 mA (Early et al. 1998a) and the effect of this uncertainty on the spectral irradiance (Appendix D in Early et al. 1998c). The effect of the random uncertainty in the current is incorporated in the daily reproducibility values.

The angular variations component of uncertainty is estimated using the standard deviation of individual measurements (Table 22). For comparison, the models described in Appendix D of Early et al. (1998c) were used to estimate the uncertainty associated with a receiver aperture greater than that used in FASCAL and the non-ideal goniometric distribution of the lamp irradiance; the result is 0.4%, in reasonable agreement with the observations.

The alignment component of uncertainty includes the effects of the uncertainty in the distance, perpendicularity between the lamp and the receiving aperture, and coalignment of these elements on the proper optical axis. Again, the treatment presented in Appendix D of Early et al. (1998c) was followed. The estimated uncertainty in the distance is 0.1 cm, the degree of perpendicularity is 0.5°, the offset uncertainty in the lamp is 0.1 cm, and the offset uncertainty in the central channel of the UAI sensor is 0.2 cm.

The uncertainty in the spectral irradiance calibration, caused by the uncertainty in the wavelength of the UAI sensor, is proportional to the product of the UAI wavelength uncertainty and $\mathrm{d}E/\mathrm{d}\lambda$ (Early et al. 1998c, Appendix D). The uncertainty in the sensor wavelengths is estimated to be 1 nm, resulting in up to a 1.5% uncertainty at 411 nm. Finally, the measurement uncertainty is repeated from Table 19. The combined relative standard uncertainty is given in the last row of Table 23; it is the RSS of the individual components of uncertainty.

The results of the field calibration are given in Table 24 in terms of the calibration factors for Lab V, F_{FS}. Note that because GWE was not measured in the NIST laboratory, no comparison is made in Fig. 21. The values from the field calibrator in Lab V, however, can be compared to the manufacturer's data. Satlantic supplied the calibration data for GWE in terms of the analog voltage, but at SIRREX-5, the digital counts from an A/D unit were recorded. The conversion factors for all of the A/D units were determined just before SIRREX-5 using a precision voltage source and were found to be linear over the range of interest (Sect. 6), and these values were used to convert the Satlantic calibration factors into the standard units. The determined conversion from voltage to counts used is $0.153\,\mathrm{mV\,count^{-1}}$.

4.4 Discussion and Recommendations

The shutter method of determining the offset is the same method used in the NIST calibrations and the plaque laboratory (Lab VI), but it is not the typical method used at Satlantic. All of the field calibrator data were reduced using the mechanical shutter data. Based on Fig. 17, a discrepancy of about 1.2% is expected between the Satlantic and NIST methods of calibration (Sect. 7).

The calibrations performed at the FASCAL facility are done over a 23 mm diameter area at 50 cm perpendicular distance away from the front of the mounting post of the lamp. The angular distribution of the irradiance is measured only under special request. The angular distribution of the lamp irradiance varies from lamp to lamp, but the latitudinal variations are more severe than in the longitudinal variations (C. Gibson, pers. comm.). In order to reduce the variations in the calibration factors, the optimal solution is to measure each of the sensors in turn, each aligned to the lamp. Because such alignment of the channels is difficult, one solution is to measure the signal at the six different orientations of the sensor and use the averaged counts over the six positions in reporting the calibration factor.

5. PLAQUE LAB

The motivation of the plaque laboratory was to continue the investigation initiated in the earlier SIRREXs on the procedure of using a standard irradiance lamp and a Spectralon plaque to create a large area source of spectral radiance. Several issues, including the uniformity of the radiance, effects of scattered light, and values of the BRDF for the plaque were discussed in SIRREX-4 (Appendix B in Johnson et al. 1996). The goal at SIRREX-5 was to establish an experimental system that was less likely to exhibit common sources of bias as compared to the setup that was used during SIRREX-4. Lab VI was also motivated by the requirement to perform NIST radiance calibrations before or after SIRREX-5 on the participating radiometers, and to provide a method to investigate the stability of the radiance calibration factors during SIRREX-5. Unfortunately, the pre-SIRREX-5 radiance calibrations were invalid because of problems with the data acquisition system (Sect. 7.2). For all measurements in the plaque laboratory, the SXR was used as a monitor of the spectral radiance.

5.1 Overview

The general design of Lab VI was similar to that implemented in SIRREX-4 (Johnson et al. 1996), but several improvements were made. The plaque laboratory for SIRREX-5 consisted of a new 60.96 cm, square, Spectralon plaque (S/N 99240) mounted vertically in a frame that was mounted on a motorized rotary stage. The vertical centerline at the face of the plaque was aligned with the axis of rotation. A rail made from aluminum channel was attached to the rotary stage so that the angle between the axis of the rail and the "normal" to the plaque was 45°, and the axis of the rail intersected the plaque at the axis

Table 24. Calibration factors for eight irradiance sensors, as determined in Lab V, as a function of nominal wavelength. The units of $F_{\rm FS}$ are $\mathrm{nW\,cm^{-2}\,nm^{-1}\,count^{-1}}$. The immersion coefficients are not included in these calibration factors, so these are in-air values.

	$F_{\rm FS}$			
λ [nm]	GAI	GWE	PWI	UAI
412	8.382×10^{-3}		4.552×10^{-3}	1.035×10^{-2}
443	9.925×10^{-3}	6.513×10^{-3}	5.039×10^{-3}	1.110×10^{-2}
490	9.822×10^{-3}	6.355×10^{-3}	5.003×10^{-3}	1.094×10^{-2}
510	9.105×10^{-3}	6.889×10^{-3}	4.886×10^{-3}	1.049×10^{-2}
555	1.010×10^{-2}	7.064×10^{-3}	4.413×10^{-3}	1.035×10^{-2}
590				1.030×10^{-2}
665	1.003×10^{-2}	6.565×10^{-3}		1.046×10^{-2}
670			4.542×10^{-3}	
682	9.210×10^{-3}	7.185×10^{-3}		
700			5.896×10^{-3}	
779				

Table 24. (cont.) Calibration factors for eight irradiance sensors, as determined in Lab V, as a function of nominal wavelength. The units of $F_{\rm FS}$ are $\mathrm{nW\,cm^{-2}\,nm^{-1}\,count^{-1}}$. The immersion coefficients are not included in these calibration factors, so these are in-air values.

	$F_{\rm FS}$			
λ [nm]	UWI	UWE	JWI	SAE
412	1.009×10^{-3}	6.300×10^{-3}	6.138×10^{-3}	9.989×10^{-3}
443	1.053×10^{-3}	6.522×10^{-3}	6.369×10^{-3}	9.279×10^{-3}
490	1.065×10^{-3}	6.056×10^{-3}	6.247×10^{-3}	9.554×10^{-3}
510	1.150×10^{-3}	6.940×10^{-3}	6.590×10^{-3}	9.937×10^{-3}
555	1.216×10^{-3}	6.594×10^{-3}	6.779×10^{-3}	9.032×10^{-3}
590	1.121×10^{-3}	6.934×10^{-3}		
665	1.125×10^{-3}	6.939×10^{-3}	6.901×10^{-3}	9.959×10^{-3}
670				
682			6.622×10^{-3}	
700				
779				8.908×10^{-3}

of rotation. Sets of holes were drilled in the top of the rail at selected distances, and a double V-block assembly was mounted to the rail using matching holes in the base plate of the double V-block, which held the radiometer to be calibrated. A pair of motorized linear translation stages, stacked together, were aligned perpendicular to the plaque. An FEL lamp mount assembly was attached to the top linear translation stage. The SXR was mounted on a tripod and viewed the center of the plaque, also at an angle of 45°, but from the opposite side of the lamp assembly as the rail for the radiometers. The SXR was not moved during SIRREX-5. All three motorized stages (from Aerotech), were under computer control in the absolute mode.

Black cloth enclosed the entire area, which comprised the area around a 1.2×1.8 m laser table. For the walls, ceiling, and curtains on three sides, black and opaque photographer's dark-room cloth was used. A partition between the lamp and the plaque was also constructed. The partition had a central square hole that resulted in direct illumination of the plaque, with about 10 cm around the edge of the plaque also illuminated (this flux fell on the black curtain which was about 15 cm behind the plaque). The partition did not reach to the ceiling, but did block the direct view of the illuminated portion of the ceiling from any point on the plaque. The reflectance of the photography cloth appeared adequate for photometry, but the reflection in the near infrared is not known. The table was covered with heavy black felt, and a piece of felt was draped over the central hole for measurement of the diffuse (or ambient) background. The equipment stand with the Aerotech stage control system was inside the enclosed area, and it was also covered with black cloth. The equipment cart for the SXR and the radiometers under test were located outside the enclosed area.

The system was aligned in several steps. A Class III HeNe laser was placed about 3 m from the plaque mount using a four-axis mount attached to a large tripod. With

the Spectralon plaque removed, a 60.96 cm, square, aluminum plate was placed in the plaque frame. Scribe marks indicated the center of the aluminum plate, and a glass microscope slide was placed over the central area. The laser was adjusted to lie in the horizontal plane at the height corresponding to the center of the aluminum plate; the angle of incidence was verified to be 0° using the glass slide. The stage was rotated by up to ±45° to ensure that the axis of rotation was at the front face. Then, the FEL lamp alignment jig was placed in the lamp mount, and the linear translation stages and the lamp mount were adjusted until the laser was centered with the lamp and perpendicular to the glass face in the lamp jig for the entire range of linear motion. Finally, the SXR and one of the test radiometers were aligned to the correct angles by rotating the plaque frame by ±22.5°, and using the reflection of the laser from the glass slide. The distance between the lamp and the front of the aluminum plate was measured and the absolute positions of the stages as given by the computer control, were noted for future reference.

The double V-block held each of the Satlantic radiometers (listed in Table 2) at the correct height, and the sets of holes in the rail were denoted by the half-angle field of view from that position: 18° and 10°, as determined by the vertical dimension of the plaque. The distance from the radiometer to the plaque was set using the D-shaped collar as a mechanical reference; it was flush with one face of one of the V-blocks.

5.2 Daily Procedures

The general procedure in Lab VI was to mount the OCR-200 sensor at the 18° (half-angle) position on the rail, set the lamp-to-plaque distance to a known value (usually about 1.2 m), and then turn on the lamp. As the lamp was warming up, the central square hole in the cloth partition was blocked, or baffled, using a section of black felt, and these baffled values were recorded as a measure of the background counts. After the lamp was warmed up for at least 15 min, the felt was removed and the total signal was recorded, with the plaque fully illuminated. Data were also obtained for both of these configurations with the SXR. The participants in Lab VI were responsible for operating the SXR data acquisition system, the OCR-200 data acquisition system, and preliminary reduction of the data.

On 23 July, no useful data were obtained because of the problem with the data acquisition system (Sect. 7). On 24 July, the GWR, PWR, UWR, and JWR were measured using F332 at a distance of 122.6 cm. Using the SXR, the lamp-to-plaque distance was varied to investigate the variation in radiance (expected to be inversely proportional to distance, i.e., r^{-2}). Data were obtained with the lamp at distances of 1.5, 1.72, and 1.97 m from the plaque. On 25 July, the SWQ, UWR, and PWR were measured and additional r^{-2} measurements were performed with the SXR. On 26 July, UWR and JWR were measured; JWR was rotated about its optical axis to test for field-of-view effects.

5.3 Results

5.3.1 Analysis

In the radiance sensors, the output signals from the photodiodes were converted to counts by an internal A/D converter. In order to find the averages and standard deviations, the output counts were reduced using a custom written FORTRAN program as described in Sect. 4.3. The raw counts were averaged using (9) from Sect. 4.3, and again, no effort was made to filter spikes in the data because other contributions to the uncertainty were deemed greater. The net average signal, $\overline{S}_{\rm N} = \overline{S}_{\rm T} - \overline{B}$, was obtained from the total signal, $\overline{S}_{\rm T}$, by subtracting the average background signal, $\overline{B}$. The background signal was measured by blocking the lamp output by an on-axis shutter, which cast a shadow over the entire plaque. The radiance calibration coefficients were obtained from the net signal using

$$\begin{aligned} D &= \frac{\overline{S}_{\rm N}}{L_{\rm C}(\lambda)}\,, \\ &= \frac{1}{F} \end{aligned} \qquad (15)$$

where D is the calibration coefficient, and $L_{\rm C}(\lambda)$ is the calculated radiance.

The radiance values were calculated using the irradiance from a calibrated FEL lamp (F332 in a vertical position at 7.9 A and 111.8 V dc) normally incident on the Spectralon plaque. The radiance, $L_{\rm C}(\lambda)$, is calculated from the known incident irradiance by using (Johnson et al. 1996, Appendix B)

$$L_{\rm C}(\lambda) = \frac{R(0°/45°,\lambda)}{\pi}\left(\frac{50\ {\rm cm}}{r}\right)^2 E(\lambda, 50\ {\rm cm}), \qquad (16)$$

where λ is the center wavelength of an individual channel, r is the distance of the plaque from the base of the FEL lamp in centimeters, $E(\lambda, 50\ {\rm cm})$ is the irradiance measured at 50 cm, and is the directional/directional reflectance factor. The reflectance factor was not measured by NIST for the large plaque because it would not fit into the experimental apparatus without substantial modifications. Following the rationale presented in the SIRREX-4 document (Johnson et al. 1996, Table B1), the reflectance factor was estimated using the 8°/hemispherical (8°/h) data provided by Labsphere at the time of purchase. The relationship between the 0°/45° reflectance factor and the 8°/h reflectance factor is taken to be $R(0°/45°,\lambda) = 1.02\ R(8°/{\rm h},\lambda)$. Because Spectralon plaques are not lambertian, a different proportionality factor would be required for other geometries.

The calibrated irradiance values from FASCAL, (Table 25) were fit by a modified planckian function given by

(12), and the fitted function was used to interpolate the calibrated irradiance values to the wavelength of interest, λ. The parameters used in the fit and the associated uncertainties are listed in Table 26. The interpolated irradiances were used in (16) to calculate the radiance.

Table 25. The calibrated irradiance values from FASCAL for lamp F332 in the vertical position at 7.9 A and 111.8 V dc.

λ [nm]	$E(\lambda)$ [μW cm^{-2} nm^{-1}]	σ' [%]
250	0.0175	0.72
260	0.0313	0.70
270	0.0514	0.67
280	0.0807	0.64
290	0.1214	0.61
300	0.1772	0.58
310	0.2499	0.54
320	0.3424	0.51
330	0.4574	0.49
340	0.5998	0.47
350	0.7702	0.44
360	0.9685	0.42
370	1.202	0.41
380	1.464	0.40
390	1.755	0.39
400	2.087	0.38
450	4.210	0.34
500	6.961	0.32
555	10.33	0.31
600	13.04	0.32
654.6	16.00	0.34
700	18.07	0.36
800	21.06	0.40
900	22.09	0.45

Table 26. The fitting parameters used to fit (12) to the calibrated irradiances from FASCAL for lamp F332 for use in (16). The units are the same as in Table 18.

Parameter	*Value*	σ
a_0	-6.447×10^{17}	3.586×10^{19}
a_1	2.273×10^{16}	9.678×10^{16}
a_2	-6.857×10^{13}	1.126×10^{13}
a_3	1.024×10^{11}	4.085×10^{11}
a_4	-7.616×10^{7}	4.019×10^{7}
a_5	2.253×10^{4}	2.279×10^{4}
a_6	-4637	2062

In order to compare the Satlantic calibration versus the NIST calibration for radiance, the measured radiance, $L_S(\lambda) = \overline{S}_N(\lambda)/D_S(\lambda)$ was first determined using the Satlantic calibration factors, $D_S(\lambda)$, and the net signal, $\overline{S}_N(\lambda)$. The ratio $H(\lambda)$ is the measured radiance divided by the calculated radiance from (16), where

$$H(\lambda) \;=\; \frac{\overline{L}_S(\lambda)}{L_C(\lambda)}, \tag{17}$$

is used to compare the NIST results with the Satlantic calibrations.

The spectral radiances measured by the SXR were determined from the net average voltages for each of the six measurement channels using the measurements of the shadowed and fully illuminated plaque. The SXR was used with a gain of 10 for the measurements. The spectral radiance, as measured by the SXR [$\overline{L}_{SXR}(\lambda)$] was determined using

$$\overline{L}_{SXR}(\lambda) \;=\; \frac{\overline{S}_N(\lambda)\, k_{10}(\lambda)}{D_{SXR}(\lambda)}, \tag{18}$$

where $D_{SXR}(\lambda)$ is the calibration coefficient, $k_{10}(\lambda)$ is the gain correction factor, and $\overline{S}_N(\lambda)$ is the net signal found using (9). The values for $D_{SXR}(\lambda), k_{10}(\lambda)$, and the SXR measurement wavelengths are given in Table 27. Because the SXR was used on gain 10, there is a correction for the gain factor of about 0.04%. Typically, separate SXR data corresponded to each OCR-200 measurement. The SXR measurements were time averaged over these intervals.

Table 27. SXR measurement wavelengths, calibration coefficients, and gain factors.

λ [nm]	$D_{SXR}(\lambda)$ [V cm^{2}sr nm μW^{-1}]	$k_{10}(\lambda)$
411.22	1.101185	0.1000351
441.50	1.468061	0.1000351
486.94	0.2442614	0.1000351
547.87	0.2425734	0.1000351
661.72	0.2604715	0.1000351
774.77	0.03013285	0.1000351

5.3.2 Repeatability

Figure 23a shows the plot of the ratio found using (17) for the sensor UWR measured over three consecutive days from 24–26 July 1996. Between the daily measurements, the sensor was dismounted and remounted on the holder, and the translation stage with the FEL lamp was moved, but was put back into the same position before each measurement. Figure 23a indicates a trend in the measured radiance over the three days. For the SXR, the ratio is the spectral radiance measured by the SXR divided by the calculated radiance,

$$H'(\lambda) \;=\; \frac{\overline{L}_{SXR}(\lambda)}{L_C(\lambda)}. \tag{19}$$

Figure 23b shows $H'(\lambda)$ does not change over the three day interval. This indicates that the trend observed with the UWR is probably due to variations in the alignment of this

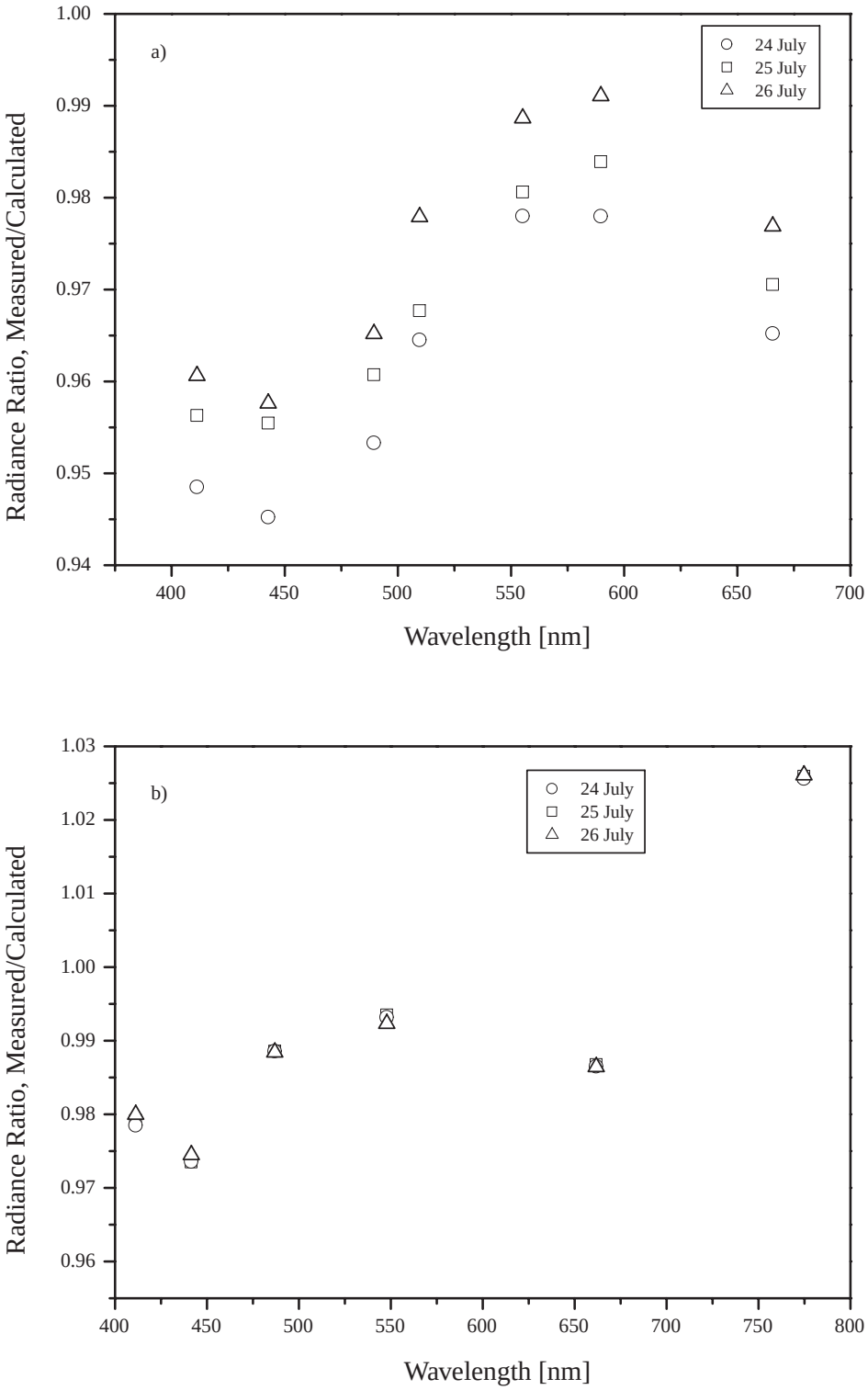

Fig. 23. The Lab VI radiance ratios, which are equal to the measured radiance divided by the radiance calculated from the irradiance standard and the diffuse plaque for sensor UWR and the SXR. Three consecutive days are shown: **a)** the ratios $H(\lambda)$ for the UWR; and **b)** the ratios $H'(\lambda)$ for the SXR.

sensor or changes in its responsivity, not due to changes in other factors, such as the position of the lamp, the irradiance from the lamp, or the measurements of scattered light.

For a closer examination of the temporal stability of UWR, the percentage difference from the mean is plotted using (13) and (14) from Sect. 4.3. Figure 24a is a plot of the percentage difference of the individual ratios from the mean taken from Fig. 23a. The increase over the three days is evident, and the percentage of uncertainty, as estimated from the standard deviation over the three days, is shown in Table 28.

Table 28. The standard deviation of the percentage difference of the ratios $H(\lambda)$ from their mean for the UWR instrument.

λ [nm]	σ' [%]
411.2	0.64
442.7	0.69
489.4	0.63
509.6	0.72
555.2	0.57
589.7	0.67
665.7	0.60

There is also a corresponding increase in the statistical uncertainty in the net signal found from the RSS of the relative standard deviation of the total signal and the background signal over the three days of measurement. An increase in the standard deviation on the third day is listed in Table 29.

Table 29. The relative standard deviation of the net signal of the UWR instrument for three days during SIRREX-5.

λ [nm]	σ' [%]		
	24 July	25 July	26 July
411.2	0.052	0.055	0.196
442.7	0.034	0.039	0.177
489.4	0.023	0.026	0.164
509.6	0.026	0.025	0.157
555.2	0.100	0.046	0.161
589.7	0.016	0.018	0.133
665.7	0.062	0.028	0.128

The SXR measurements have a far smaller spread in radiance values (Fig. 24b). The standard deviations of the SXR measurements are shown in Table 30 and are an order of magnitude smaller than that of the UWR measurements.

By examining the raw data, some of the causes for the change in the measured radiance become apparent. Figure 25a shows the total signal counts as a function of time sequence for the 665.7 nm channel of the UWR sensor measured over three days. The discontinuity in counts at about 1,000 (arbitrary units) on the ordinate, corresponds to the beginning of the measurement for the second day, and similarly, the discontinuity at about 1,600 indicates the beginning of measurements for the third day. Aside from the increase in counts over the three days, there is a downward drift of the counts on 24 July, and also an increase in the random noise on 26 July. The baffled background signal shown in Fig. 25b for the same channel, also shows discontinuities between the daily measurement sets, as well as an increase in the noise on the third day. The other channels for UWR at shorter wavelengths show the same trends in the raw data, but with less drift on 24 July than that seen in the 665.7 nm channel. Because the SXR gave the same output voltages with the same measurement precision, the variability illustrated in Fig. 25 with the UWR must be associated with the alignment of the UWR, its internal electronics, or some other systematic effect.

Table 30. The standard deviation of the ratios $H'(\lambda)$ for 24–26 July.

λ [nm]	σ' [%]
411.22	0.074
441.50	0.055
486.94	0.009
547.87	0.060
661.72	0.016
774.77	0.024

During Lab VI, the PWR sensor was also calibrated for radiance responsivity. On 24 July, the PWR instrument was measured just before the measurement of the UWR instrument; on 25 July, the PWR instrument was measured just after the measurement of the UWR instrument. Any changes due to the changes in the laboratory conditions should be apparent in the radiance measurements done with the PWR instrument. Figure 26a is a plot of the ratio $H(\lambda)$ for the PWR instrument and shows that, within the uncertainty of the measurement, the radiance did not change over the two days. On the second day the channel 6 signal changed by more than 5% during the measurement interval, while the channel 5 signal was stable to within 0.03%. Also on the second day, the channel 7 reading remained near the background level, independent of the illumination conditions. The radiance stability in this spectral region is supported by the data from the SXR as shown in Fig. 26b, which indicates constant values for $H'(\lambda)$ between the two days.

Another check of the instrumental repeatability in Lab VI are the measurements using the JWR instrument, which was used immediately after the UWR instrument on both 24 and 26 July. Figure 27a illustrates the ratios $H(\lambda)$ for these two days. The ratio increased on 26 July, from less than 0.2% at the longest wavelengths to almost 1.5% near 550 nm. However, simultaneous measurements with the SXR, plotted in Fig. 27b, show that the ratio $H'(\lambda)$ decreased slightly on the second day.

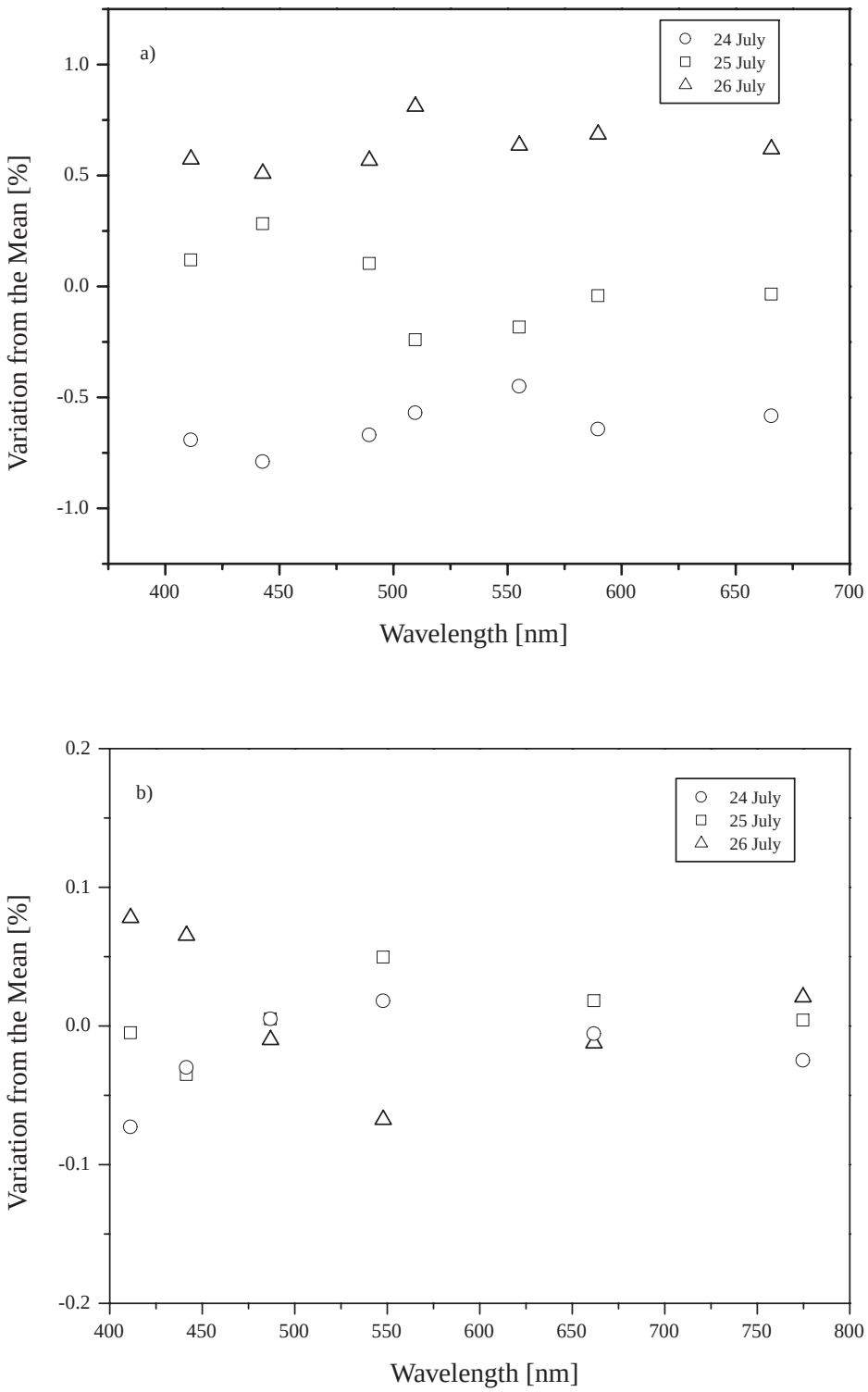

Fig. 24. The variation of the radiance ratios about their mean values (Fig. 23): **a)** the variation in $H(\lambda)$ for the UWR sensor normalized to the mean value; and **b)** the variation in $H'(\lambda)$ for the SXR normalized to the mean value.

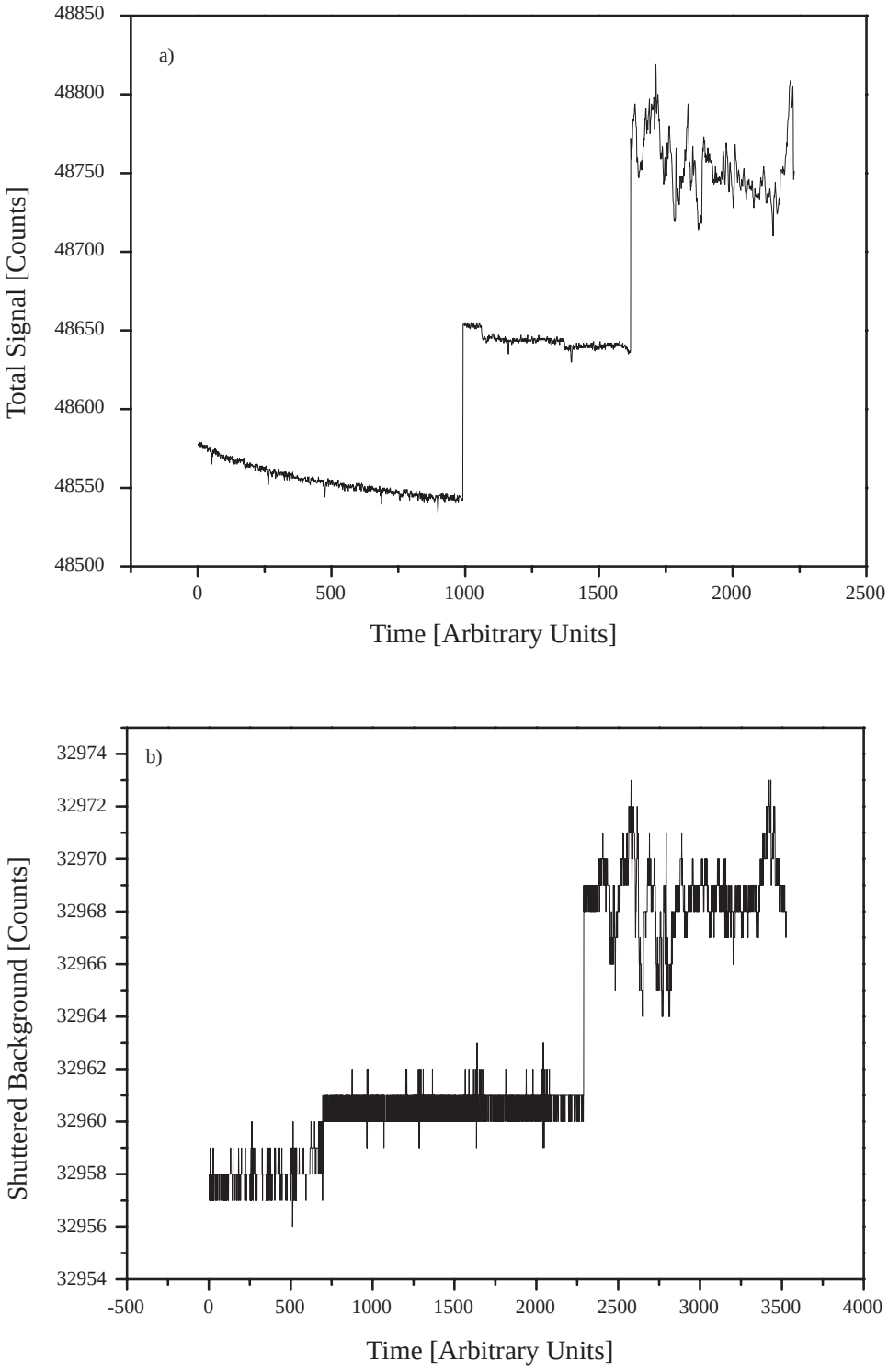

Fig. 25. The digital counts as a function of time sequence for one channel of the UWR instrument. **a)** The total signal counts at 665.7 nm. The values in the time sequence correspond to: 0–1,000 for 24 July; 1,000 to about 1,600 for 25 July; and the remainder for 26 July. **b)** The ambient signal counts at 665.7 nm. The values in the time sequence correspond to: 0–700 for 24 July; 700 to about 2,300 for 25 July; and the remainder for 26 July.

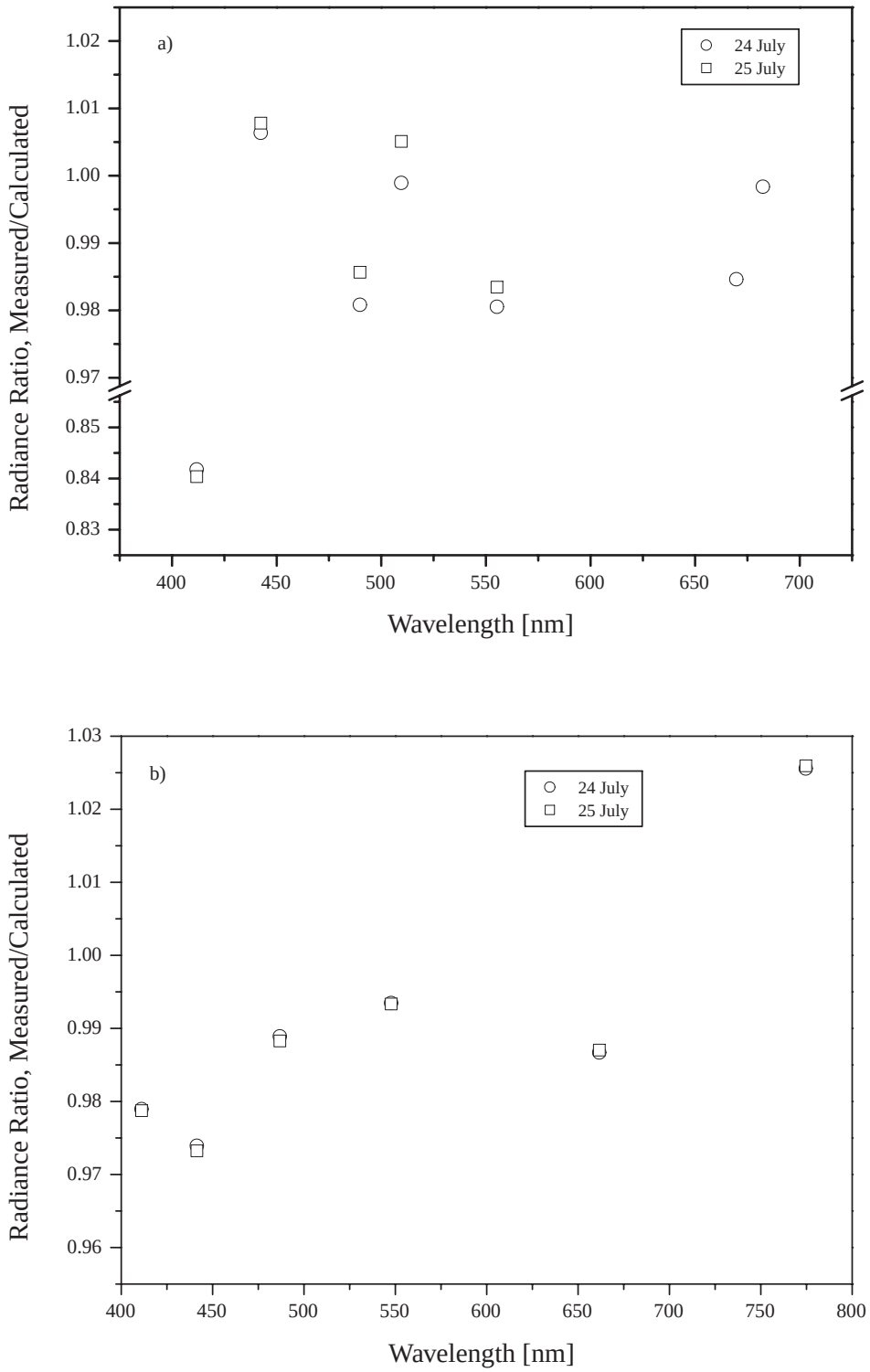

Fig. 26. The Lab VI radiance ratios, which are equal to the measured radiance divided by the radiance calculated from the irradiance standard and the diffuse plaque for sensor PWR and the SXR. Two consecutive days are shown: **a)** the ratios $H(\lambda)$ for the PWR; and **b)** the ratios $H'(\lambda)$ for the SXR.

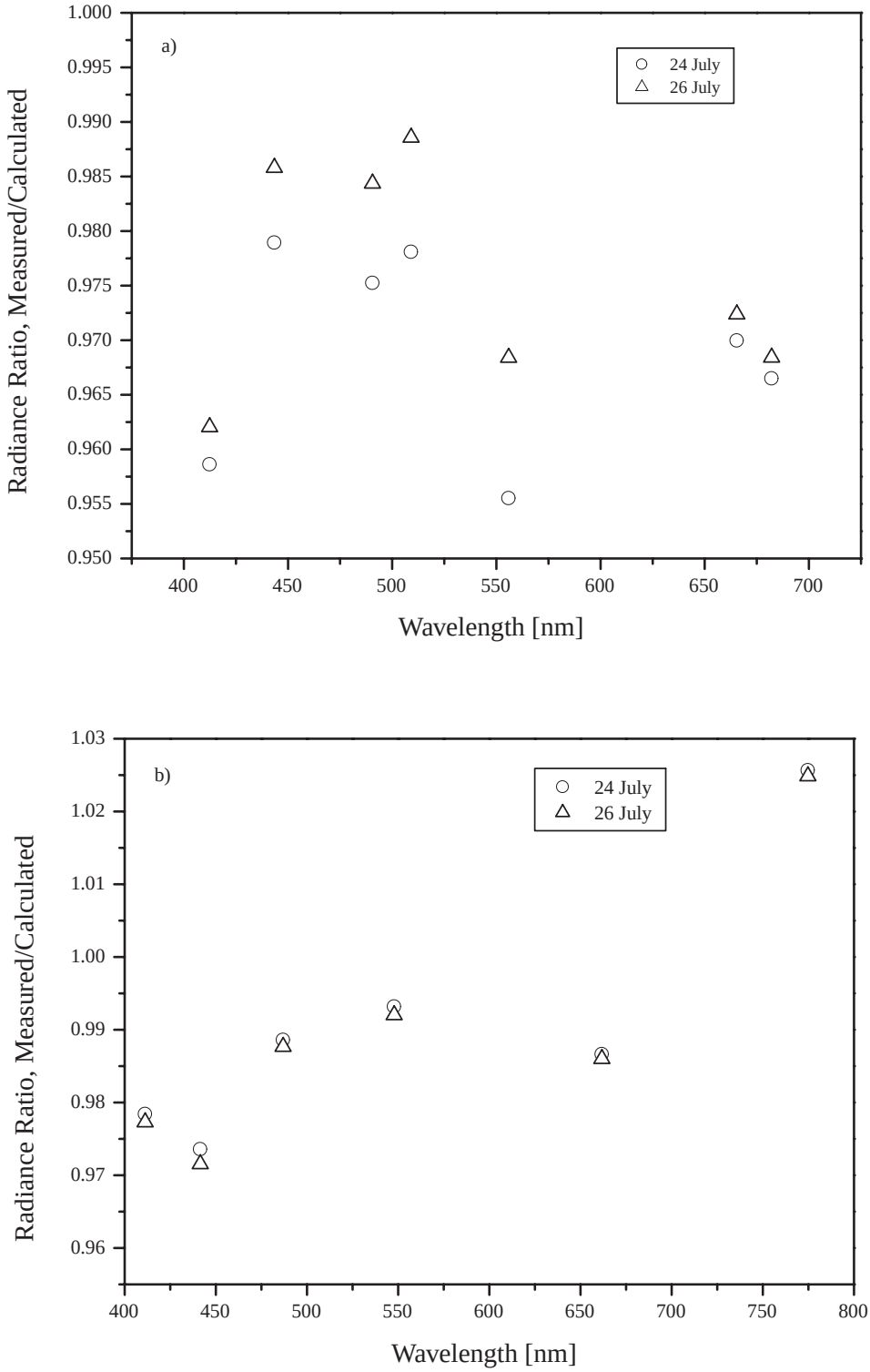

Fig. 27. The Lab VI radiance ratios, which are equal to the measured radiance divided by the radiance calculated from the irradiance standard and the diffuse plaque for sensor JWR and the SXR. Two days are shown: **a)** the ratios $H(\lambda)$ for the JWR; and **b)** the ratios $H'(\lambda)$ for the SXR.

The radiance measurements, which are repeated over three days with the different combination of three instruments, indicate that the total measurement uncertainty in Lab VI is dependent on repeatability of the sensor measurements. The temporal overlap of the measurements with the SXR eliminates other causes, such as systematic effects (lamp-to-plaque distance, lamp current, and consistency of ambient background measurements). The temporal variability in the radiance measurement observed in the JWR and PWR instruments is consistent with the percentage standard deviations in Table 28.

5.3.3 Geometric Effects

The SXR was used to measure radiance on 24 July for three different lamp-to-plaque distances. The distances were measured using the standard reference point, which is the front of the posts in the lamp base. In order for an accurate application of the r^{-2} scaling law to determine the irradiance on the surface of the plaque, (16), the correct radiometric reference point should be used. In FEL lamps, the diameter of the posts is 6.35 mm, and if the filament is centered over the mounting posts, the scaling law $[50.32/(r+0.32)]^2$ would seem appropriate (with r in centimeters). With this radiometric offset, then the calculated radiance from the plaque, using (16), will be larger than that calculated using the front of the posts as the reference surface. The bias increases with increasing lamp distance; at 150, 172, and 197 cm it is 0.850.95%, respectively.

The ratios for the SXR measurements at these three distances are shown in Fig. 28a. The radiance was calculated using the front of the posts as the reference surface. The SXR data do not support an offset in the radiometric distance of 0.32 cm (Fig. 28b). If variations in the other experimental parameters are assumed to be negligible, then the relative ordering, from most positive to the most negative, of the values should coincide with the 197 cm to the 150 cm values. No clear pattern is evident. This result is in contrast with other recent work. Biggar (1999) found he could improve the standard deviations of fits of experimental data by a factor of 10 using a scaling law modified for a radiometric offset. This work involved irradiance, not radiance measurements, and the lamp distance was varied from 1–1.5 m. Y. Ohno (pers. comm.) points out that the actual radiometric distance offset may depend on the filament structure of each lamp, because of coil shading effects. An alternative explanation for the SIRREX-5 SXR scaling law results is that the measurements were affected disproportionately by scattered light at each of the three distances. The uncertainty in the lamp-to-plaque distance is not a likely source of error, because the precision was a few micrometers and a small systematic offset does not affect the predicted ordering of the values. Table 31 gives the standard deviation of the results from Fig. 28b.

To determine whether the measurements were sensitive to the changes in the viewing area on the plaque, the JWR instrument was rotated about its geometric axis. Typically, the Satlantic radiometers were mounted with the shortest wavelength channel in the uppermost vertical position. On 26 July, the JWR instrument was measured with each of the channels in turn occupying the uppermost vertical position. Any effect due to viewing a different area on the plaque, however, was overwhelmed by the instrumental drift as shown in Table 32. Although the measurements were taken immediately after one another, there is an abrupt change in the standard deviation between measurement sessions. For a single measurement set, the signal in all seven channels drifted with identical shape in time, although with different peak-to-valley amplitudes. A plot of the data is not shown because any differences in the signal with rotational position were smaller than the observed instrumental variability.

Table 31. The standard deviation of the percentage difference from their mean of the ratios at three different distances.

λ [nm]	σ' [%]
411.22	0.43
441.50	0.49
486.94	0.43
547.87	0.47
661.72	0.39
774.77	0.44

Table 32. The relative standard deviations, in percent, from the JWR measurements on 26 July. The column heading denotes that the particular channel on the sensor was placed in the uppermost vertical position.

λ [nm]	412.4	443.5	490.6	509.1	555.9	665.4
412.4	0.11	0.24	0.34	0.35	1.64	2.15
443.5	0.06	0.22	0.31	0.33	1.53	2.00
490.6	0.05	0.19	0.28	0.29	1.38	1.79
509.1	0.04	0.18	0.27	0.28	1.33	1.73
555.9	0.06	0.17	0.24	0.26	1.23	1.59
665.4	0.02	0.14	0.21	0.22	1.03	1.33
682.1	0.02	0.13	0.20	0.22	1.01	1.30

5.3.4 Calibration

Because the calibration factor is the calculated radiances divided by the net counts, the total uncertainty is the RSS of the individual uncertainties in the radiances and the net counts. The components of uncertainty are given in Table 33; because all of the calibrations for the radiance sensors by NIST were performed using the plaque method, these uncertainties are appropriate for the NIST calibration factors.

The uncertainty in the irradiance in the FEL lamp operated in the vertical position (Table 25) is from the FASCAL calibration. As in Sect. 4, there is an interpolation

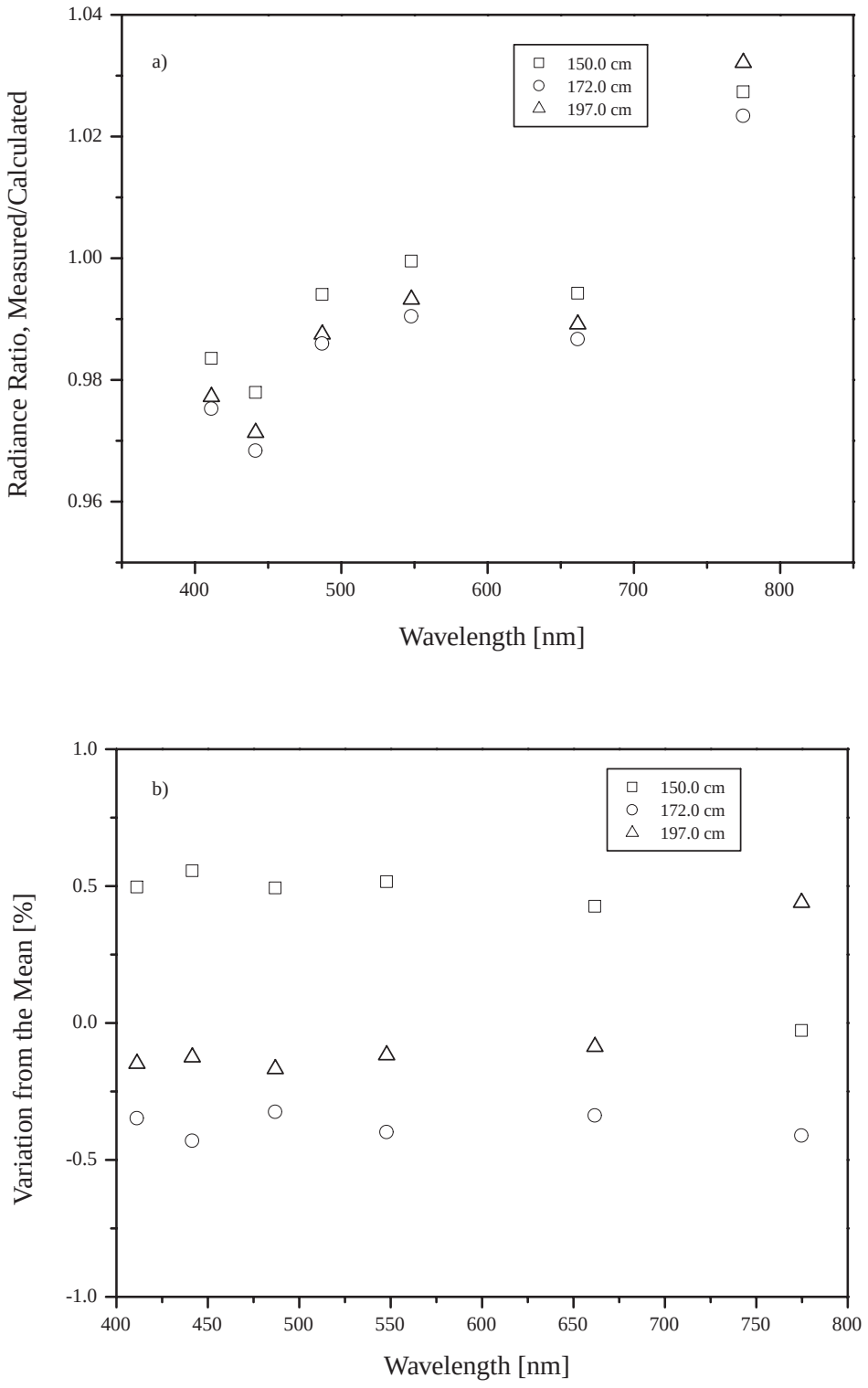

Fig. 28. Radiance ratios in Lab VI as a function of the lamp-to-plaque distance, for three separate distances: **a)** variations in the ratios $H'(\lambda)$; and **b)** the variation in the individual ratios shown in panel **a** about their mean value.

Table 33. Relative standard uncertainties, in percent, for the radiance calibration of the UWR instrument using the plaque method.

	λ [nm]						
Component of Uncertainty	411.2	442.8	489.6	509.5	555.3	589.0	665.5
Lamp Irradiance	0.37	0.34	0.32	0.32	0.31	0.32	0.34
Interpolation	0.30	0.30	0.30	0.30	0.30	0.30	0.30
Lamp Current	0.02	0.02	0.02	0.02	0.02	0.02	0.01
Irradiance Distribution	0.88	0.88	0.88	0.88	0.88	0.88	0.88
Plaque Reflectance	0.87	0.87	0.87	0.87	0.87	0.87	0.87
Alignment, lamp-to-plaque	0.45	0.45	0.45	0.45	0.45	0.45	0.45
Distance Scaling Law	0.30	0.30	0.30	0.30	0.30	0.30	0.30
Wavelength	1.51	1.22	0.91	0.80	0.60	0.48	0.29
Signal	0.64	0.69	0.63	0.72	0.57	0.67	0.60
RSS Total	2.16	1.98	1.78	1.76	1.61	1.61	1.55

component of uncertainty. Here, the component of uncertainty related to the lamp current is based on a systematic uncertainty of 0.15 mA and a random uncertainty of 0.18 mA (Early et al. 1998c).

The models described in Appendix D of Early et al. (1998c) were used to estimate the uncertainty associated with a receiver aperture greater than that used in FASCAL and the non-ideal goniometric distribution of the lamp irradiance. In this case, the *receiver aperture* is the area of the illuminated plaque viewed by the Satlantic radiometer. The effect of a 1.5% uncertainty in the plaque reflectance factor was modeled according to a uniform probability distribution.

As with the field calibrator, the alignment component of uncertainty includes the effects of the uncertainty in the distance, perpendicularity between the lamp and the receiving aperture, and co-alignment of these elements on the proper optical axis. Again, the treatment presented in Appendix D of Early et al. (1998c) was followed. The estimated uncertainty in the distance is 0.2 cm, the degree of perpendicularity is 0.5°, the offset uncertainty in the lamp is 0.1 cm, and the offset uncertainty in the central channel of the UWR sensor is 0.3 cm. As in Sect. 4, the uncertainty in the sensor wavelengths is estimated to be 1 nm, resulting in up to a 1.5% uncertainty at 411 nm.

The final component of uncertainty in Table 33 corresponds to the measurement precision. The standard deviation of the UWR results for the three measurement days are given; these values will be different for other sensors, but the other components of uncertainties in Table 33 should be constant. Table 34 lists the calibration factors for the sensors measured in Lab VI. The wavelengths are nominal values for the individual channels.

6. ADDITIONAL TOPICS

This section summarizes the remaining two SIRREX-5 laboratory sessions, Lab VII with the SQM, and Lab VIII "Selected Topics." The irradiance lamp calibrations and the A/D measurements are also discussed.

6.1 SQM

The SQM was developed as a portable field source to monitor the stability of sensors such as the Satlantic OCR and OCI series during ocean cruises (Johnson et al. 1998b). The performance of the SQM during the third Atlantic Meridional Transect (AMT-3) cruise is reported in Hooker and Aiken (1998), where the stability of the field radiometers was established to be 1% or better. During SIRREX-5, which took place two months before the AMT cruise, the SQM was used in Lab VII to monitor the stability of the BSI radiometers CAI, CWI, and CWR over a four day interval. All measurements took place at Little Seneca Lake. The enclosed interior of the truck, which was rented to transport equipment from NIST to Little Seneca Lake, served as the SQM laboratory. The truck and SQM electronics module are visible in Fig. 16. The objective of Lab VII was to provide additional experimental data on the SQM and to demonstrate the operation and utility of a portable field source.

The SQM contains three internal filtered detectors, one is broadband and the other two are centered at about 425 nm and 625 nm. During SIRREX-5, the filters and detectors in the internal monitor detectors were stabilized to 40°C using the SQM temperature controller. The two sets of lamps in the SQM were set to constant current values of 3.15 A and 0.961 A, respectively. Each set of lamps contains eight bulbs. The voltage drop across each lamp was recorded each day; the standard deviation of these readings was 4.5 mV for the high-current set, and 2.4 mV for the low-current set. During the measurements with the CAI, CWI, and CWR sensors, the three internal detectors were stable to within 0.3%.

As for the CAI, CWI, and CWR sensors, the output of the SQM was too low for the channel at 380 nm; improvements to the SQM would have to be made before it could

Table 34. The calibration factors measured at NIST, in units of $\mu W\,cm^{-2}\,nm^{-1}\,count^{-1}$. The instrument GWR was measured only once, and the others are averages of two (JWR and PWR) or three (UWR) separate measurements.

	F_{NL}				
λ [nm]	UWR	JWR	PWR	GWR	SWQ
411	9.373×10^{-5}	1.913×10^{-4}	1.400×10^{-4}	5.245×10^{-4}	9.827×10^{-5}
443	9.650×10^{-5}	1.680×10^{-4}	8.542×10^{-5}	5.355×10^{-4}	9.247×10^{-5}
490	8.795×10^{-5}	1.721×10^{-4}	5.698×10^{-5}	5.994×10^{-4}	9.285×10^{-5}
510	9.451×10^{-5}	1.923×10^{-4}	5.697×10^{-5}	5.605×10^{-4}	5.819×10^{-5}
555	9.105×10^{-5}	1.859×10^{-4}	5.162×10^{-5}	5.883×10^{-4}	5.468×10^{-5}
590	8.417×10^{-5}				
667	5.697×10^{-5}	1.002×10^{-4}	3.620×10^{-5}	6.126×10^{-4}	3.711×10^{-5}
683		1.325×10^{-4}	3.636×10^{-5}	5.305×10^{-4}	3.819×10^{-5}

be used below about 400 nm. The output of the SQM was also rather low for the broadband photosynthetically available radiation (PAR) channels in CAI and CWI, with net signals below 100 mV. Also, useful data were not obtained with the 683 nm channel of CWR. Figure 29 gives the results obtained from the measurements with CAI, CWI, and CWR with the SQM. For each measurement channel, the results of the four days of measurements were averaged; these averages were used to normalize the results at each channel. The standard deviation of these averages was between 0.5–1.5%, except for the PAR channels, which produced standard deviations of 0.1% and 0.5% for CAI and CWI, respectively. For CAI and CWI, the 31 July measurements were between 1–1.5% higher than the other three days.

Immediately after SIRREX-5 (31 July to 3 August), in preparation for the AMT cruise, the SQM was used with GWI, PWI, GAI, PWR, GWR, SWQ, and GWE at NIST. The results are reported in Shaw et al. (1997). Then, after some minor modifications (a new lamp ring and a change in the gain of the internal detector's amplifier), the SQM was used in the AMT-3 cruise.

6.2 Lab VIII

The objective of Lab VIII ("Selected Topics") was to illustrate topics in radiometric calibration that are sometimes neglected or not considered. Practically speaking, Lab VIII was necessary to provide a relevant activity for all of the eight groups on every afternoon during SIRREX-5.

During the first day, 23 July, the Lab VIII activity consisted of using an irradiance detector mounted on an x, y translation stage to map the irradiance distribution of an FEL standard lamp. This study is relevant to the use of large diffuse plaques, illuminated by a standard of spectral irradiance, to produce known values of spectral radiance. The concept is simple: mount the radiometer on the translation stages some distance from the lamp, with the plane of the two-dimensional scan perpendicular to the optical axis of the radiometer. The lamp and the radiometer are aligned so that scanned array is centered on the lamp. The method consists of acquiring repeated scans (e.g., in the horizontal, or x direction) at different vertical locations. After each horizontal scan, the radiometer is positioned at the central location to monitor the stability of the lamp. The spatial uniformity of the irradiance distribution should be incorporated into the calculation of the spectral radiance from an illuminated diffuse plaque [e.g., Heath et al. (1993)].

On 24 and 26 July, Lab VIII took the form of a miniworkshop. A summary of the SOOP (Mueller and Austin 1995), published in the *SeaWiFS Technical Report Series*, was used as the starting point of the discussions. On 24 July, the session concentrated on in-water radiometry, specifically buoys and moorings. On 26 July, the topic was above-water radiometry. An additional session on laboratory calibration protocols was planned for 29 July, but the field site restoration was performed instead.

On 25 July, a commercial illuminance meter was taken to the in-air site at the NIST pond for Lab VIII. Because the spectral response function in illuminance meters is known, the concept was to compare the measured illuminance to the value expected from the downwelling spectral irradiance, thus providing an additional verification of the accuracy of the irradiance sensors. The values for $E_s(0^+, \lambda)$ were supplied by temporally simultaneous SAI data (the grating instrument), and the participants had the opportunity to analyze the data.

6.3 A/D Calibrations

A standard procedure at NIST for characterizing Si, Ge, or InGaAs radiometers is linearity measurements of the transimpedance amplifier. This amplifier converts the photocurrent from the detector to a voltage, usually with selectable gain. The analog voltage is then digitized by a commercial DMM. For the linearity measurements, the photodiode is replaced with a precision current source, and the radiometer is designed to exercise this option. Under computer control, the voltage produced by the amplifier is measured for the full range of relevant input currents. The commercial DMM is calibrated annually.

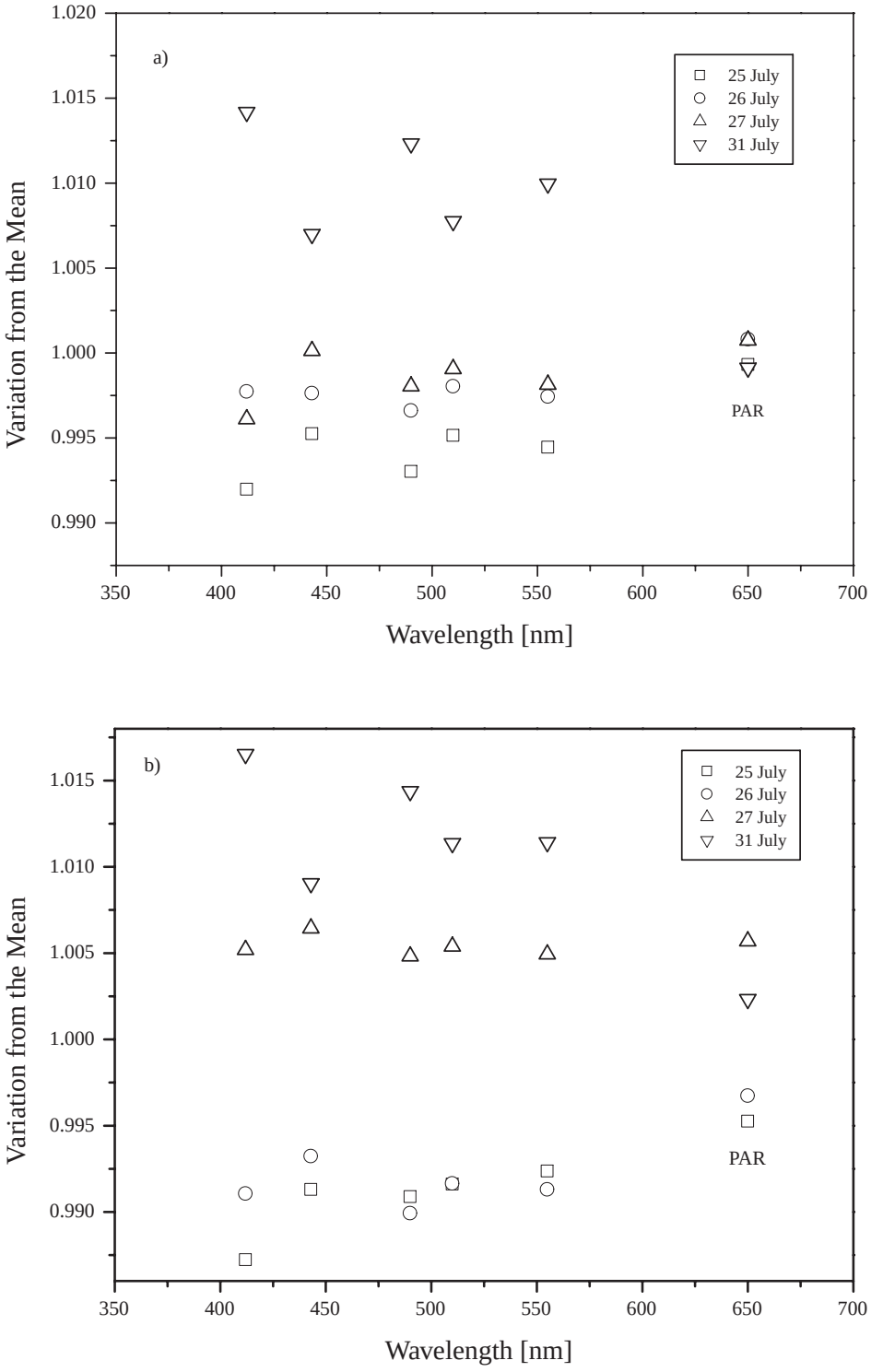

Fig. 29. Variations in the net signals for the field sensor measurements with the SQM. For each wavelength or channel, the results for each of the four days, normalized by the average, are plotted. In **a)** and **b)**, the variations recorded by the sensors CAI and CWI, respectively, for each measurement wavelength are plotted as a function of wavelength. The broadband PAR channel is plotted at 650 nm for the purpose of illustration.

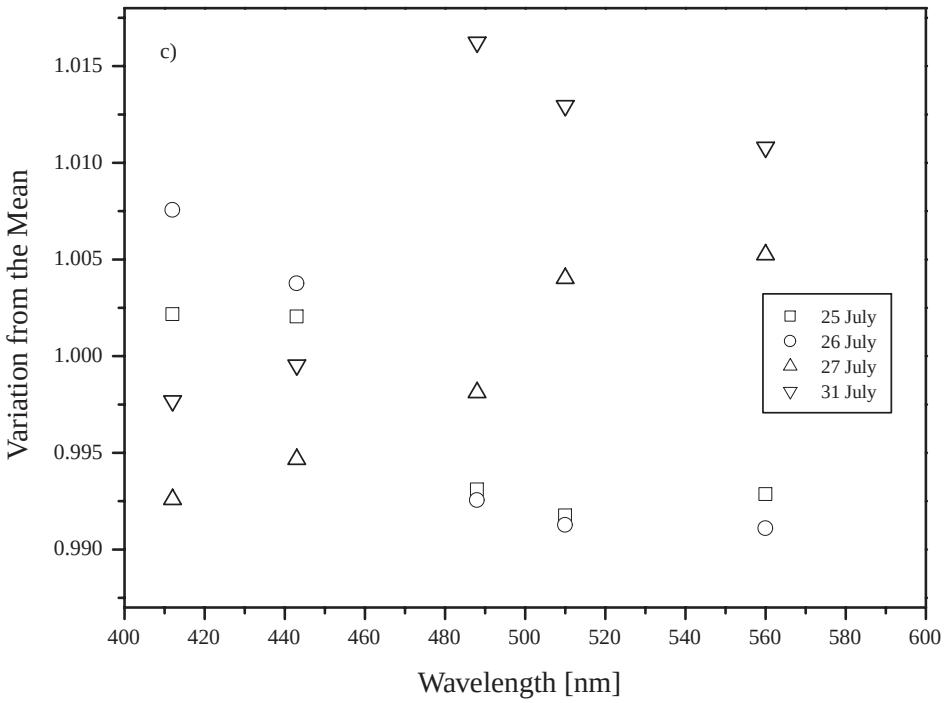

Fig. 29. (cont.) Variations in the net signals for the field sensor measurements with the SQM. For each wavelength or channel, the results for each of the four days, normalized by the average, is plotted. **c)** The variations recorded by CWR are plotted as a function of wavelength.

The field radiometers studied at SIRREX-5 are similar in design, except that the commercial multimeter is replaced by an A/D circuit which is housed in a watertight container, and the transimpedance amplifier could not be separated from the detector for electrical characterization. Only the performance of the A/D units (Table 3), therefore, was assessed using the NIST amplifier linearity setup. A precision voltage source (Keithley model 263), under computer control, was substituted for the computer-controlled current source. The output voltage, representing the output of one channel in the Satlantic OCR or OCI sensors, was input to the A/D unit [Satlantic model OCP or the Multichannel Visible Detection System (MVDS)]; the digital counts corresponding to this voltage were recorded by the SAS-II data acquisition system. Satlantic provided a pigtail cable for the interface between the Keithley voltage source and the A/D units. At the same time, the output voltage from the Keithley voltage source was input to an HP 3458A DMM and recorded using custom data acquisition software in QuickBasic (Microsoft Corp.). Regression of the voltage recorded by the 3458A and the digital counts is a measure of the linearity of the A/D unit.

The analysis of the data was complicated by extraneous values that were recorded as the NIST amplifier linearity program was changing the voltage; there was no synchronization between the two systems. Figure 30 shows, as an example, the regression for the L1 A/D (OCP-100, number 004); the voltage step was 50 mV, resulting in 101 data points. Only the data for the $E_d(\lambda)$ port of L1 are shown, and not every point for each of the seven channels is plotted. The linear correlation coefficient was equal to unity for the seven channels shown in Fig. 30. Averaged over the seven channels in L1 for the $E_d(\lambda)$ port, the offset is 32,769.9±1.7 counts and the slope is 6,549.48±0.53 counts V^{-1}. The results for the $L_u(\lambda)$ port in L1 and the other units were similar in terms of the degree of linearity exhibited by the A/D units.

6.4 Lamp Calibrations

One of the prime objectives in previous SIRREXs was to intercompare the standards of spectral irradiance, e.g., FEL-type lamps used by various laboratories to calibrate irradiance and radiance sensors (using the plaque method). At SIRREX-1 to SIRREX-3, this proved to be a time consuming activity, although with careful work and repeated calibrations of the transfer radiometer (a single-grating scanning monochromator), a transfer uncertainty of about 1% was achieved (Mueller et al. 1996). SIRREX-4, which took place at NIST and emphasized training and demonstration of protocols, offered no opportunity for lamp intercomparisons.

A compromise was offered for SIRREX-5, in response to the observation that the standard lamps were being neglected: FASCAL was scheduled for spectral irradiance

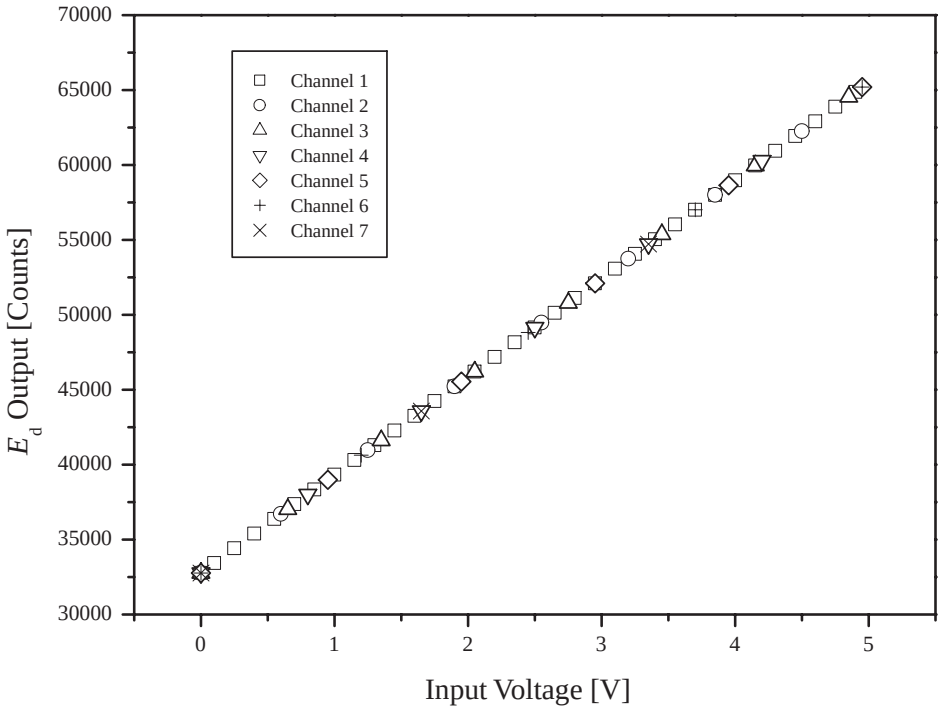

Fig. 30. Results of the A/D calibration for the $E_d(\lambda)$ port of unit L1. For each channel, the output in counts is plotted as a function of the input voltage. For clarity, not every point is shown; of the 101 points for each channel, the actual number plotted varies from 33 to 3.

calibrations for July 1996, so the participants could hand-carry their lamps to and from NIST. The cost of the calibration was not altered or reduced, and the production of the calibration report was not altered from the normal procedures, so the prime benefit was the hand delivery and the opportunity to visit FASCAL. The purchase orders for the lamp calibrations were due prior to SIRREX-5.

Only two laboratories took advantage of the opportunity to hand-carry lamps to and from NIST: MLML and Satlantic. The group at MLML is part of the NOAA MOBY project. MLML sent two lamps, one of which arrived damaged and was not calibrated. Satlantic sent one new lamp, F-409, which was calibrated by Optronic Laboratories, Inc. (OL) on 25 April 1996. The undamaged MLML lamp, F-307, participated in SIRREX-1 (Mueller 1993), SIRREX-2 (Mueller et al. 1994), and SIRREX-3 (Mueller et al. 1996). Lamp F-307 acquired 25.6 h since its last calibration at SIRREX-3.

Each lamp was measured three times on FASCAL by comparing it to three different primary working standards (see Walker et al. 1987 for a description of FASCAL). The spectral irradiance at 50 cm distance, from 350–900 nm (beginning at 900 nm) was determined separately for each lamp. As is standard practice on FASCAL, the lamp current was set using a calibrated shunt resistor, the voltage drop across the lamp was monitored, and the output of the primary working standards and the test lamps were recorded by ancillary filter radiometers (a photometer and a UV radiometer).

Figure 31 shows the history of F-307. The lamp was supplied by OL; they calibrated the lamp in June 1992. These data from OL are used to normalize the results; the quantities plotted correspond to the SIRREX result minus the OL result, divided by the OL result. The change in F-307 between SIRREX-3 (which used the portable single-grating monochromator), and SIRREX-5 (which used FASCAL), is between 0.5–1%.

7. NIST CALIBRATIONS

One of the essential activities at SIRREX-5 was the calibration and characterization of the radiometers listed in Table 2 by NIST personnel using NIST methods, calibrated sources, and detectors. The comparison of these NIST calibration coefficients to those provided by the owner of the sensor is one indicator of the accuracy of the radiometers, although there are many other factors that must be considered when reducing and analyzing in-water or in-air radiometric data. The NIST laboratory calibrations also provided a method to determine the repeatability and reproducibility of the instruments by performing multiple measurements in the laboratory on different days and by using the field calibrators, such as the UV Intercomparison Field Calibrator.

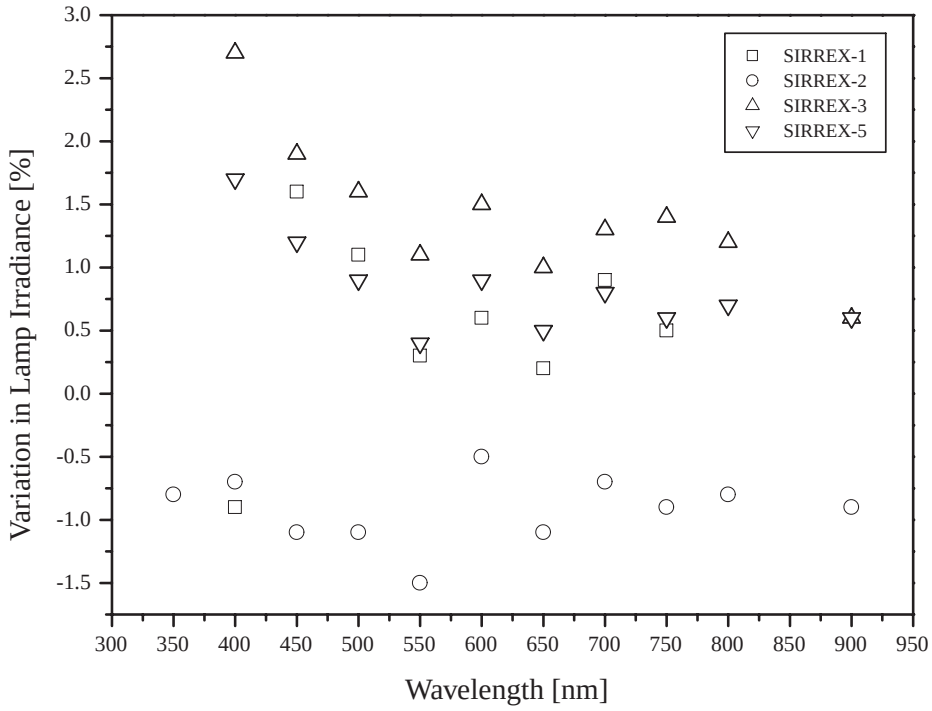

Fig. 31. The relative variation in the spectral irradiance of FEL lamp F-307. The quantity plotted corresponds to (SIRREX− OL)/OL, in percent. The SIRREX-5 results correspond to a NIST calibration on the FASCAL facility.

7.1 Overview

The calibrations were limited by the resources available (time, NIST personnel, and the use of NIST facilities) and the existing capabilities at NIST (e.g., no in-water characterization facilities). The wavelength accuracy of the PS2-903 units was determined using a HeNe laser, and gas discharge sources (Ne and Hg). The relative spectral responsivity of the filter radiometers was not determined, because these measurements require many hours of data acquisition and analysis, e.g., about 170 h of data acquisition was required for full spectral characterization of the SXR (Johnson et al. 1998a). The irradiance sensors were calibrated using a standard lamp (FEL lamp F332) at 50 cm. The radiance sensors were calibrated using the plaque method, in the same facility as described in Sect. 5 (Lab VI).

The irradiance and radiance calibration facility was designed to be compatible with the plaque laboratory (Lab VI) so that the in-air sensors (Lab III) could be calibrated in the mornings while the meeting activities were in session elsewhere. Kinematic design of the mounts and the use of the accurate translation stage were implemented, to produce rapid and accurate results.

As described in Sect. 5, the plaque laboratory consisted of a 60.96 cm, square, Spectralon plaque mounted vertically in a frame on a motorized rotary stage. A motorized linear translation stage assembly with an FEL lamp mount assembly was aligned perpendicular to the plaque; the SXR measured the plaque radiance with a viewing angle of 45°; and the test radiometer measured the plaque with a viewing angle of −45°. The same double V-block and rail system that was used in Lab VI for the Satlantic radiometers was used for the PS2-903 and BSI radiometers. The double V-block, however, was designed for the Satlantic and PS2-903 radiometers; there was no holder for the BSI radiometers because of a planning oversight. The PS2-903 units were mounted onto the double V-block mount at the correct height using an adapter plate, but the height of the BSI radiometer CWR was above the center of the plaque. For the CWR calibrations, the lamp was raised as much as possible, resulting in an offset of about 0.2 cm, which caused a negligible bias in the radiance calibration.

Because evidence at the past SIRREXs indicated that interreflections are a major source of bias in the plaque method of generating a source of known radiance, care was taken to eliminate extraneous sources of radiation. As mentioned in Sect. 5, black cloth was used to cover the walls, ceiling, and laser table, and to separate the area around the laser table from the rest of the laboratory. Only the plaque and a small area around the plaque were illuminated, and the diffuse component of the signal was measured by draping a cloth over the hole in the opaque partition between the lamp and the plaque (Sect. 5).

The irradiance calibrations were performed using a second double V-block assembly which could be placed on the

Table 35. Relative standard uncertainties, in percent, for irradiance calibrations of the filter radiometers in the NIST laboratory using lamp F332.

	λ [nm]						
Component of Uncertainty	411.2	442.7	489.4	509.6	555.2	589.7	665.7
Lamp Irradiance	0.37	0.34	0.32	0.32	0.31	0.32	0.34
Interpolation	0.30	0.30	0.30	0.30	0.30	0.30	0.30
Lamp Current	0.02	0.02	0.02	0.02	0.02	0.02	0.01
Irradiance Distribution	0.41	0.41	0.41	0.41	0.41	0.41	0.41
Alignment	0.47	0.47	0.47	0.47	0.47	0.47	0.47
Wavelength	1.51	1.22	0.91	0.80	0.60	0.48	0.29
Signal	0.26	0.18	0.11	0.09	0.07	0.05	0.04
RSS Total	1.72	1.46	1.20	1.10	0.97	0.90	0.83

laser-lamp-plaque axis using a kinematic mount attached to the laser table. The height was fixed so that once the kinematic mount was positioned correctly, the fixture did not have to be realigned for each irradiance calibration. The rotational position of the irradiance sensors was fixed with the shortest wavelength channel in the highest vertical position. To reduce scattered light, the plaque was covered with a plastic bag† and then covered with black cloth. The linear translation stages were moved to the correct position to result in the desired 50 cm separation between the lamp and the irradiance collector. The distance was measured to the front of the diffuser, which was on the optical axis, and this distance was made repeatable using the D-shaped mounting ring. The distance from the front of the sensor to the front face of the ring, however, had to be increased by 0.74 cm to mount the calibration V-block, and then set back to the position used for the field measurements. More thorough planning would have avoided this extra step.

The BSI irradiance sensors were calibrated using the irradiance V-block, however, as with the CWR sensor, the increased diameter required an adjustment in the lamp height, with the final height of the lamp also about 0.2 cm too low. The resulting bias is calculated to be 0.28%.

For the irradiance calibrations, the diffuse component of the signal was measured by placing a cylindrical tube, covered with black cloth, between the lamp and the irradiance sensor. The location of this on-axis baffle was chosen so that the shadow was cast over all of the irradiance collectors, while keeping the size of the shadow as small as possible.

Typical uncertainties for the radiance calibrations using the plaque method are given in Table 33. The uncertainties for the irradiance calibration are similar to those for the field unit, and are detailed in Table 35 for the filter radiometers calibrated during SIRREX-5. The distance between the lamp and the diffuser was 50±0.1 cm. For the measurement uncertainty, the average of the experimental standard deviations for the same wavelength in the OCI-200 sensors was used.

† The use of plastic or other material containing hydrocarbons with diffuse plaques made from Spectralon or pressed polytetrafluoroethylene is known to alter the reflectance, especially in the ultraviolet (Y. Barnes, pers. comm.), but suitable alternatives were not readily available at SIRREX-5.

7.2 Daily Procedures

7.2.1 Satlantic Radiometers

A group of irradiance sensors (GWI, PWI, UWI, UWE, JWI, GAI, UAI, and SAE) were calibrated using F332 on 18 and 19 July. The A/D unit was L1 for all except UAI and SAE, which were integrated with MVDS-16 and MVDS-17, respectively. On 30 July, the laboratory calibration was repeated. All of the other units, except GAI, were also calibrated in the UV Intercomparison field irradiance calibration (Sec. 4). Unit GWE was only calibrated using the field calibrator.

On 20 July, the laboratory was configured for the radiance calibrations using the large NIST Spectralon plaque. Four radiance sensors (GWR, PWR, JWR, and UWR) were measured, although unsuccessfully. As with the irradiance calibrations, the A/D L1 was used in conjunction with custom software in LabVIEW for the Macintosh operating system. On 18–20 July, this custom data acquisition system operated properly for the irradiance sensors, but not for the radiance sensors, so no data were recorded. The entire sequence of radiance measurements and the first full day of the Lab VI, on 23 July, was completed before the problem was discovered, in part because the software did not display the *real time* results during the measurement procedure. The problem was corrected on 24 July, but there was no time after SIRREX-5 to repeat all of the radiance calibrations. Therefore, for these four critical downwelling radiance sensors, as well as the SWQ, the only calibration data available is from the Lab VI (Sect. 5).

The SAS-II system (composed of the GAE and the GAR sensors, the A/D units, and the PC), was calibrated

twice during SIRREX-5. On 18 and 25 July, GAE was calibrated for spectral irradiance responsivity. On 20 and 24 July, GAR was calibrated for radiance responsivity. These data were obtained using the Satlantic acquisition program that runs under MS-DOS using the option to save the results as raw counts, not in physical units (irradiance or radiance). The purpose of the repeat measurements was to assess the repeatability of the SAS-II system.

7.2.2 BSI Radiometers

On 30 July, after the irradiance calibration of GWI, the lamp was raised to within 0.2 cm of the longitudinal axis of the BSI sensors CAI or CWI, as explained above. On 31 July, the laboratory was reconfigured for radiance calibrations and CWR was calibrated. CWR was rotated about the optical axis in 90° steps, repeating with the starting position, to assess geometric effects.

7.2.3 ASD Spectrometers

A test of the wavelength calibration of the ASD spectrometers, with the irradiance unit SAI, was performed on 16 July using a HeNe laser, and Hg and Ne emission line sources. The accuracy of the wavelength calibration affects the interpretation of the spectral irradiance, radiance, and reflectance data, especially if these quantities vary rapidly with wavelength.

On 18 July, the SAI units were calibrated for irradiance responsivity using F332. The sequence of measurement consisted of acquiring one scan of the shuttered background (the diffuse component) while the lamp was at full operating current, but not fully stabilized, then five scans of the total signal 15 min later. On 22 and 25 July, the irradiance calibration for the SAI was repeated. The radiance calibration for the SAR was performed on 24 July with the unit mounted in the 18° position.

7.3 Results

7.3.1 Satlantic Radiometers

The NIST calibration factors for the OCI-200 radiometers GWI, PWI, UWI, UWE, JWI, GAI, UAI, and SAE are given in Tables 36–43. The factors for GWE are given in Table 44, although these were obtained using the field calibrator, because no laboratory measurements were made. The raw data were analyzed following procedures similar to those outlined in Sect. 4 for the UV field calibrator. The tables state the measurement wavelength, the calibration factor supplied by the owner of the radiometer, the NIST calibration factor, and the ratio of the two calibration factors.

Sensor GWI was calibrated by Satlantic on 26 June 1996. The calibration factors F_S are given in Table 36. The agreement with the NIST calibration factors, F_{NL}, is good, with the mean ratio F_S:F_{NL} equal to 0.999±0.012 with a maximum disparity of 2%. Sensor PWI was calibrated by G. Moore; the PML calibration factors F_{PML} are given in Table 37. Comparison with NIST gives a mean ratio of F_{PML}:F_{NL} equal to 0.980±0.018 with a maximum disparity of 5% at 700 nm. Sensor UWI was calibrated by Satlantic on 15 June 1996; the calibration factors F_S are given in Table 38. The mean ratio F_S:F_{NL} is equal to 0.998±0.013 with a maximum disparity of 2.3%. Sensor UWE was also calibrated by Satlantic on 15 June 1996; the calibration factors F_S are given in Table 39. The mean ratio F_S:F_{NL} is equal to 0.997±0.012 with a maximum disparity of 2.2%.

Sensor JWI was calibrated at the Joint Research Centre (JRC) by G. Zibordi; the calibration factors F_{JRC} are given in Table 40. The mean ratio F_{JRC}:F_{NL} is equal to 0.999±0.014 with a maximum disparity of 2.5%. Sensor GAI was calibrated by Satlantic on 26 June 1996; the calibration factors F_S are given in Table 41. The mean ratio F_S:F_{NL} is equal to 0.999±0.011 with a maximum disparity of 1.8%. Sensor UAI was calibrated by Satlantic on 15 June 1996; the calibration factors F_S are given in Table 42. The mean ratio F_S:F_{NL} is equal to 0.889±0.011 with a maximum disparity of 12.7%. The reason for the overall discrepancy is not known. Sensor SAE was calibrated by Satlantic on 12 June 1996; the calibration factors F_S are given in Table 43. The mean ratio F_S:F_{NL} is equal to 0.981±0.018 with a maximum disparity of 4.5%.

Sensor GWE was calibrated by Satlantic in terms of the output voltage on 18 March 1996. Using the A/D calibration data from the NIST SIRREX-5 values, the net counts during the NIST calibration were converted to voltages for comparing them to the Satlantic results. Channel 1 at 411.5 nm saturated during the NIST measurements and no value for F_{NL} is reported. The mean ratio F_S:F_{NL} is equal to 0.980±0.016 (Table 44) with a maximum disparity of 4.0%.

The NIST calibration factors for the OCR-200 radiometers GWR, SWQ, PWR, UWR, and JWR from the plaque laboratory are given in Tables 45–49. The raw data were analyzed as described in Sect. 5 for the plaque laboratory. The tables list the measurement wavelength, the calibration factor supplied by the owner of the radiometer, the NIST calibration factor, and the ratio of the calibration factors.

The GWR sensor was calibrated by Satlantic on 26 June 1996; the calibration factors F_S are given in Table 45. The mean ratio F_S:F_{NL} is equal to 0.961±0.008 with a maximum disparity of −5.4%. Sensor SWQ was calibrated by JRC on 15 June 1996; the calibration factors F_S are given in Table 46. The mean ratio F_{JRC}:F_{NL} is equal to 0.973±0.014 with a maximum disparity of −5.4%. Sensor PWR was calibrated at PML by G. Moore. The calibration factors F_{PML} are given in Table 47. The mean ratio F_{PML}:F_{NL} is equal to 0.972±0.056 with a maximum disparity of −15.3%, which occurs at the shortest measurement wavelength. Excluding this channel improves the overall agreement, so that the mean ratio F_{PML}:F_{NL} is equal to

Table 36. Calibration factors for GWI compared to the values from Satlantic.

λ [nm]	F_S [μW cm^{-2} nm^{-1} count^{-1}]	F_{NL} [μW cm^{-2} nm^{-1} count^{-1}]	F_S:F_{NL}
413	6.201×10^{-3}	6.106×10^{-3}	1.016
443.2	6.567×10^{-3}	6.553×10^{-3}	1.002
490.5	6.567×10^{-3}	6.555×10^{-3}	1.002
509.2	6.409×10^{-3}	6.541×10^{-3}	0.980
555.5	6.828×10^{-3}	6.910×10^{-3}	0.988
665.6	6.737×10^{-3}	6.695×10^{-3}	1.006
683.8	6.619×10^{-3}	6.632×10^{-3}	0.998

Table 37. NIST calibration factors for PWI compared to the values from PML.

λ [nm]	F_{PML} [μW cm^{-2} nm^{-1} count^{-1}]	F_{NL} [μW cm^{-2} nm^{-1} count^{-1}]	F_{PML}:F_{NL}
412.3	4.384×10^{-3}	4.422×10^{-3}	0.992
442.4	4.884×10^{-3}	4.951×10^{-3}	0.987
490.1	4.911×10^{-3}	5.040×10^{-3}	0.974
509.9	4.800×10^{-3}	4.963×10^{-3}	0.968
555.6	4.341×10^{-3}	4.420×10^{-3}	0.982
670.4	4.490×10^{-3}	4.462×10^{-3}	1.007
700.1	5.337×10^{-3}	5.618×10^{-3}	0.950

Table 38. NIST calibration factors for UWI compared to the values from Satlantic.

λ [nm]	F_S [μW cm^{-2} nm^{-1} count^{-1}]	F_{NL} [μW cm^{-2} nm^{-1} count^{-1}]	F_S:F_{NL}
411.3	1.002×10^{-3}	9.890×10^{-4}	1.013
443	1.052×10^{-3}	1.044×10^{-3}	1.008
489.6	1.074×10^{-3}	1.085×10^{-3}	0.989
509.5	1.142×10^{-3}	1.169×10^{-3}	0.977
554.7	1.158×10^{-3}	1.170×10^{-3}	0.989
590.1	1.124×10^{-3}	1.111×10^{-3}	1.011
665.6	1.122×10^{-3}	1.122×10^{-3}	1.000

Table 39. NIST calibration factors for UWE compared to the values from Satlantic.

λ [nm]	F_S [μW cm^{-2} nm^{-1} count^{-1}]	F_{NL} [μW cm^{-2} nm^{-1} count^{-1}]	F_S:F_{NL}
411.3	6.284×10^{-3}	6.223×10^{-3}	1.010
442.5	6.531×10^{-3}	6.499×10^{-3}	1.005
490.2	5.962×10^{-3}	6.032×10^{-3}	0.988
509.6	6.884×10^{-3}	7.040×10^{-3}	0.978
555.2	6.497×10^{-3}	6.559×10^{-3}	0.991
589.6	6.872×10^{-3}	6.808×10^{-3}	1.009
665	6.897×10^{-3}	6.914×10^{-3}	0.998

Table 40. NIST calibration factors for JWI compared to the values from JRC.

λ [nm]	F_{JRC} [μW cm^{-2} nm^{-1} count^{-1}]	F_{NL} [μW cm^{-2} nm^{-1} count^{-1}]	F_{JRC}:F_{NL}
412.4	5.94×10^{-3}	5.981×10^{-3}	0.993
443.5	6.29×10^{-3}	6.305×10^{-3}	0.998
490.6	6.26×10^{-3}	6.345×10^{-3}	0.987
509.1	6.60×10^{-3}	6.713×10^{-3}	0.983
555.9	6.84×10^{-3}	6.824×10^{-3}	1.002
665.4	6.97×10^{-3}	6.800×10^{-3}	1.025
682.1	6.68×10^{-3}	6.623×10^{-3}	1.009

Table 41. NIST calibration factors for GAI compared to the values from Satlantic.

λ [nm]	F_{S} [μW cm^{-2} nm^{-1} count^{-1}]	F_{NL} [μW cm^{-2} nm^{-1} count^{-1}]	F_{S}:F_{NL}
411.3	8.313×10^{-3}	8.182×10^{-3}	1.016
442.3	9.848×10^{-3}	9.825×10^{-3}	1.002
490.5	9.909×10^{-3}	9.972×10^{-3}	0.994
509.2	9.093×10^{-3}	9.255×10^{-3}	0.982
555	9.970×10^{-3}	1.010×10^{-2}	0.987
664.8	9.829×10^{-3}	9.803×10^{-3}	1.003
682.6	9.224×10^{-3}	9.180×10^{-3}	1.005

Table 42. NIST calibration factors for UAI compared to the values from Satlantic.

λ [nm]	F_{S} [μW cm^{-2} nm^{-1} count^{-1}]	F_{NL} [μW cm^{-2} nm^{-1} count^{-1}]	F_{S}:F_{NL}
411.2	9.034×10^{-3}	1.006×10^{-2}	0.898
442.8	9.758×10^{-3}	1.094×10^{-2}	0.892
489.6	9.649×10^{-3}	1.102×10^{-2}	0.876
509.5	9.205×10^{-3}	1.055×10^{-2}	0.873
555.3	9.190×10^{-3}	1.034×10^{-2}	0.889
589	9.147×10^{-3}	1.012×10^{-2}	0.904
665.5	9.284×10^{-3}	1.038×10^{-2}	0.894

Table 43. NIST calibration factors for SAE compared to the values from Satlantic.

λ [nm]	F_{S} [μW cm^{-2} nm^{-1} count^{-1}]	F_{NL} [μW cm^{-2} nm^{-1} count^{-1}]	F_{S}:F_{NL}
411.1	9.729×10^{-3}	9.761×10^{-3}	0.997
442.4	9.057×10^{-3}	9.176×10^{-3}	0.987
489.8	9.391×10^{-3}	9.722×10^{-3}	0.966
509.7	9.576×10^{-3}	1.003×10^{-2}	0.955
554.1	8.766×10^{-3}	9.028×10^{-3}	0.971
665.4	9.734×10^{-3}	9.717×10^{-3}	1.002
779.2	8.966×10^{-3}	9.035×10^{-3}	0.992

Table 44. NIST calibration factors for GWE compared to the values from Satlantic.

λ [nm]	F_S [μW cm^{-2} nm^{-1} count^{-1}]	F_{NL} [μW cm^{-2} nm^{-1} count^{-1}]	F_S:F_{NL}
411.5	6.33×10^{-3}	—	—
442.5	6.40×10^{-3}	6.513×10^{-3}	0.983
489.3	6.29×10^{-3}	6.355×10^{-3}	0.990
509.6	6.61×10^{-3}	6.889×10^{-3}	0.960
555.2	6.79×10^{-3}	7.064×10^{-3}	0.961
664.9	6.54×10^{-3}	6.565×10^{-3}	0.996
683.5	7.12×10^{-3}	7.185×10^{-3}	0.991

Table 45. NIST calibration factors for GWR compared to the values from Satlantic.

λ [nm]	F_S [μW cm^{-2} nm^{-1} count^{-1}]	F_{NL} [μW cm^{-2} nm^{-1} count^{-1}]	F_S:F_{NL}
411.1	4.963×10^{-4}	5.245×10^{-4}	0.946
443.6	5.143×10^{-4}	5.355×10^{-4}	0.960
489.5	5.781×10^{-4}	5.994×10^{-4}	0.964
509.2	5.440×10^{-4}	5.605×10^{-4}	0.971
555.4	5.623×10^{-4}	5.883×10^{-4}	0.956
665.7	5.892×10^{-4}	6.127×10^{-4}	0.962
683.2	5.116×10^{-4}	5.305×10^{-4}	0.964

Table 46. NIST calibration factors for SWQ compared to the values from JRC.

λ [nm]	F_{JRC} [μW cm^{-2} nm^{-1} count^{-1}]	F_{NL} [μW cm^{-2} nm^{-1} count^{-1}]	F_{JRC}:F_{NL}
411.1	9.30×10^{-5}	9.827×10^{-5}	0.946
442.9	8.93×10^{-5}	9.247×10^{-5}	0.966
489.9	9.05×10^{-5}	9.285×10^{-5}	0.975
509.7	5.69×10^{-5}	5.819×10^{-5}	0.978
555	5.39×10^{-5}	5.468×10^{-5}	0.986
665.5	3.60×10^{-5}	3.711×10^{-5}	0.970
683.7	3.77×10^{-5}	3.819×10^{-5}	0.987

Table 47. NIST calibration factors for PWR compared to the values from PML.

λ [nm]	F_{PML} [μW cm^{-2} nm^{-1} count^{-1}]	F_{NL} [μW cm^{-2} nm^{-1} count^{-1}]	F_{PML}:F_{NL}
411.9	1.186×10^{-4}	1.400×10^{-4}	0.847
442.5	8.602×10^{-5}	8.542×10^{-5}	1.007
489.9	5.602×10^{-5}	5.698×10^{-5}	0.983
509.7	5.708×10^{-5}	5.697×10^{-5}	1.002
555.4	5.069×10^{-5}	5.162×10^{-5}	0.982
669.8	3.564×10^{-5}	3.620×10^{-5}	0.985
682.5	3.630×10^{-5}	3.636×10^{-5}	0.998

Table 48. NIST calibration factors for UWR compared to the values from Satlantic.

λ [nm]	F_S [μW cm^{-2} nm^{-1} count^{-1}]	F_{NL} [μW cm^{-2} nm^{-1} count^{-1}]	F_S:F_{NL}
411.2	8.953×10^{-5}	9.373×10^{-5}	0.955
442.7	9.194×10^{-5}	9.650×10^{-5}	0.953
489.4	8.441×10^{-5}	8.795×10^{-5}	0.960
509.6	9.168×10^{-5}	9.451×10^{-5}	0.970
555.2	8.945×10^{-5}	9.105×10^{-5}	0.982
589.7	8.285×10^{-5}	8.417×10^{-5}	0.984
665.7	5.531×10^{-5}	5.697×10^{-5}	0.971

Table 49. NIST calibration factors for JWR compared to the values from JRC.

λ [nm]	F_{JRC} [μW cm^{-2} nm^{-1} count^{-1}]	F_{NL} [μW cm^{-2} nm^{-1} count^{-1}]	F_{JRC}:F_{NL}
412.4	1.837×10^{-4}	1.913×10^{-4}	0.960
443.5	1.650×10^{-4}	1.680×10^{-4}	0.982
490.6	1.686×10^{-4}	1.721×10^{-4}	0.980
509.1	1.891×10^{-4}	1.923×10^{-4}	0.983
555.9	1.788×10^{-4}	1.859×10^{-4}	0.962
665.4	9.730×10^{-5}	1.002×10^{-4}	0.971
682.1	1.282×10^{-4}	1.325×10^{-4}	0.967

0.993±0.011. The 412 nm channel was known to be degrading at the rate of about 5% per month (G. Moore, pers. comm.).

The UWR sensor was calibrated by Satlantic on 12 June 1996. The calibration factors F_S are given in Table 48. The mean ratio F_S:F_{NL} is equal to 0.968±0.013 with a maximum disparity of −4.7%. The JWR sensor was calibrated by JRC on 15 July 1996, and the calibration factors F_{JRC} are given in Table 49. The mean ratio F_{JRC}:F_{NL} is equal to 0.972±0.010 with a maximum disparity of −4.0%.

7.3.2 SAS-II System

The NIST calibration factors for the GAE and GAR sensors were determined twice during SIRREX-5; the factors are given in Tables 50 and 51, respectively. The raw data were analyzed following procedures similar to those outlined earlier. The tables state the measurement wavelength, the calibration factor supplied by the owner of the radiometer, the NIST calibration factor, and the ratio of the calibration factors.

The GAE sensor was calibrated by Satlantic on 20 December 1995. The calibration factors F_S are given in Table 50. The mean ratio F_S:F_{NL} is equal to 0.978±0.025 with a maximum disparity of −7.0%. The GAR radiance sensor was calibrated by Satlantic on 5 February 1996; the calibration factors F_S are given in Table 51. The mean ratio F_S:F_{NL} is equal to 0.982±0.013 with a maximum disparity of −4.0%.

7.3.3 BSI Radiometers

The NIST calibration factors for the PRV-600 and PRV-610 radiometers CAI, CWI, and CWR were determined after SIRREX-5 using F332; the Spectralon plaque was used with the lamp to calibrate CWR. The factors for CAI and CWI are given in Tables 52 and 53. The results for CWR are not reported because there were problems with the results which are not understood—the results for a few channels are satisfactory, but other channels disagree with the expected values by greater than a factor of 2. The raw data were analyzed following procedures similar to those outlined in the earlier sections. The tables state the measurement wavelength, the calibration factor supplied by the owner of the radiometer, the NIST calibration factor, and the ratio of the calibration factors. None of the broadband PAR channels could be calibrated at NIST, because there was no information on the relative spectral responsivities.

The calibration factors supplied by the instrument owner and originating with BSI, F_{BSI}, for sensor CAI are given in Table 52. The mean ratio F_{BSI}:F_{NL} is equal to 0.982±0.005 with a maximum disparity of −2.8%. The calibration factors, F_{BSI}, for sensor CWI are given in Table 53. The mean ratio F_{BSI}:F_{NL} is equal to 0.973±0.004 with a maximum disparity of −3.6%.

7.3.4 ASD Spectrometers

The accuracy of the wavelength calibration of the PS2-903 spectrometers is shown in Fig. 32a as the difference in

Table 50. NIST calibration factors for GAE (part of the SAS-II) compared to the values from Satlantic.

λ [nm]	F_S [μW cm^{-2} nm^{-1} count^{-1}]	F_{NL} [μW cm^{-2} nm^{-1} count^{-1}]	F_S:F_{NL}
412.6	9.274×10^{-3}	9.356×10^{-3}	0.991
442.2	8.957×10^{-3}	8.953×10^{-3}	1.000
490.2	9.185×10^{-3}	9.255×10^{-3}	0.992
510.5	8.338×10^{-3}	8.967×10^{-3}	0.930
554.6	8.855×10^{-3}	9.223×10^{-3}	0.960
668.9	9.127×10^{-3}	9.253×10^{-3}	0.986
683.5	9.343×10^{-3}	9.485×10^{-3}	0.985

Table 51. NIST calibration factors for GAR (part of the SAS-II) compared to the values from Satlantic.

λ [nm]	F_S [μW cm^{-2} nm^{-1} count^{-1}]	F_{NL} [μW cm^{-2} nm^{-1} count^{-1}]	F_S:F_{NL}
412.6	6.281×10^{-4}	6.383×10^{-4}	0.984
442.2	6.081×10^{-4}	6.158×10^{-4}	0.987
490.3	6.071×10^{-4}	6.141×10^{-4}	0.989
510.3	5.987×10^{-4}	6.237×10^{-4}	0.960
554.6	6.108×10^{-4}	6.281×10^{-4}	0.972
668.9	3.012×10^{-4}	3.064×10^{-4}	0.983
682.7	3.072×10^{-4}	3.068×10^{-4}	1.001

Table 52. NIST calibration factors for CAI compared to the values provided by the instrument owner.

λ [nm]	F_{BSI} [μW cm^{-2} nm^{-1} count^{-1}]	F_{NL} [μW cm^{-2} nm^{-1} count^{-1}]	F_{BSI}:F_{NL}
380	−30.38	−30.94	0.982
412	−30.58	−31.46	0.972
443	−29.24	−29.78	0.982
490	−29.92	−30.43	0.983
510	−30.15	−30.61	0.985
555	−30.59	−31.01	0.986

Table 53. NIST calibration factors for CWI compared to the values provided by the instrument owner.

λ [nm]	F_{BSI} [μW cm^{-2} nm^{-1} count^{-1}]	F_{NL} [μW cm^{-2} nm^{-1} count^{-1}]	F_{BSI}:F_{NL}
380	−76.49	−78.63	0.973
412	−30.89	−32.04	0.964
443	−30.57	−31.44	0.972
490	−29.38	−30.16	0.974
510	−30.34	−31.12	0.975
555	−30.13	−30.82	0.978

the measured centroid of the emission line and the actual wavelength of the transition. The peak wavelengths were determined using a commercial software package, Peakfit, with gaussian peak shapes. The peak positions were also determined using centroid calculations, but the two methods were in agreement. The results for the two spectrometers (SAI and SAR) are plotted using different symbols. The HeNe laser was also used to determine the stray light in the PS2-903 spectrometers. Figure 32b shows that the stray light rejection is on the order of 10^{-3}. The features at about 300 nm and 900 nm are not reproducible. They may be an artifact of the PS2-903 analysis software or the result of saturation at the HeNe wavelength.

Figure 33a illustrates the results of the NIST calibration of the SAI and SAR spectrometers. The calibration coefficients supplied by the instrument owner are normalized using the NIST calibration coefficients. For wavelengths above 420 nm, the differences are up to 20%. Below about 400 nm, the signal-to-noise ratios were inadequate for analysis. Figure 33b gives the standard deviations for the calibration of the SAR instrument. For both the SAI and the SAR, the discrepancy of up to 20% is larger than that observed for the other instruments which were calibrated by NIST at SIRREX-5.

7.4 Discussion of NIST Calibrations

7.4.1 Irradiance

The results for the irradiance-measuring filter radiometers are summarized in Fig. 34. An examination of the ratios of the manufacturer's calibration factors over the NIST values reveals that the average over wavelength of the ratios for the irradiance sensors are distributed about 0.988, with a standard deviation of 0.017. For this calculation, sensor UAI was not included; the Satlantic values for F_S are about 10% smaller than the NIST values; the source of the discrepancy is unknown.

As a function of wavelength, the ratio $F{:}F_{NL}$ is generally a minimum at the 509 nm channel, which could imply a problem with the NIST scale or method. In the irradiance calibration measurements, the shortest wavelength channel was placed at the highest vertical position, and the 509 nm channel was at the lowest vertical position. This decrease at 509 nm for the Satlantic sensors could be caused by the goniometric distribution of irradiance from lamp F332. The wavelength dependence, however, could also be compounded by the fact that the lamp used by Satlantic for the irradiance calibration could also have an angle-dependent irradiance pattern.

As a function of channel number in the Satlantic sensors, the standard deviation of the ratios $F{:}F_{NL}$ is given in Table 54. The results for UAI and channel 7 of PWI were excluded. The smallest total uncertainty is measured for channel 7, similar to that found for the field calibrator. It is the only channel aligned with the optical axis of the lamp.

Table 54. The relative standard deviations of the ratios $F{:}F_{NL}$ for the irradiance sensors as a function of channel number.

Channel No.	σ' [%]
1	1.08
2	0.85
3	1.20
4	1.01
5	0.94
6	0.78
7	0.57

7.4.2 Radiance

The corresponding ratios for the radiance sensors are mostly below 1 (Fig. 35). The average and standard deviation (excluding all of the CWR results, and channel 1 of PWR) is 0.974±0.015. One reason for the discrepancy could be the value used for the plaque reflectance factor in (16). Most calibrations by the manufacturers are done with the calibrated irradiance lamp incident at 0° on the plaque while the sensor views the plaque at a 45° angle. The plaque manufacturer, however, usually only provides the reflectance factor for the light incident at 8° and collected over the entire hemisphere.

A comparison of the $R(8°/h)$ and the $R(0°/45°)$ for the small plaque (25.4 cm, square, Spectralon) done as a part of SIRREX-4, showed that the ratio of the 0°/45° reflectance factor over the 8°/h was not 1.0, but ranged from 1.029 at 400 nm, to 1.026 at 633 nm (Johnson et al. 1996). The BRDF and $R(6°/h)$ for this same plaque were measured by NIST in June 1997, September 1997, and May 1998. Data were obtained at three wavelengths: 400, 632.8, and 770 nm. The BRDF measurements were limited to 0° incident angle and −70° to +70° view angle, with an increment of 10°. No temporal trend was evident, so these data for the three dates were averaged. A fourth order polynomial in the view angle was used to determine $R(0°/45°)$. In good agreement with the SIRREX-4 data, the average ratio $R(0°/45°){:}R(6°/45°)$ for these more recent results is 1.025 at 400 nm, and 1.028 at 633 and 770 nm.

The large plaque was used for the radiance calibrations in SIRREX-5; there are no NIST measurements of the BRDF or $R(6°/h)$. Based on the measurements of the small plaque, a single value of $R(0°/45°){:}R(8°/h) = 1.0275$ was used for the reflectance factor ratio at all wavelengths. Thus, if $R(8°/h)$ values were used instead, as are done during the calibrations at the home institutions, then the radiance calibration factors would be smaller by 2.75%; this is in agreement with the observed average discrepancy of −3%.

7.4.3 SXR Studies

The independent measurements of the spectral radiance of the large plaque using the SXR are compared to

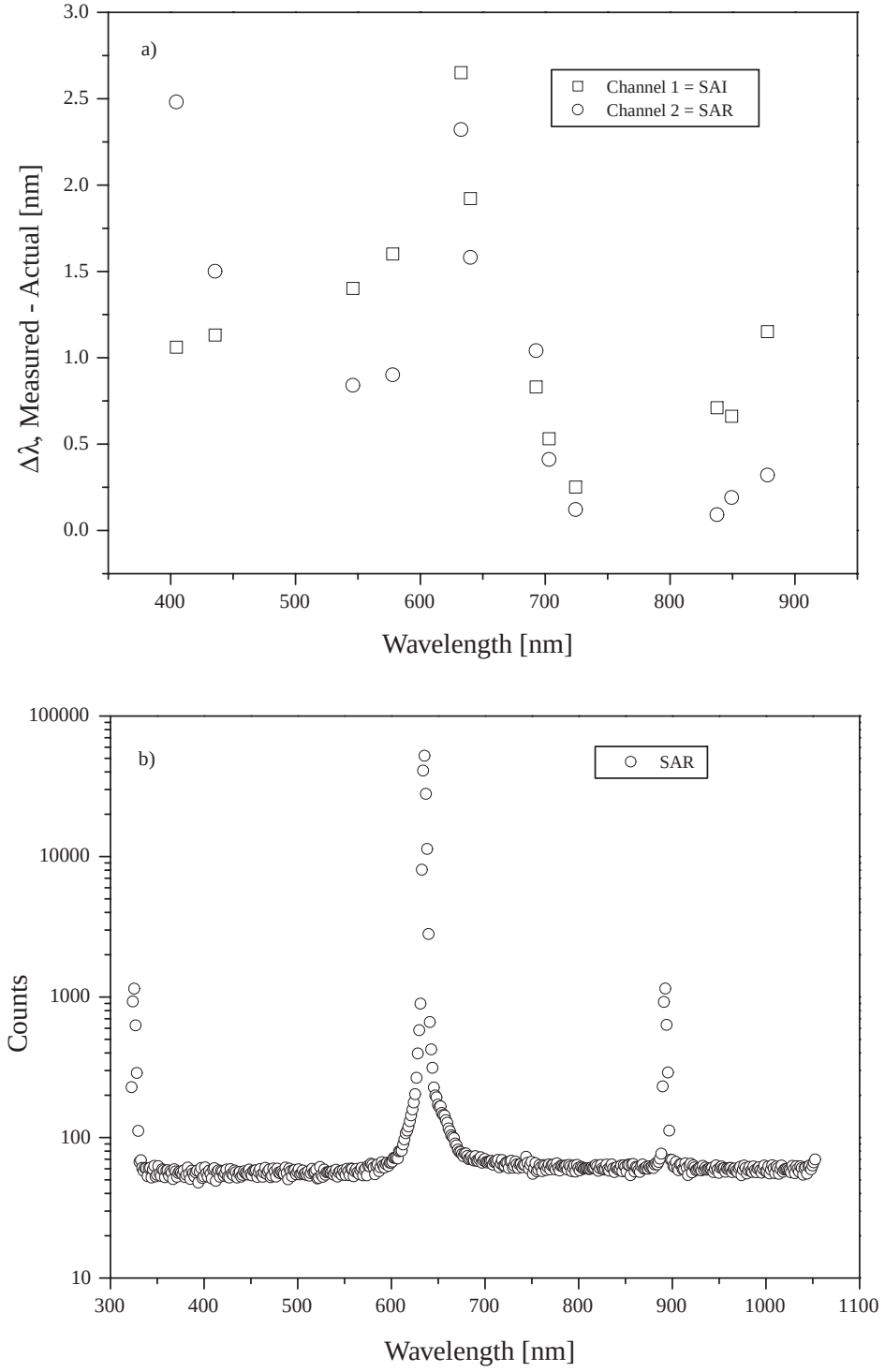

Fig. 32. Results of studies of the wavelength calibration and stray light of the PS2-903 system: **a)** wavelength accuracy of the SAI and SAR spectrometers as determined from measurements of line sources with known transitions and a HeNe laser; and **b)** the output, in counts, of the SAR instrument from measurements of a HeNe laser.

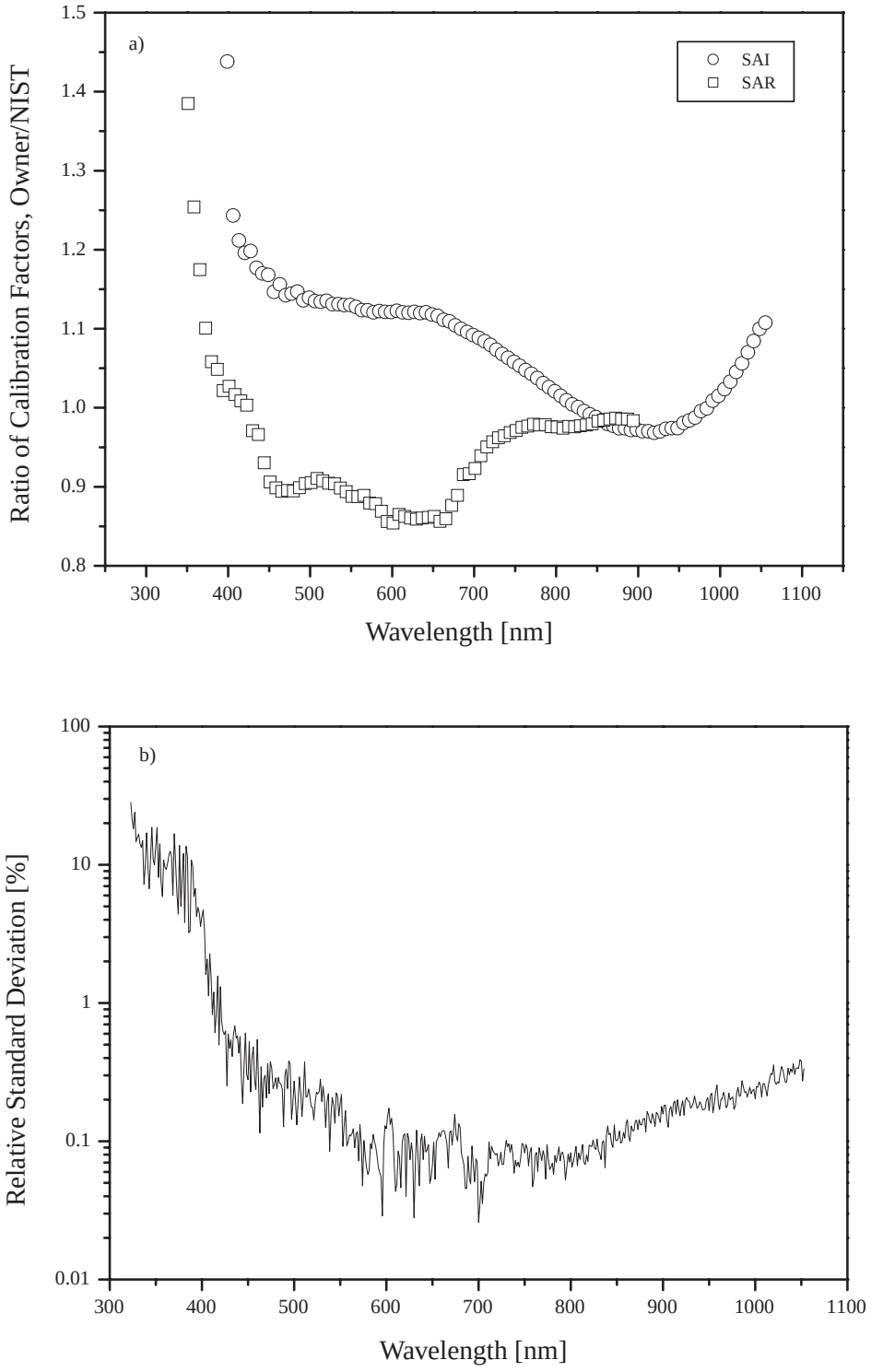

Fig. 33. Results of the radiometric calibration of the PS2-903 system. **a)** Comparison of the calibration factors for the SAI and the SAR for the values supplied by the owner and the values determined by NIST during SIRREX-5. The two sensors are identified in the legend. **b)** Relative standard deviations as a function of wavelength for the calibration scans for SAI.

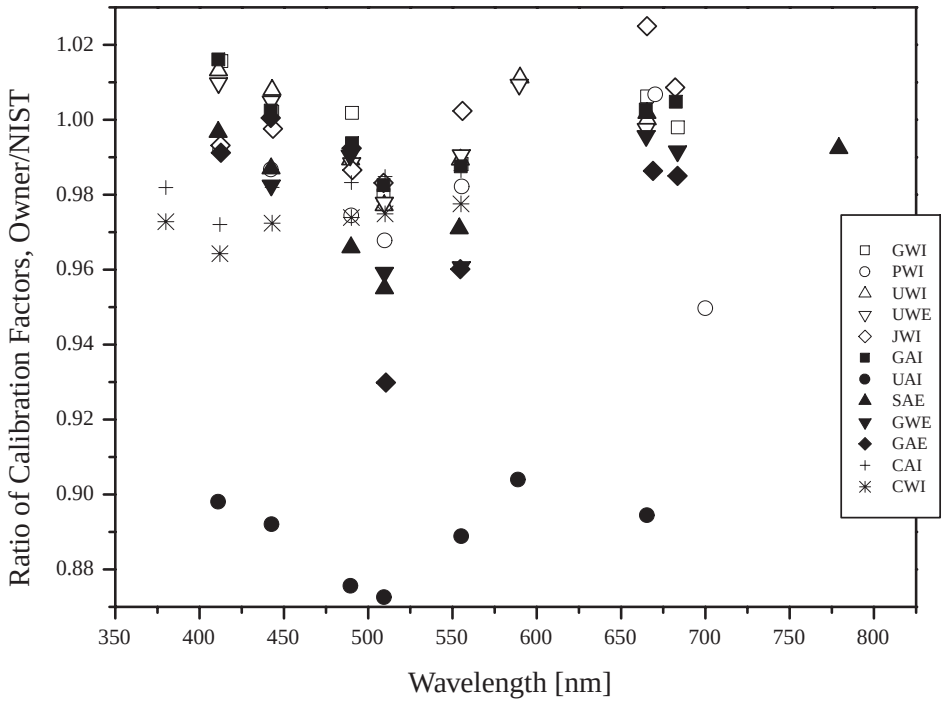

Fig. 34. The calibration factors for the filter radiometers supplied by the owners of these irradiance sensors normalized by the calibration factors determined at NIST during SIRREX-5. This ratio is plotted as a function of the sensor's measurement wavelength.

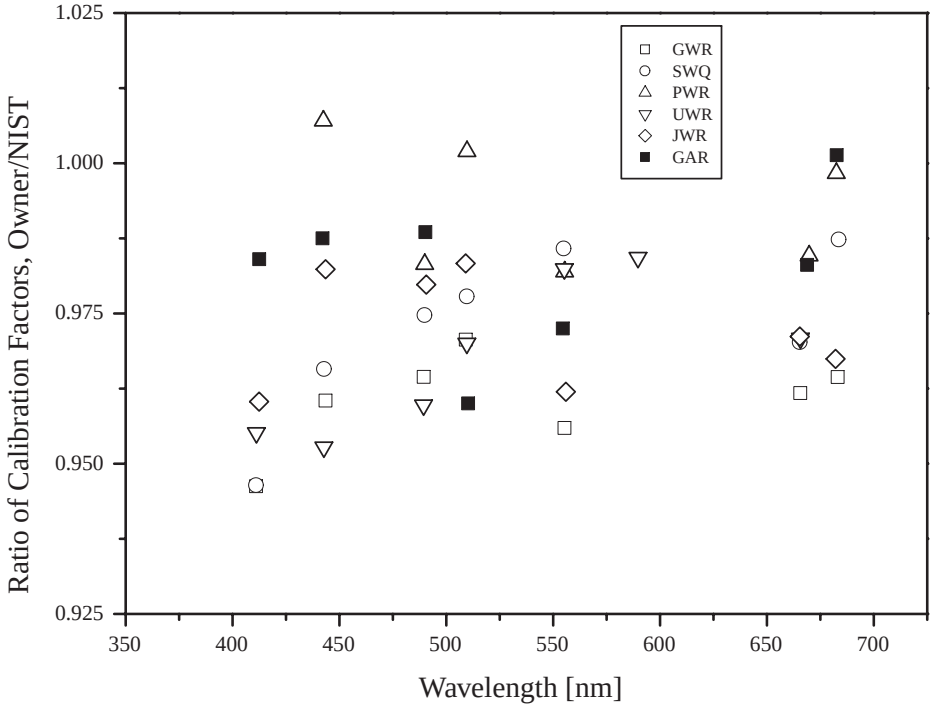

Fig. 35. The calibration factors for the filter radiometers supplied by the owners of these radiance sensors normalized by the calibration factors determined at NIST during SIRREX-5. This ratio is plotted as a function of the sensor's measurement wavelength.

the spectral radiance predicted from (16) in Figs. 23b, 26b, and 27b. Unlike the OCR-200s, the SXR views the same target area for each channel, with common input optics. A comparison of the average value for $H'(\lambda)$ at the four measurement wavelengths closest to those in the OCR-200 sensors, is given in Table 55 for GWR, UWR, and GAR. The results are in agreement, although the SXR values are in better agreement with the calculated values. The SXR Type A uncertainty is negligible, while the OCR-200 Type A uncertainty is about 1%.

Table 55. Direct comparison of the SXR and OCR-200 measurements of the illuminated plaque for common measurement wavelengths.

λ	$H'(\lambda)$		$H(\lambda)$	
[nm]	*Average*	σ	*Average*	σ
412	0.979	0.0008	0.962	0.020
442	0.973	0.0009	0.967	0.018
490	0.988	0.0004	0.971	0.015
665	0.987	0.0003	0.973	0.011

On 31 July, the SXR was used to measure the small and large plaques as an additional test of the practice of estimating the plaque radiance from $R(8°/\mathrm{h})$ data. According to (16), the predicted radiance is proportional to $R(0°/45°, \lambda)$; in this work, this bidirectional reflectance factor is assumed to be proportional to $R(8°/\mathrm{h}, \lambda)$. The ratio of the spectral radiances as measured by the SXR for equivalent illumination conditions of the two plaques should, therefore, be equal to the ratio of the $R(8°/\mathrm{h}, \lambda)$ factors.

The values for $R(8°/\mathrm{h}, \lambda)$, as supplied by Labsphere for both plaques, are shown in Fig. 36. The small plaque was calibrated at Labsphere on 29 August 1994 and the large plaque on 30 December 1995. Also shown, for the small plaque, are the average of the NIST measurements for $R(6°/\mathrm{h}, \lambda)$ in June 1997, October 1997, and May 1998. For the NIST data, the vertical lines represent the standard deviation of the three measurements. The independent determinations are in agreement given the combined uncertainty of the measurement.

The $R(8°/\mathrm{h}, \lambda)$ data in Fig. 36 indicates that the radiance from the small plaque should be slightly larger (about 0.3% from 400–800 nm) than the large plaque; in fact, the opposite is observed. Figure 37 is the ratio of the radiance measured by the SXR for the two plaques, with the large plaque results normalized by the small plaque results. The average ratio is about 1.013, implying a discrepancy of about 1.6% based on the reflectance values from Labsphere. The statistical uncertainties in the SXR measurements are less than 0.1% (Table 30). Labsphere states that the random uncertainty in the $R(8°/\mathrm{h}, \lambda)$ values is 0.005, but an estimate for the total uncertainty is not given. Differences in the lamp-to-plaque distance for the two plaques could account for part of the discrepancy. From (16), a difference of 0.5 cm at 122.4 cm corresponds to a relative change in radiance of 0.8%. Interreflections between the illuminated plaque and the surrounding black cloth may depend on the size of the illuminated plaque, resulting in different values for the radiance. The fraction of scattered light, as measured using the on-axis obscuration, however, did not depend on the size of the plaque. The scattered radiance was about 0.5% of the total radiance for SXR channels 1–5; for channel 6 at 775 nm, this value was 4%.

7.4.4 SXR vs. Actual BRDF

Finally, the SXR measurements of the small plaque on 31 July 1996 are compared to the radiance calculated using the average of the NIST BRDF values for $R(0°/45°, \lambda)$. As explained above, NIST measured the BRDF of the small plaque in 1997 and 1998; these data are in agreement with the 1995 data reported in the SIRREX-4 document (Johnson et al. 1996). To determine $R(0°/45°, \lambda)$ at the SXR wavelengths, the 1997 and 1998 data at the three measurement wavelengths were averaged and then fit to a fourth order polynomial to find the value at $\theta' = 45°$. Then these bidirectional reflectance factors were fit to a second order polynomial as a function of wavelength, to determine the reflectance at the SXR wavelengths. These values were used in (16) to determine the $L_C(\lambda)$. A comparison to the radiance measured by the SXR is given in Fig. 38. The ratio of the measured to the calculated values, which is the quantity plotted, indicates the agreement is between −2.8% and +1.7%. The overall trend is the same as that observed with the large plaque (compare Fig. 38 to Figs. 23b, 26b, or 27b).

8. DISCUSSION

The discussion and recommendations that result from SIRREX-5 fall into two categories: 1) general statements about this type of activity; and 2) conclusions inferred from the specific experiments.

8.1 General Statements

8.1.1 Planning

SIRREX-5 required a tremendous amount of planning, extensive efforts to prepare and restore the laboratories and their sites, additional time for the calibration of the optical sensors, and a large effort to reduce and analyze the data collected. This latter activity took place after SIRREX-5. In short, SIRREX-5 was a resource-intensive activity. Of the multiple SIRREX objectives, SIRREX-5 concentrated on intercomparing field radiometers, confirming the calibration coefficients and radiometric stability from the NIST laboratory to the outdoors, and demonstrating proper measurement practice and protocol implementation. The exchange of information that took place

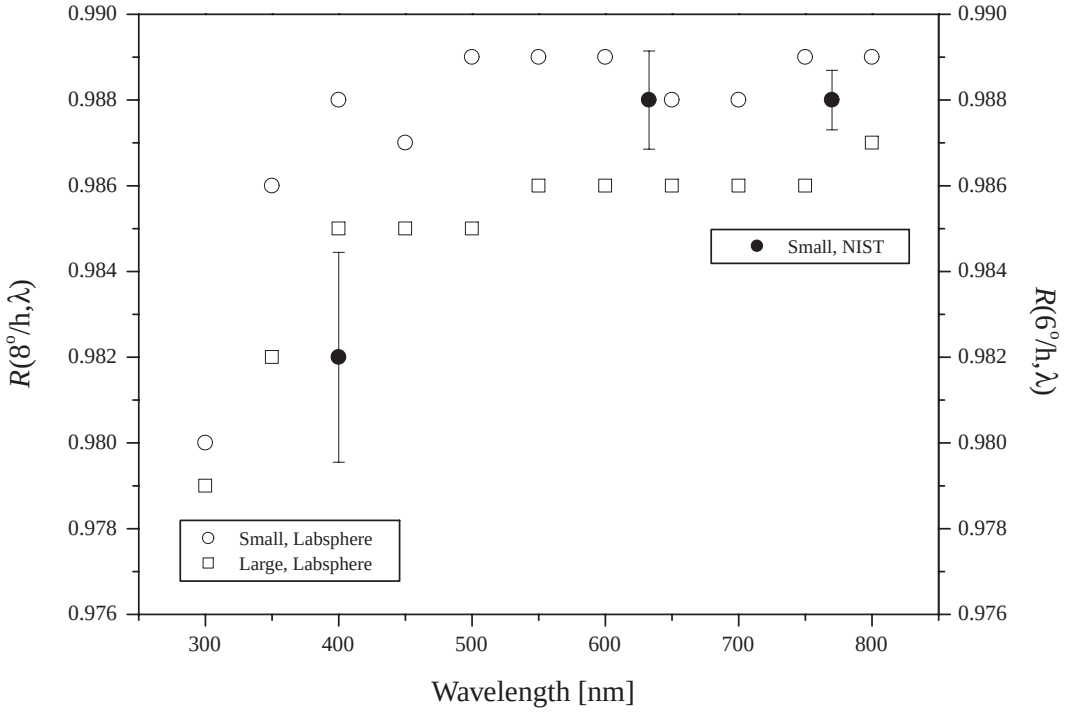

Fig. 36. The Labsphere values for $R(8°/\mathrm{h}, \lambda)$ for the large and the small NIST Spectralon plaques, and the average NIST measurements for $R(6°/\mathrm{h}, \lambda)$.

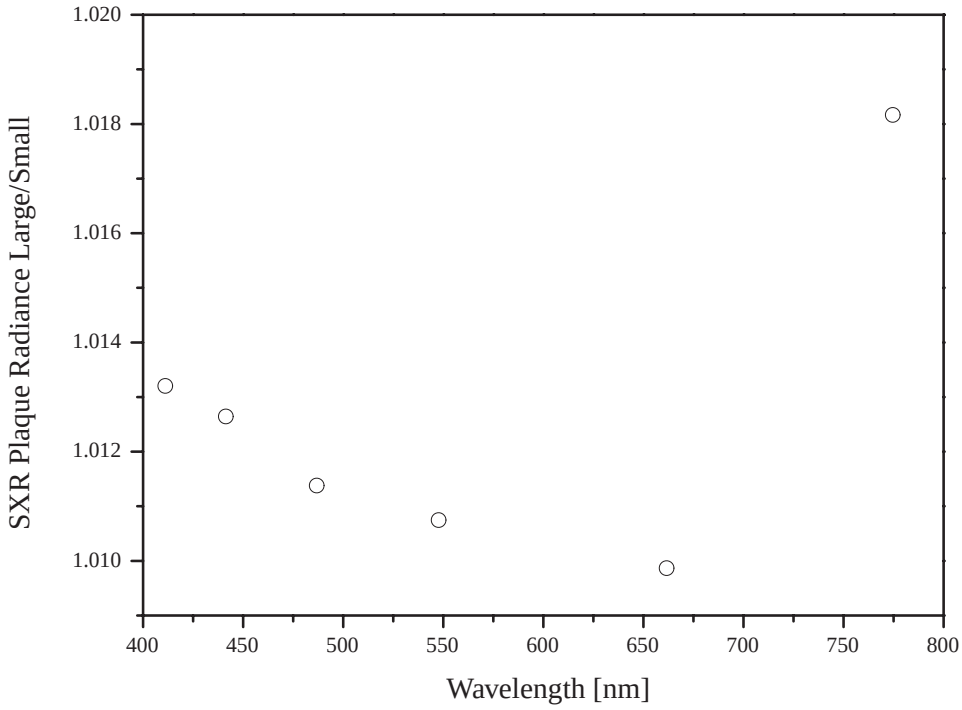

Fig. 37. SXR measurements of the illuminated plaques, plotted as the results for the large plaque normalized by the results for the small plaque. The measurements were made on 31 July.

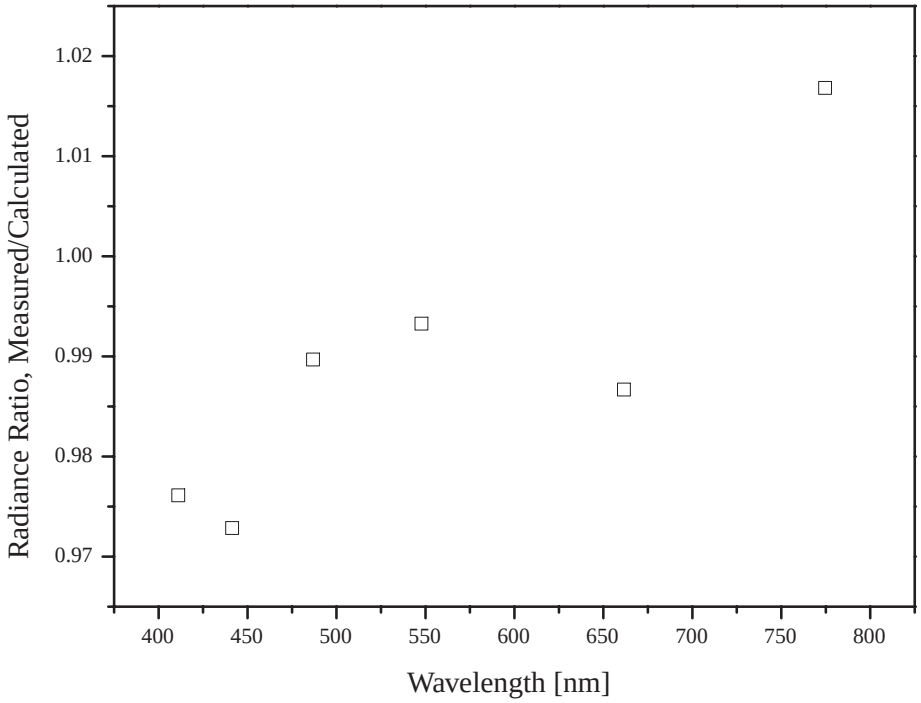

Fig. 38. SXR radiance measurements of the small plaque, normalized by the radiance predicted from the plaque BRDF and the irradiance of the standard lamp.

during the morning talks was an additional feature. The participants fell into two categories: 1) those who were intensively engaged in executing the experiments, often with equipment with which they were familiar; and 2) those who were there to learn, with no direct role in planning or executing SIRREX-5.

This combination of controlled intercomparisons and a workshop, or training, atmosphere was difficult to implement. The workshop atmosphere and open enrollment led to a large number of participants; the training objective meant that the groups should be kept small, which led to a large number of groups. Identifying appropriate activities for all groups, with adequate leadership and facilities, required a large number of personnel. For example, there were no free key personnel available to troubleshoot the various SIRREX-5 laboratories; in several cases this would have been beneficial. It is recommended that in the future the intercomparison and training objectives be made separate, perhaps in the form of two sequential activities.

Failure to plan adequately for the thorough reduction, analysis, and documentation of the results of SIRREX-5 was an oversight. Resources are required for these activities, so an additional recommendation is that future activities of this nature include the production of a preliminary draft after executing the experiments. This would approximately double the length of time for the overall activity.

8.1.2 Data Acquisition

Data acquisition and analysis software and procedures (including data stream merging) should be completed and fully tested prior to the experiment. A set of minimum requirements for data acquisition software should be developed and included in the next revision of the SOOP. Some experiments produced inappropriate, inconsistent, or invalid measurements which could have been avoided if the data, or some subset of the data, were displayed in real time, independent of the status of the file archiving procedures. The serial number of the optical sensor head should be recorded in the data file. Information on the A/D unit is not adequate in cases where the A/D unit can be operated with different optical units. In addition, the serial number should be read electronically by the data acquisition software, so that it is not the responsibility of the operator to enter the correct value into the computer program during the instrument initialization. The calibration data files, analyzed in Sect. 7, for the most part did not contain any information on the instrument identification. Proper interpretation of all of the SIRREX-5 calibration data, with respect to the 23 instruments calibrated, is completely dependent on the accuracy of the filename and the comments recorded in the laboratory notebooks.

8.1.3 Rapid Results

Profile data for the in-water measurements should be analyzed and presented within one hour of completing a profile measurement. This capability would allow anomalies (e.g., excessive pitch or roll angles for the in-water measurements) to be detected in time to correct the cause. It would also be easier to make daily assessments of the inter-

comparison results, as was intended, but not realized, during SIRREX-5. The lack of suitable rapid results severely affected the NIST calibrations because of the failure of the data acquisition software during the pre-SIRREX laboratory radiance calibrations. In both cases, additional trained personnel, available at the time of measurement, would have been useful.

8.1.4 Calibration Coefficients

There was initial confusion at SIRREX-5 regarding calibration coefficients. Not all of the instrument owners could readily supply pre-SIRREX calibration coefficients to be applied to each instrument that participated in the measurements. It was the responsibility of each instrument's user or owner to provide these values, just as if the SIRREX represented an operational cruise.

8.2 Specific Experiment

8.2.1 *In Situ* Intercomparisons

The objective of the in-water laboratories (Lab I and Lab II) was to perform simultaneous *in situ* intercomparisons using radiometers in the same class. By excluding results obtained with variable lighting and with proper control of the platform stability and other parameters, field radiometers of the same overall design (OCR-200 or OCI-200) agreed within about 2%. This value is not significantly larger than the variation expected from the uncertainty in the calibration coefficients. In comparison, the field comparisons of the downwelling solar irradiance in the UV have identified discrepancies between simultaneous field measurements, given the expected calibration accuracy of the instruments (Early et al. 1998b and 1998c). However, the UV measurements incorporated instruments of various designs and calibration pathways. The expansion of the class of ocean color radiometers is a reasonable goal for future intercomparisons. A key result of the in-water laboratories is the significance of the platform stability. As discussed in Sect. 2.4, controlling the pitch and roll offsets is very important, and incorporating a comparison of the pressure sensors would probably be beneficial.

The in-air laboratories (Lab III and Lab IV) did not include simultaneous measurements with the same class of instruments—two different instrument designs were used sequentially. Instead of comparing radiance or irradiance, a derived quantity, R_{RS}, was compared using two methods for determining the downwelling irradiance. The separate measurements required to determine $E_s(0^+, \lambda)$ were sequential, but made rapidly in order to reduce the effect of variations in the lighting conditions. The procedures used in the field reasonably represented the procedures implemented by some researchers, as one objective of Labs III and IV was to identify potential sources of systematic error. The discrepancy between the values for R_{RS}, obtained using the two methods, is greater than the uncertainty desired for actual field measurements. This indicates that additional investigations would be beneficial, and the uncertainty obtained in the typical field experiment may be as large as 15%. For the method of using a diffusely reflectance standard for deriving the total downwelling irradiance, many issues were identified (Sect. 3.1). These must be addressed before this method can be used with confidence.

8.2.2 Instrument Stability

The results with the UV field irradiance calibrator (Lab V) demonstrated that the calibration coefficients for the selected subset of field radiometers could be duplicated, within a few percent, in the field. The result is significant because, as with the in-water experiments, the OCI-200 class of radiometers had never been tested in this manner: a direct comparison of absolute calibration coefficients for laboratory and field measurements.

The SQM, used in Lab VII, demonstrated a portable, stable source which was used to monitor the radiometric sensitivity of three field instruments. During SIRREX-5, the instruments were stable to within 1.5%, and the internal monitors in the SQM were stable to within 0.3%.

8.2.3 Calibration Coefficients

The calibration coefficients determined by NIST for the filter radiometers agreed with those provided with the instrument to within a few percent. This result is encouraging, because the instruments were calibrated by various laboratories. For the 11 irradiance sensors manufactured by Satlantic or BSI (excluding UAI), the average ratio of the stated calibration factors, normalized by the NIST values, is 0.988±0.017 (Fig. 34). For the six radiance sensors manufactured by Satlantic, the average of the similar ratio is 0.974±0.015 (Fig. 35). Sensor CWR from BSI was excluded from the average, because there appeared to be problems with its calibration at NIST. Channel 1 of sensor PWR was also excluded. The increased discrepancy from NIST for the radiance sensors compared to the irradiance sensors may be partially explained by the underlying assumptions on the reflectance of the diffuse target used in generating the scale of spectral radiance. Finally, the NIST calibration of the field radiometers was only partially successful, because of the failure of the data acquisition software during the pre-SIRREX calibration activities. The calibration coefficients for the OCR-200 series sensors, therefore, derive entirely from the plaque laboratory.

The NIST calibration of the PS2-903 system (SAI and SAR) disagreed with that provided by the instrument owner by an amount that is significant given the goals outlined in the SOOP (Mueller and Austin 1995). The average ratio, for the spectral interval from 400–1056 nm, of the stated SAI calibration factors normalized by the NIST values, is 1.07±0.07. Likewise, the average ratio, for the spectral interval from 400–900 nm, is 0.93±0.05 (Fig. 33a).

8.2.4 Overlooked Measurement Issues

For sensors with multiple, off-axis channels, the calibration coefficients were found to depend on the angular position of the individual channels; this was attributed to the nonpoint source behavior of FEL lamps. The accuracy of radiance and irradiance calibrations would be improved if care were taken to align the optical axis of the individual channels on the optical axis of the calibration source. For FEL lamps, NIST describes an alignment jig for this purpose (Walker et al. 1987). For illuminated plaques or integrating spheres, the optical axis is normal to, and centered in, the plane of the source. If it is not possible to align each optical axis separately, variations caused by the off-axis geometries and source uniformities should be averaged out by performing the calibrations at several angular orientations about the optical axis.

The plaque laboratory (Lab VI), as with the previous SIRREXs, demonstrated the problems associated with creating a source of calculable spectral radiance using a diffusely reflecting standard and a standard of spectral irradiance. The experimental arrangement in SIRREX-5 was superior to that used during SIRREX-4, because the geometry was determined more accurately (lamp distance and radiometer view angle) using calibrated motorized stages. The control of scattered light and the measurement of the ambient signal were also better. It was possible to investigate, in a more systematic way, the variation in the radiometer calibration coefficients with rotation about the sensor's optical axis. The variation in the plaque radiance with the lamp-to-plaque distance was also varied; however, the uncertainty in the reflectance of the plaque, the uniformity of the irradiance distribution on the plaque, and the correct reference plane for the $1/r^2$ correction of the lamp irradiance still have to be quantified. The agreement between the SXR and the predicted radiance and the discrepancy between the SXR measurements of two plaques of known $R(8°/\mathrm{h}, \lambda)$ indicate that the uncertainty in the spectral radiance is probably several percent.

The laboratory on selected topics was an attempt to address ancillary key issues, such as the irradiance uniformity on a plaque, the accuracy of the downwelling irradiance, and the utility and appropriateness of the SOOP. In hindsight, this was too ambitious, and Lab VIII probably should have concentrated on only one of these topics.

9. CONCLUSIONS

The stated objectives of SIRREX-5 were to intercompare various field radiometers, demonstrate proper measurement practice, and review and improve measurement protocols. In spite of the limitations and problems, which are identified in this document, the overall assessment of SIRREX-5 is favorable. Future activities should be limited to addressing a specific, limited set of these objectives, ideally under more realistic (e.g., clear ocean waters) measurement conditions.

Acknowledgments

The successful execution of SIRREX-5 was not possible without the assistance of many individuals. For arranging the site at Little Seneca Lake, the authors are grateful to Lester Straw, Deputy Director of Parks, Montgomery County Department of Parks, Silver Spring, Maryland; James McMahon, Park Manager, Black Hill Regional Park, Boyds, Maryland; and Jeff Asner, WSSC, Laurel, Maryland.

From NIST, Bob Saunders led two of the selected topics laboratories, and assisted with the data acquisition associated with these efforts. Ted Early provided valuable advice and assistance during the entire project, from the planning to the final manuscript. Yvonne Barnes measured the reflectance standards for directional/hemispherical and bidirectional reflectance factors. Charles Gibson performed the calibrations of the standard irradiance lamps. Tom Larason was responsible for the A/D calibrations. From NASA/GSFC, Chuck McClain assisted with the experiments and led the protocols sessions. Brian Schieber assisted with all aspects of data acquisition for the in-water experiments. Ron Carlson provided valuable logistical support during the planning and execution of SIRREX-5.

Jim Brown (UM) assisted with the data acquisition software for the Satlantic radiometers. Curtis Davis, Ajit Subramaniam, Sonia Gallegos, and Gregory Terrie lent equipment to SIRREX-5. Scott McLean lent equipment, assisted with the data acquistition software, and led some sessions of the Lab V. Giuseppe Zibordi and Gerald Moore lent equipment and assisted with the in-water experiments at Little Seneca Lake. Jim Ehramjian assisted with the data acquisition and execution of some of the SIRREX-5 Labs. Dennis Clark (NOAA) lent the single channel irradiance radiometer for Lab VIII. Many SIRREX-5 participants distinguished themselves by providing valuable and welcome assistance; in particular the authors wish to thank Jim Irish, Ajit Subramanian, John Morrow, Dave Menzies, and Hans Hakvoort. The participation of NIST in SIRREX-5 was made possible by NASA Interagency Agreement S-64096-E.

Appendix A

SIRREX-5 Participants

The attendees to SIRREX–5 are presented alphabetically with the contact information provided as of the time of SIRREX–5. The lecturers are identified and laboratory instructors are noted, as well as those individuals who participated in the laboratory sessions as active participants or observers.

Kohei Arai — *Group G*
Saga University
1 Honjo
Saga
JAPAN
Voice: 81–952–28–8650
Fax: 81–952–28–8650
Net: arai@is.saga_u.ac.jp

Edward Armstrong *Group G*
NOAA/Coastal Services Center
2224 S. Hobson Avenue
Charleston, SC 29405
USA
Voice: 803–974–6265
Fax: 803–974–6224
Net: armstrong@csc.noaa.gov

Robert Barnes *In-Air Data Reduction*
NASA/GSFC/SAIC General Sciences Corporation
Code 970.2
Greenbelt, MD 20771
USA
Voice: 301–286–0501
Fax: 301–286–0268
Net: rbarnes@calval.gsfc.nasa.gov

Yvonne Barnes *Lecturer*
NIST/Optical Technology Division
MS 8442
Gaithersburg, MD 20899
USA
Voice: 301–975–2345
Fax: 301–840–8551
Net: yvonne.barnes@nist.gov

John Brock *Group D*
NOAA/Coastal Services Center
2224 S. Hobson Avenue
Charleston, SC 29405
USA
Voice: 803–974–6239
Fax: 803–974–6224
Net: jbrock@csc.noaa.gov

Sally Bruce *Plaque Laboratory Instructor*
NIST/Optical Technology Division
MS 8441
Gaithersburg, MD 20899
USA
Voice: 301–975–2323
Fax: 301–869–5700
Net: sally.bruce@nist.gov

James Butler
NASA/GSFC
Code 920.1
Greenbelt, MD 20771
USA
Voice: 301–286–4606
Fax: 301–286–1616
Net: butler@ltpmail.gsfc.nasa.gov

Ronald Carlson *Logistical Support*
NASA/GSFC/Science Systems and Applications Inc.
Code 970.2
Greenbelt, MD 20771
USA
Voice: 301–286–0774
Fax: 301–286–1775
Net: ron@ardbeg.gsfc.nasa.gov

Brian Curtiss *Group C*
Analytical Spectral Devices
4760 Walnut Street, Suite 106
Boulder, CO 80301
USA
Voice: 303–444–6522
Fax: 303–444–6825

Curtis Davis
Naval Research Laboratory
4555 Overlook Avenue, SW
Code 7212
Washington, DC 20375
USA
Voice: 202–767–9269
Fax: 202–404–7453
Net: davis@riva.nrl.navy.mil

Edward Early *Instrument Calibrations*
NIST/Optical Technology Division
MS 8442
Gaithersburg, MD 20771
USA
Voice: 301–975–2343
Fax: 301–840–8551
Net: edward.early@nist.gov

Jim Ehramjian *Group E*
Biospherical Instruments, Inc.
5340 Riley Street
San Diego, CA 92110
USA
Voice: 619–686–1888
Fax: 619–686–1887
Net: support@biosph.rical.com

Robert Eplee, Jr. *In-Water Data Reduction*
NASA/GSFC/SAIC General Sciences Corporation
Code 970.2
Greenbelt, MD 20771
USA
Voice: 301–286–0953
Fax: 301–286–0268
Net: eplee@calval.gsfc.nasa.gov

Robert Faus *Group D*
Analytical Spectral Devices
4760 Walnut Street, Suite 105
Boulder, CO 80301
USA
Voice: 303–444–6522
Fax: 303–444–6825
Net: rjfaus@asdi.com

Sonia Gallegos *Withdrew?*
Naval Research Laboratory/Stennis Space Center
Code 7240
Stennis Space Center, MS 39529
USA
Voice: 601–688–4867
Fax: 601–688–4149
Net: gallegos@nrlssc.navy.mil

Charles Gibson *Lecturer and FASCAL*
NIST/Optical Technology Division
MS 8441
Gaithersburg, MD 20899
USA
Voice: 301–975–2329
Fax: 301–869–5700
Net: charles.gibson@nist.gov

Hans Hakvoort *Group A*
GKSS
Max-Planck-Strasse, GFE
Geesthacht 21502
GERMANY
Voice: 49–4152–872472
Fax: 49–4152–8722466
Net: hakvoort@gkss.de

Chung-ru Ho *Group B*
National Taiwan Ocean University
Department of Oceanography
Keelung, Taiwan
REPUBLIC OF CHINA
Voice: 886–2–4620912
Net: chungru@sun\$oce.ntou.edu.tw

Herschel Hochman *Group E*
University of South Florida
140 Seventh Avenue, South
KRC 3119, MSL 119
St. Petersburg, FL 33701
USA
Voice: 813–893–9186
Fax: 813–893–9103
Net: val@carbon.marine.usf.edu

Stanford Hooker *In-Water Data Collection*
NASA/GSFC
Code 970.2
Greenbelt, MD 20771
USA
Voice: 301–286–9503
Fax: 301–286–0268
Net: stan@ardbeg.gsfc.nasa.gov

James Irish *Group A*
Woods Hole Oceanographic Institute
307 Smith, MS 17
Woods Hole, MA 02543
USA
Voice: 508–289–2732
Fax: 508–457–2195
Net: jirish@whoi.edu

Carol Johnson *Instrument Calibrations*
NIST/Optical Technology Division
MS 8441
Gaithersburg, MD 20899
USA
Voice: 301–975–2322
Fax: 301–869–5700
Net: cjohnson@nist.gov

Nan-jung Kuo *Group D*
National Taiwan Ocean University
Department of Oceanography
Keelung, Taiwan
REPUBLIC OF CHINA
Voice: 886–2–4620912
Net: kuonj@sun\$oce.ntou.edu.tw

Thomas Larason *Lecturer and*
NIST/Optical Technology Division *Instrument*
MS 8441 *Calibrations*
Gaithersburg, MD 20899
USA
Voice: 301–975–2334
Fax: 301–869–5700
Net: thomas.larason@nist.gov

Li-Shing Lee *Group E*
NSPO
8 Prosperity Road
Hain-chu Science Park
Hain-chu, Taiwan
REPUBLIC OF CHINA
Voice: 886–3–5784208
Fax: 886–2–5770134
Net:www.lle@nspo.gov.tw

Hsien-wen Li *Group G*
National Taiwan Ocean University
Department of Oceanography
Keelung, Taiwan
REPUBLIC OF CHINA
Voice: 886–2–4620912

Charlotte Lovengreen *Group E*
Biospherical Instruments, Inc.
5340 Riley Street
San Diego, CA 92110
USA
Voice: 619–686–1888
Fax: 619–686–1887

Stephane Maritorena *Group H*
NASA/GSFC/USRA
Code 970.2
Greenbelt, MD 20771
USA
Fax: 301–286–0268
Net: stephane@calval.gsfc.nasa.gov

Charles McClain *Discussion Leader*
NASA/GSFC
Code 971
Greenbelt, MD 20771
USA
Voice: 301–286–5377
Fax: 301–286–0268
Net: mcclain@calval.gsfc.nasa.gov

James McLean *Group H*
NASA/GSFC
Code 925
Greenbelt, MD 20771
USA
Voice: 301–286–5082

Scott McLean *Lecturer*
Satlantic, Inc.
3295 Barrington Street
Halifax, Nova Scotia B3K 5X8
CANADA
Voice: 902–492–4781
Net: scott@satlantic.com

Dave Menzies *Lecturer and Group B*
UCSB/ICESS
Santa Barbara, CA 93106
USA
Voice: 805–893–2578
Net: davem@icess.ucsb.edu

Eduardo Michelena *Group G*
National Data Buoy Center
Building 1100
Stennis Space Center, MS 39529
USA
Voice: 601–688–1715
Fax: 601–688–3153

Gerald Moore *In-Water Data Processing and Lecturer*
Plymouth Marine Laboratory
Prospect Place, West Hoe
Plymouth PL1 3DH
UNITED KINGDOM
Voice: 44–1–752–222772
Fax: 44–1–752–670637
Net: g.moore@pmc.ac.uk

John Morrow *Lecturer*
Biospherical Instruments, Inc.
5340 Riley Street
San Diego, CA 92110
USA
Voice: 619–686–1888
Fax: 619–686–1887
Net: support@biospherical.com

Jim Mueller *In-Water Data Collection*
SDSU/CHORS
6505 Alvardo Road, Suite 206
San Diego, CA 92120
USA
Voice: 619–594–2230
Fax: 619–594–8670
Net: jim@chors.sdsu.edu

Regina Preusker *Group C*
DLR-WS
Rudower Chaussee 5
Berlin, 12489
GERMANY
Voice: 49–30–67055–582
Fax: 49–30–67055–572
Net: regina.preuster@dlr.de

William Rhea *Group B*
Naval Research Laboratory
4555 Overlook Avenue, SW
Code 7212
Washington, DC 20375
USA
Voice: 202–767–0439
Fax: 202–404–7453
Net: rhea@rira.nrl.navy.mil

Rodney Riley *Group A*
Computer Sciences Corporation
Building 3205
Stennis Space Center, MS 39529
USA
Voice: 601–688–2267
Fax: 601–688–3489
Net: rriley@csc.ndbc.noaa.gov

Bob Saunders *Laboratory Instructor*
NIST/Optical Technology Division
MS 8441
Gaithersburg, MD 20899
USA
Voice: 301–975–2355
Fax: 301–869–5700
Net: rds@nist.gov

Brian Schieber *In-Water Data Processing*
NASA/GSFC/SAIC General Sciences Corporation
Code 970.2
Greenbelt, MD 20771
USA
Voice: 301–286–1440
Fax: 301–286–0268
Net: schieb@shark.gsfc.nasa.gov

Ping-Shine Shaw *Field Calibrations*
NIST/Optical Technology Division
MS 8442
Gaithersburg, MD 20899
USA
Voice: 301–975–4416
Fax: 301–869–5700
Net: psshaw@nist.gov

Ajit Subramaniam *Group F*
NOAA/Coastal Services Center
2224 South Hobson Avenue
Charleston, SC 29405
USA
Voice: 803–974–6250
Fax: 803–974–6224
Net: asubramaniam@cceh.noaa.gov

Karl-Heinz Suemnich *Group C*
DLR-WS
Rudower Chaussee 5
Berlin, 12489
GERMANY
Voice: 4930–67055–570
Fax: 4930–67055–572
Net: karl--heinz.suemnich@dlr.de

Gregory Terrie *Group F*
Naval Research Laboratory
Code 7243
Building 1105, Room E526
Stennis Space Center, MS 39529
USA
Voice: 601–688–4549
Net: terie@nrlssc.navy.mil

Ambler Thompson *In-Air Data Collection and Instrument Calibrations*
NIST/Optical Technology Division
MS 8442
Gaithersburg, MD 20899
USA
Voice: 301–975–2333
Fax: 301–840–8551
Net: ambler.thompson@nist.gov

Wei-peng Tsai *Group F*
National Taiwan Ocean University
Department of Oceanography
Keelung, Taiwan
REPUBLIC OF CHINA
Voice: 886–2–4620912
Net: tsai@tours.oce.ntou.edu.tw

Kirk Waters *Group H*
NOAA/Coastal Service Center
2224 South Hudson Avenue
Charleston, SC 29405
USA
Voice: 803–974–6227
Fax: 803–974–6224
Net: kwaters@osc.noaa.gov

Giuseppe Zibordi *Group A*
Joint Research Centre
TP272
Ispra, 21020
ITALY
Voice: 39–0–332–789–034
Net: giuseppe.zibordi@jrc.it

Editorial Note

This document is presented *as submitted* with minor modifications to correct typographical or obvious clerical errors and to maintain the established style of the *SeaWiFS Postlaunch Technical Report Series*.

Glossary

A/D	Analog-to-Digital
AMT	Atlantic Meridional Transect
AOP	Apparent Optical Property
ASD	Analytical Spectral Devices
BRDF	Bidirectional Reflectance Distribution Function
BSI	Biospherical Instruments, Inc.
C/CSC	NOAA Coastal Services Center, Charleston, South Carolina
CHORS	Center for Hydro-Optics and Remote Sensing
CZCS	Coastal Zone Color Scanner
dc	Direct Current
DMM	Digital Multimeter
FARCAL	Facility for Advanced Radiometric Calibrations
FASCAL	Facility for Automated Spectroradiometric Calibrations
FEL	Not an acronym, but a lamp designator.
FORTRAN	Formula Translation (computer language)

GLOBEC Global Ocean System Eco-Dynamics
GPIB General Purpose Interface Bus
GSFC Goddard Space Flight Center

HP Hewlett-Packard

IMSL International Mathematical and Statistical Libraries

JRC Joint Research Centre

MLML Moss Landing Marine Laboratory
MOBY Marine Optical Buoy
MOS Modular Optoelectronic Scanner
MVDS Multichannel Visible Detection System

NASA National Aeronautics and Space Administration
NIST National Institute of Standards and Technology
NOAA National Oceanic and Atmospheric Administration
NRL Naval Research Laboratory, Code 7212, Washington, DC.

OCI Ocean Color Irradiance (radiometer)
OCP Ocean Color Profiler
OCR Ocean Color Radiometer
OL Optronic Laboratories, Inc.
OSC Orbital Sciences Corporation

PAR Photosynthetically Available Radiation
PC Personal Computer
PML Plymouth Marine Laboratory

RSS Root-Sum Square

SAS-II Satlantic Airborne Sensor
SBRC Santa Barbara Research Center (Raytheon)
SBRS Santa Barbara Remote Sensing (Hughes)
S/CSC National Data Buoy Center, Stennis Space Center, Mississippi
SDSU San Diego State University
SDY Sequential Day of the Year
SeaWiFS Sea-viewing Wide Field-of-view Sensor
SIMBIOS Sensor Intercomparison and Merger for Biological and Interdisciplinary Oceanic Studies
SIRREX SeaWiFS Intercalibration Round-Robin Experiment
S/N Serial Number
S/NRL Naval Research Laboratory, Code 7243, Stennis Space Center, Mississippi.
SQM SeaWiFS Quality Monitor
SXR SeaWiFS Transfer Radiometer

UA University of Arizona
UCSB University of California at Santa Barbara
UM University of Miami
USN Naval Research Laboratory, Code 7240, Stennis Space Center, Mississippi
UV Ultraviolet

WSSC Washington Suburban Sanitary Commission

Symbols

a_i Coefficient in modified planckian function.
$\overline{B}$ Time-averaged background signal.
$\overline{B}_{\mathrm{C}}$ Time-averaged background signal obtained using the lens cap.
$\overline{B}_{\mathrm{S}}$ Time-average background signal using an on-axis shutter.
$\overline{D}$ Average calibration coefficient.
D_S Satlantic calibration coefficient.
$D_{\mathrm{SXR}}(\lambda)$ SXR calibration coefficient.

$E(\lambda)$ Spectral irradiance.
$E(\lambda, 50)$ Spectral irradiance at 50 cm from an FEL lamp.
$E_d(z, \lambda)$ Downwelled, in-water, spectral irradiance as a function of depth.
$E_s(0^+, \lambda)$ Downwelled, in-air, spectral irradiance at the surface of the water.
$E_s(t)$ Downwelled, in-air, spectral irradiance as a function of time.

F Inverse of the average calibration coefficient, i.e., the average calibration factor.
F_{BSI} Calibration factor from BSI.
F_{FS} Average calibration factor determined using the UV irradiance field source.
F_{JRC} Calibration factor from JRC.
F_{NL} Average calibration factor determined by NIST.
F_{PML} Calibration factor from PML.
F_S Calibration factor from Satlantic.

$H(\lambda)$ Measured radiance divided by the calculated radiance for the field sensors.
$H'(\lambda)$ Measured radiance divided by the calculated radiance for the SXR.

i Index to denote coefficient in modified planckian function (i from 0–6).

j Index to denote a measurement at time t.

k Index to denote one measurement session.
$k_{10}(\lambda)$ SXR gain correction factor.
$k(\lambda)$ Extinction coefficient.

$L_{\mathrm{C}}(\lambda)$ Calculated radiance of the illuminated plaque.
$L_{\mathrm{p}}(t)$ Radiance of a diffusely reflecting standard plaque as a function of time.
$L_{\mathrm{p}}(\lambda)$ Radiance of a diffusely reflecting standard plaque.
$\overline{L}_{\mathrm{S}}(\lambda)$ Radiance determined using Satlantic calibration coefficients.
$L_{\mathrm{sfc}}(t)$ Radiance of the water's surface as a function of time.
$L_{\mathrm{sfc}}(\lambda)$ Radiance of the water's surface.
$L_{\mathrm{sky}}(t)$ Radiance of the sky as a function of time.
$L_{\mathrm{sky}}(\lambda)$ Radiance of the sky.
$\overline{L}_{\mathrm{SXR}}$ Radiance measured with the SXR.
$L_u(z, \lambda)$ Upwelled, in-water, spectral radiance as a function of depth.
$L_u(0^-, \lambda)$ Upwelled, in-water, spectral radiance just below the surface.
$L_W(\lambda)$ Water-leaving radiance.

m Number of measurement sessions.

n Total number of individual samples acquired during time t.
$n(\lambda)$ Index of refraction.

r Distance from the irradiance lamp to the plaque.
R Linear correlation coefficient.
$R(\theta/\theta', \lambda)$ Bidirectional reflectance factor.
$R(\theta/\mathrm{h}, \lambda)$ Directional hemispherical reflectance.
$R(\mathrm{h}/\theta', \lambda)$ Hemispherical directional reflectance.
$R_{\mathrm{RS}}(\lambda)$ Remote sensing reflectance.
$R_{\mathrm{RS,c}}$ Remote sensing reflectance determined using calibrated radiance and irradiance sensors.

$R_{\mathrm{RS,p}}$ Remote sensing reflectance determined using the reflected radiance from a diffuse plaque to determine the downwelling irradiance.
$\overline{S}_{\mathrm{N}}$ Time-averaged net signal.
$\overline{S}_{\mathrm{N}}^{\mathrm{C}}$ Time-averaged net signal using $\overline{B}_{\mathrm{C}}$.
$\overline{S}_{\mathrm{N}}^{\mathrm{S}}$ Time-averaged net signal using $\overline{B}_{\mathrm{S}}$.
$\breve{S}_{\mathrm{N}}^{\mathrm{C}}$ Variability of the net capped signal.
$\breve{S}_{\mathrm{N}}^{\mathrm{S}}$ Variability of the net shuttered signal.

$S_{\mathrm{P}}(\lambda)$ Signal from plaque, proportional to radiance.
$S_{\mathrm{sfc}}(\lambda)$ Signal from the surface of the water, proportional to radiance.
$S_{\mathrm{sky}}(\lambda)$ Signal from the sky, proportional to the radiance.
$\overline{S}_{\mathrm{T}}$ Time-averaged total signal.

t Time at the particular data sampling.
t' Time at the particular data sampling, where the prime denotes different values.
t'' Time at the particular data sampling, where the double prime denotes different values.
$\overline{X}(\lambda)$ Time-averaged output at wavelength λ for n measurements.
$\overline{X}_k(\lambda)$ Time-averaged output of the n measurements for the kth measurement session.
$\breve{X}_k(\lambda)$ Variation in the results for measurement session k referenced to the average.
$\hat{X}(\lambda)$ Average result for m measurement sessions.
$X_j(\lambda, t)$ Output of the sensor at wavelength λ for measurement j taken at time t.

z Depth variable.

$\overline{\Delta}'$ Average relative difference.
$\Delta\lambda$ Wavelength difference.

θ Polar angle for incident direction.
θ' Polar angle for exitent direction.

λ Detection wavelength.

$\rho_W(\lambda)$ Fresnel reflectance of water.
$\rho_p(\lambda)$ Reflectance of standard gray plaque.

σ Standard deviation.
σ' Relative standard deviation.

ϕ Azimuthal angle for incident direction.
ϕ' Azimuthal angle for exitent direction.

References

Biggar, S.F., 1999: A method for correcting the irradiance of standards of spectral irradiance (lamps) operated at non-standard distances. *Opt. Photonics News,* (accepted).

Carder, K.L., and R.G. Steward, 1985: A remote-sensing reflectance model of a red-tide dinoflagellate off west Florida. *Limnol. Oceanogr.,* **30,** 286–298.

DeWitt, D.P., and J.C. Richmond, 1988: "Thermal radiative properties of materials." In: *Theory and Practice of Radiation Thermometry,* D.P. DeWitt and G.D. Nutter, Eds., John Wiley and Sons, Inc., New York, 91–187.

Early, E.A., E.A. Thompson, and P. Disterhoft, 1998a: A field calibration unit for ultraviolet spectroradiometers. *Appl. Opt.,* **37,** 6,664–6,670.

——, A. Thompson, B.C. Johnson, J. DeLuisi, P. Disterhoft, D. Wardle, E. Wu, W. Mou, J. Ehramjian, J. Tusson, T. Mestechkina, M. Beaubian, J. Gibson, and D. Hayes, 1998b: The 1996 North American interagency intercomparison of ultraviolet monitoring spectroradiometers. *J. Res. NIST,* **103,** 449–482.

——, ——, ——, ——, ——, ——, ——, ——, Y. Sun, T. Lucas, T. Mestechkina, L. Harrison, J. Berndt, and D. Hayes, 1998c: The 1995 North American interagency intercomparison of ultraviolet monitoring spectroradiometers. *J. Res. NIST,* **103,** 15–62.

——, P.Y. Barnes, B.C. Johnson, J.J. Butler, C.J. Bruegge, S.F. Biggar, P.R. Spyak, and M.M. Pavlov, 1999: Bidirectional reflectance round-robin in support of the Earth Observing System Program. *J. Atmos. Oceanic Tech.,* (accepted).

Heath, D.F., Z. Wei, W.K. Fowler, and V.W. Nelson, 1993: Comparison of spectral radiance calibrations of SBUV-2 satellite ozone monitoring instruments using integrating sphere and flat-plate diffuser techniques. *Metrologia,* **30,** 259–264.

Hooker, S.B., C.R. McClain, and A. Holmes, 1993: Ocean color imaging: CZCS to SeaWiFS. *Mar. Technol. Soc. J.,* **27,** 3–15.

——, ——, J.K. Firestone, T.L. Westphal, E. Yeh, and Y. Ge, 1994a: The SeaWiFS Bio-Optical Archive and Storage System (SeaBASS), Part 1. *NASA Tech. Memo. 104566, Vol. 20,* S.B. Hooker and E.R. Firestone, Eds., NASA Goddard Space Flight Center, Greenbelt, Maryland, 40 pp.

——, T.L. Westphal, Y. Ge, 1994b: "The SIRREX database." In: Hooker, S.B., C.R. McClain, J.K. Firestone, T.L. Westphal, E. Yeh, and Y. Ge, 1994: The SeaWiFS Bio-Optical Archive and Storage System (SeaBASS), Part 1. *NASA Tech. Memo. 104566, Vol. 20,* S.B. Hooker and E.R. Firestone, Eds., NASA Goddard Space Flight Center, Greenbelt, Maryland, 23–30.

——, and J. Aiken, 1998: Calibration evaluation and radiometric testing of field radiometers with the SeaWiFS Quality Monitor (SQM). *J. Atmos. Oceanic Tech.,* **15,** 995–1,007.

——, and C.R. McClain, 1999: A comprehensive plan for the calibration and validation of SeaWiFS data. *Prog. Oceanogr.,* (accepted).

——, G. Zibordi, G. Lazin, and S. McLean, 1999: The SeaBOARR-98 Field Campaign. *NASA Tech. Memo. 1999–206892, Vol. 3,* S.B. Hooker and E.R. Firestone, Eds., NASA Goddard Space Flight Center, Greenbelt, Maryland, 40 pp.

Johnson, B.C., S.S. Bruce, E.A. Early, J.M. Houston, T.R. O'Brian, A. Thompson, S.B. Hooker, and J.L. Mueller, 1996: The Fourth SeaWiFS Intercalibration Round-Robin Experiment, SIRREX-4, May 1995. *NASA Tech. Memo. 104566, Vol. 37,* S.B. Hooker and E.R. Firestone, Eds., NASA Goddard Space Flight Center, Greenbelt, Maryland, 66 pp.

——, J.B. Fowler, and C.L. Cromer, 1998a: The SeaWiFS Transfer Radiometer (SXR). *NASA Tech. Memo. 1998–206892, Vol. 1,* S.B. Hooker and E.R. Firestone, Eds., NASA Goddard Space Flight Center, Greenbelt, Maryland, 58 pp.

——, P-S. Shaw, S.B. Hooker, and D. Lynch, 1998b: Radiometric and engineering performance of the SeaWiFS Quality Monitor (SQM): A portable light source for field radiometers. *J. Atmos. Oceanic Tech.,* **15,** 1,008–1,022.

——, R.E. Eplee, Jr., R.A. Barnes, E.A. Early, and R.T. Caffrey, 1999: The 1997 Prelaunch Radiometric Calibration of SeaWiFS. *NASA Tech. Memo. 1999–206892, Vol. 4,* S.B. Hooker and E.R. Firestone, Eds., NASA Goddard Space Flight Center, Greenbelt, Maryland, 51 pp.

McClain, C.R., W.E. Esaias, W. Barnes, B. Guenther, D. Endres, S.B. Hooker, G. Mitchell, and R. Barnes, 1992: Calibration and Validation Plan for SeaWiFS. *NASA Tech. Memo. 104566, Vol. 3,* S.B. Hooker and E.R. Firestone, Eds., NASA Goddard Space Flight Center, Greenbelt, Maryland, 60 pp.

——, M.L. Cleave, G.C. Feldman, W.W. Gregg, S.B. Hooker, and N. Kuring, 1998: Science quality SeaWiFS data for global biosphere research. *Sea Technol.,* September 1998, 10–16.

Mueller, J.L., 1993: The First SeaWiFS Intercalibration Round-Robin Experiment, SIRREX-1, July 1992. *NASA Tech. Memo. 104566, Vol. 14,* S.B. Hooker and E.R. Firestone, Eds., NASA Goddard Space Flight Center, Greenbelt, Maryland, 60 pp.

——, and R.W. Austin, 1992: Ocean Optics Protocols for SeaWiFS Validation. *NASA Tech. Memo. 104566, Vol. 5,* S.B. Hooker and E.R. Firestone, Eds., NASA Goddard Space Flight Center, Greenbelt, Maryland, 43 pp.

——, B.C. Johnson, C.L. Cromer, J.W. Cooper, J.T. McLean, S.B. Hooker, and T.L. Westphal, 1994: The Second SeaWiFS Intercalibration Round-Robin Experiment, SIRREX-2, June 1993. *NASA Tech. Memo. 104566, Vol. 16,* S.B. Hooker and E.R. Firestone, Eds., NASA Goddard Space Flight Center, Greenbelt, Maryland, 121 pp.

——, and R.W. Austin, 1995: Ocean Optics Protocols for SeaWiFS Validation, Revision 1. *NASA Tech. Memo. 104566, Vol. 25,* S.B. Hooker, E.R. Firestone, and J.G. Acker, Eds., NASA Goddard Space Flight Center, Greenbelt, Maryland, 67 pp.

——, B.C. Johnson, C.L. Cromer, S.B. Hooker, J.T. McLean, and S. Biggar, 1996: The Third SeaWiFS Intercalibration Round-Robin Experiment, SIRREX-3, September 1994. *NASA Tech. Memo. 104566, Vol. 34,* S.B. Hooker, E.R. Firestone, and J.G. Acker, Eds., NASA Goddard Space Flight Center, Greenbelt, Maryland, 78 pp.

Saunders, R.D., and J.B. Shumaker, 1977: Optical Radiation Measurements: The 1973 NBS Scale of Spectral Irradiance. *NBS Tech. Note 594-13,* National Bureau of Standards, Gaithersburg, Maryland, 29 pp.

Shaw, P-S., B.C. Johnson, S.B. Hooker, and D. Lynch, 1997: The SeaWiFS Quality Monitor—a portable field calibration light source. *Proc. SPIE,* **2963,** 772–776.

Taylor, B.N., and C.E. Kuyatt, 1994: Guidelines for Evaluating and Expressing the Uncertainty of NIST Measurement Results. *NIST Tech. Note 1297,* U.S. Department of Commerce, National Institute of Standards and Technology, Washington, DC, 20 pp.

Walker, J.H., R.D. Saunders, J.K. Jackson, and D.A. McSparron, 1987: Spectral Irradiance Calibrations. *NBS Special Publication 250-20,* U.S. Department of Commerce, National Institute of Standards and Technology, Washington, DC, 37 pp., plus Appendices.

——, and A. Thompson, 1994: Improved automated current control for standard lamps. *J. of Res. NIST,* **99,** 255–261.

The SeaWiFS Postlaunch Technical Report Series

Vol. 1

Johnson, B.C., J.B. Fowler, and C.L. Cromer, 1998: The SeaWiFS Transfer Radiometer (SXR). *NASA Tech. Memo. 1998–206892, Vol. 1,* S.B. Hooker and E.R. Firestone, Eds., NASA Goddard Space Flight Center, Greenbelt, Maryland, 58 pp.

Vol. 2

Aiken, J., D.G. Cummings, S.W. Gibb, N.W. Rees, R. Wooddd-Walker, E.M.S. Woodward, J. Woolfenden, S.B. Hooker, J-F. Berthon, C.D. Dempsey, D.J. Suggett, P. Wood, C. Donlon, N. González-Benítez, I. Huskin, M. Quevedo, R. Barciela-Fernandez, C. de Vargas, and C. McKee, 1998: AMT-5 Cruise Report. *NASA Tech. Memo. 1998–206892, Vol. 2,* S.B. Hooker and E.R. Firestone, Eds., NASA Goddard Space Flight Center, Greenbelt, Maryland, 113 pp.

Vol. 3

Hooker, S.B., G. Zibordi, G. Lazin, and S. McLean, 1999: The SeaBOARR-98 Field Campaign. *NASA Tech. Memo. 1999–206892, Vol. 3,* S.B. Hooker and E.R. Firestone, Eds., NASA Goddard Space Flight Center, Greenbelt, Maryland, 40 pp.

Vol. 4

Johnson, B.C., R.E. Eplee, Jr., R.A. Barnes, E.A. Early, and R.T. Caffrey, 1999: The 1997 Prelaunch Radiometric Calibration of SeaWiFS. *NASA Tech. Memo. 1999–206892, Vol. 4,* S.B. Hooker and E.R. Firestone, Eds., NASA Goddard Space Flight Center, Greenbelt, Maryland, 51 pp.

Vol. 5

Barnes, R.A., R.E. Eplee, Jr., S.F. Biggar, K.J. Thome, E.F. Zalewski, P.N. Slater, and A.W. Holmes 1999: The SeaWiFS Solar Radiation-Based Calibration and the Transfer-to-Orbit Experiment. *NASA Tech. Memo. 1999–206892, Vol. 5,* S.B. Hooker and E.R. Firestone, Eds., NASA Goddard Space Flight Center, 28 pp.

Vol. 6

Firestone, E.R., and S.B. Hooker, 1999: SeaWiFS Postlaunch Technical Report Series Cumulative Index: Volumes 1–5. *NASA Tech. Memo. 1999–206892, Vol. 6,* S.B. Hooker and E.R. Firestone, Eds., NASA Goddard Space Flight Center, Greenbelt, Maryland, (in preparation).

Vol. 7

Johnson, B.C., H.W. Yoon, S.S. Bruce, P-S. Shaw, A. Thompson, S.B. Hooker, R.E. Eplee, Jr., R.A. Barnes, S. Maritorena, and J.L. Mueller, 1999: The Fifth SeaWiFS Intercalibration Round-Robin Experiment (SIRREX-5), July 1996. *NASA Tech. Memo. 1999–206892, Vol. 7,* S.B. Hooker and E.R. Firestone, Eds., NASA Goddard Space Flight Center, 75 pp.